EFFECTS OF ION IRRADIATION ON THE CHEMICAL AND MICROSTRUCTURAL PROPERTIES OF SOL-GEL DERIVED THIN FILMS

By
SEYYED ALI SHOJAEE

Bachelor of Science
Ferdowsi University of Mashhad
Mashhad, Iran
2005

Master of Science
Sharif University of Technology
Tehran, Iran
2008

Submitted to the Faculty of the
Graduate College of the
Oklahoma State University
in partial fulfillment of
the requirement for
the Degree of
DOCTOR OF PHILOSOPHY
August 2016

EFFECTS OF ION IRRADIATION ON THE CHEMICAL AND MICROSTRUCTURAL PROPERTIES OF SOL-GEL DERIVED THIN FILMS

Thesis Approved:

Don A. Lucca

Dissertation Advisor

Daniel R. Grischkowsky

Sandip P. Harimkar

Matthew J. Klopfstein

ACKNOWLEDGMENTS

I would like to thank my advisor, Professor Don A. Lucca, for his support throughout this project and many others. I would also like to thank my committee, Professor Daniel Grischkowsky, Professor Matthew Klopfstein, and Professor Sandip Harimkar for their valuable time and suggestions. I would also like to acknowledge the helps and comments I received from Professor Hamed Hatami, Professor Prabhakar Pagilla and the late Professor Ranga Komanduri who at one point all served on my committee.

I extend my gratitude to Dr. Andreas Mehner and Mr. Torsten Prenzel of the Stiftung Institut für Werkstofftechnik (IWT) for their help in the synthesis of the sol-gel films and in performing the XPS experiments. I would also like to thank Dr. Yongqiang Wang at Los Alamos National Laboratory for his devoted help and for performing ion irradiation and ERD/RBS experiments. I am also grateful to my colleague Dr. Yongli Qi for performing nanoindentation experiments. I would also like to thank my colleagues, Tres Harriman and Arezoo Zare for their help and support.

The financial support for this project was provided by the National Science Foundation through Grant Nos. OISE-0352377 and OISE-0128050 and is gratefully acknowledged. The funding for the Transregionaler Sonderforschungsbereich SFB/TR4 was provided by the Deutsche Forschungsgemeinschaft and is also gratefully acknowledged.

Finally, I would like to thank my family and friends for their continuous support and encouragement.

Acknowledgements reflect the views of the author and are not endorsed by committee members or Oklahoma State University.

Name: SEYYED ALI SHOJAEE

Date of Degree: AUGUST 2016

Title of Study: EFFECTS OF ION IRRADIATION ON THE CHEMICAL AND MICROSTRUCTURAL PROPERTIES OF SOL-GEL DERIVED THIN FILMS

Major Field: MECHANICAL AND AEROSPACE ENGINEERING

Abstract:

The effects of ion irradiation on the chemical and structural properties of ion irradiated thin films were studied. Ion irradiation was performed using 200 keV H^+, 400 keV N^{2+}, 1 MeV Cu^+, 4 MeV Cu^{2+}, and 9 MeV Cu^{3+} ions. The irradiation targets were sol-gel derived silica-based thin films based on TEOS/MTES ingredients coated on a (100) silicon substrate. The structure of the films was studied by a combination of Raman spectroscopy, photoluminescence spectroscopy, Fourier transform infrared (FT-IR) spectroscopy, X-ray diffraction (XRD), elastic recoil detection (ERD), Rutherford backscattering spectrometry (RBS), atomic force microscopy, scanning electron microscopy, and X-ray photoelectron spectroscopy (XPS). The results indicate that irradiation with 200 keV H^+ and 400 keV N^{2+} ions only causes hydrogen loss, whereas irradiation with 1 MeV Cu^+, 4 MeV Cu^{2+}, and 9 MeV Cu^{3+} ions leads to hydrogen, oxygen, and carbon loss. A systematic investigation of the structure of amorphous silica and free carbon clusters formed during ion irradiation was performed. The results indicate that there is a decrease in the Si-O-Si bond angle of the silica phase with increasing ion energy. In addition, evidence of a transformation from tetrahedrally coordinated silica to octahedrally coordinated silica is observed after ion irradiation with 9 MeV Cu^{3+} ions. It was also found that, compared to heat-treated films, the free carbon clusters formed during ion irradiation have more defective graphitic six-fold structure. After ion irradiation with 4 MeV Cu^{2+} and 9 MeV Cu^{3+} ions, the Raman spectroscopy results indicates a complete destruction of the graphitic six-fold structure. It is also confirmed that with increasing irradiation fluence and ion energy, there is an increase in carbon incorporation within the silica structure. The microstructure of the films is determined as an amorphous silica matrix with isolated clusters of amorphous carbon. The structural changes after ion irradiation, specifically, changes in the Si-O-Si bond angle and concentration of carbon-rich tetrahedra were then used to explain the enhancement in the elastic modulus and hardness of the ion irradiated films. The results indicate that the changes in the Si-O-Si bond angle was the dominant mechanism for the enhancement of the elastic modulus of the films after ion irradiation.

TABLE OF CONTENTS

1 INTRODUCTION **1**

1.1 Motivation for the present study . . . 1

1.2 Objectives . . . 2

2 BACKGROUND **4**

2.1 Silica-based sol-gel thin films . . . 4

2.2 Polymer-derived SiOC ceramic materials . . . 5

2.3 Ion irradiation of polymers . . . 6

2.4 Microstructure of SiOC ceramics . . . 7

2.4.1 Carbon . . . 9

2.4.2 Amorphous silica . . . 12

2.4.3 Silicon carbide . . . 16

2.4.4 Silicon . . . 17

2.4.5 Microstructural configuration of polymer-derived ceramics . . . 17

2.5 Possible effects of irradiation on polymer-derived ceramics . . . 19

2.5.1 Crystallization . . . 19

2.5.2 Synthesis of silicon carbide nanoparticles . . . 20

2.6 Possible substrate-film reactions during heat-treatment . . . 21

2.7 Summary of previous studies on ion irradiation of sol-gel derived thin films . . . 21

3 EXPERIMENTAL APPROACH **24**

3.1 Thin film synthesis, deposition, and heat-treatment . . . 24

3.2 Ion irradiation . . . 26

3.3 Characterization techniques . . . 28

3.3.1 Raman spectroscopy . . . 28

3.3.2 Fourier-transform infrared spectroscopy (FT-IR) . . . 30

3.3.3 Rutherford backscattering spectrometry and elastic recoil detection . . . 30

3.3.4 X-ray diffraction 31
3.3.5 Scanning electron microscopy 31
3.3.6 X-ray photoelectron spectroscopy 31

4 RESULTS AND DISCUSSION **33**
4.1 Surface condition of the ion irradiated and heat-treated films 33
4.2 Conversion of films with light ions 33
4.2.1 Chemical evolution of the films after heat-treatment and ion irradiation with light ions 33
4.2.2 FT-IR spectroscopy characterization 36
4.2.3 Raman spectroscopy characterization of free carbon clusters 44
4.2.4 XPS characterization of the films irradiated with N^{2+} ions 50
4.2.5 Microstructural configuration of the films irradiated with light ions 53
4.2.6 Mechanical properties of the films after ion irradiation with light ions 57
4.3 Conversion of films with heavy ions 62
4.3.1 Chemical evolution of the films after ion irradiation with heavy ions 62
4.3.2 FT-IR spectroscopy characterization 66
4.3.3 Raman spectroscopy characterization of free carbon clusters 72
4.3.4 XPS characterization of the films irradiated with heavy ions 77
4.3.5 Microstructural configuration of the films after ion irradiation with heavy ions 82
4.3.6 Mechanical properties of the films after ion irradiation with heavy ions 87
4.4 Secondary heat-treatment of ion irradiated films 90
4.4.1 FT-IR spectroscopy characterization of ion irradiated base-catalyzed films after secondary heat-treatment 91
4.4.2 Raman spectroscopy characterization of ion irradiated base-catalyzed films after secondary heat-treatment 94

5 CONCLUSIONS AND POSSIBLE FUTURE WORK **97**
5.1 Conclusions 97
5.2 Possible Future Work 101

Bibliography **102**

A Curve fitting results of C 1s spectra of ion irradiated films **122**

B XPS O 1s spectra of ion irradiated and heat-treated films **125**

C Silica Raman modes of fused silica and the film heat-treated at 800 °C **127**

D Estimation of free carbon content of ion irradiated and heat-treated films **129**

E Low Temperature Photoluminescence Spectra **132**

LIST OF TABLES

3.1 The chemical composition of acid- and base-catalyzed sols. 24

3.2 Ion irradiation conditions of films for the acid-catalyzed films. 27

3.3 Ion irradiation and secondary heat-treatment conditions for the base-catalyzed films. 27

4.1 Curve fitting results of the FT-IR spectra of the heat-treated and H^+ and N^{2+} ion irradiated films. 44

4.2 Curve fitting results of the Raman spectra of the heat-treated and H^+ and N^{2+} irradiated films exhibiting carbon related D and G Raman modes. 47

4.3 Bond dissociation energy of various chemical bonds in TEOS and similar compounds. The symbol Me stands for methyl (CH_3). 63

4.4 Curve fitting results of the FT-IR spectra of the films irradiated with 1 MeV Cu^+ ions. 68

4.5 Curve fitting results of the Raman spectra of 1 MeV Cu^+ irradiated films exhibiting carbon related D and G Raman modes. 75

4.6 XPS and ERD/RBS measured chemical composition of the films 80

4.7 Curve fitting results of FT-IR spectra of base-catalyzed films irradiated with H^+ and N^{2+} ions after secondary heat-treatment at 1100 °C and 1350 °C. 92

4.8 Curve fitting results of the Raman spectra of base-catalyzed films after secondary heat-treatment. 95

5.1 The proposed microstructure of ion irradiated films 100

D.1 The concentration of different SiO_xC_y tetrahedra along with C/Si ratio and percentage of free carbon in each specimen. 131

LIST OF FIGURES

1.1 a) Diamond turning of a sol-gel coated steel mold b) steel mold with a micro-machined sol-gel derived coating c) SEM image of the micro-machined coated surface [2]. . . . 2

2.1 The molecular structure of a) TEOS and b) MTES. 6

2.2 Schematic of final phases in the microstructure of heat-treated SiOC materials [12, 13, 15, 29, 31]. 8

2.3 Homogeneous and inhomogeneous distribution of carbon in an SiOC matrix after heat-treatment at different temperatures, as observed by HRTEM [34]. Carbon clusters are indicated by a circle. 9

2.4 The variation of G mode spectral center and I(D)/I(G) intensity ratios with the crystalline order of carbon [35]. 11

2.5 a) Three-dimensional and b) two-dimensional schematic representation of crystalline silica and c) three-dimensional and d) two-dimensional schematic representation of amorphous silica [43]. 13

2.6 a) Schematic representation of the Si-O-Si bond angle (β_0) [49], b) distribution of the Si-O-Si bond angle as measured by XRD [44], c) calculated distribution of the Si-O-Si bond angle [44], d) vibrational modes of the Si-O-Si bond [47], and e) pantograph mechanism of deformation in amorphous silica [50]. 15

2.7 Crystal structure of the stishovite polymorph of silica. The figure is redrawn from [60]. White circles represent oxygen atoms and grey circles are silicon atoms. 16

2.8 Two proposed microstructural configurations for polymer-derived SiOC materials a) isolated carbon clusters within an amorphous silica matrix and b) an interconnected carbon network with silica filling the voids [29]. 18

2.9 Contour plot of the ^{29}Si two-dimensional correlation NMR spectrum of a polysiloxane-derived SiOC PDC of composition $SiO_{1.5}C_{0.68}$ pyrolyzed at 1100 °C [69]. 19

2.10 Formation of large surface defects in sol-gel derived SiOC thin films on a silicon substrate after heat-treatment at 1200 °C [85]. 21

2.11 Effect of 250 keV N^{2+} ion irradiation on the hardness of sol-gel films pre-heat-treated at 300°C and 800°C. The full symbols represent the specimens preheated at 300°C and the empty symbols represent the specimens pre-heat-treated at 800°C [21]. . . . 23

3.1 Preparation of a) acid-catalyzed sols and b) base-catalyzed sols. The numbers indicate the sequence of addition [87]. 25

3.2 Schematic of different scattering mechanisms during Raman and FT-IR spectroscopy. 29

4.1 SEM images from sol-gel thin films, a) green film b) heat-treated at 800 °C c) ion irradiated with N^{2+} ions with a fluence of 10^{15} ions/cm^2 and d) irradiated with N^{2+} ions with a fluence of 10^{15} ions/cm^2 at 320,000X. 34

4.2 Atomic concentration ratios of hydrogen, carbon, and oxygen compared to silicon for films irradiated with a) H^+ and b) N^{2+} ions. 35

4.3 Atomic concentration ratios of carbon, and oxygen compared to silicon for heat-treated thin films [87]. The horizontal line is the theoretical composition of SiO_2. . . 36

4.4 Variations in the density of H^+ and N^{2+} irradiated films as a function of fluence. . . 37

4.5 XRD patterns of H^+ and N^{2+} irradiatied thin films. 38

4.6 Transmission FT-IR spectra of heat-treated thin films. 39

4.7 Transmission FT-IR spectra of the H^+ irradiated thin films. 40

4.8 Transmission FT-IR spectra of the N^{2+} irradiated thin films. 41

4.9 Reflection FT-IR spectra of the H^+ irradiated, N^{2+} irradiated, and heat-treated films. 42

4.10 (a) Schematic of changes in the location of electron clouds and repulsive electrostatic forces (F_1, F_2, F_3) in a carbon incorporated silica tetrahedra as a result of electronegativity difference between carbon and oxygen, (b) the resulting decrease in the Si-O-Si bond angle as the result of carbon incorporation. The figure is adapted from [110]. . 43

4.11 Raman spectra of the films heat-treated at a) 500 °C and b) 800 °C. 45

4.12 Raman spectra of the H^+ irradiated films at different fluences: a) 10^{13} ions/cm^2 b) 10^{14} ions/cm^2 c) 10^{15} ions/cm^2 d) 10^{16} ions/cm^2 e) 10^{17} ions/cm^2 and f) 2×10^{17} ions/cm^2. 46

4.13 Raman spectra of the N^{2+} irradiated films at different fluences: a) 10^{13} ions/cm^2 b) 10^{15} ions/cm^2 and c) 5×10^{15} ions/cm^2. 47

4.14 Raman spectra of two H^+ irradiated films at fluences of 10^{14} and 2×10^{17} ions/cm^2. . 50

4.15 Photoluminescence spectra of ion irradiated films that possess free carbon clusters. The peaks between 550-600 nm and 625-650 nm are carbon Raman modes. 51

4.16 The XPS Si 2p spectra after irradiation with N^{2+} ions. For comparison, the XPS spectra of a heat-treated film is also included. 52
4.17 XPS C 1s spectra of the films irradiated with N^{2+} ions. For comparison, the XPS spectra of a heat-treated film is also included. 53
4.18 Chemical composition triangle of a) H^+ ion irradiated b) N^{2+} ion irradiated and c) heat-treated films, predicting the final phases present within the films based on a model developed for heat-treated films 55
4.19 Microstructural configuration of films after irradiation with a) H^+ ions at a fluence of 2×10^{17} ions/cm^2 and b) N^{2+} ions at a fluence of 5×10^{15} ions/cm^2. 57
4.20 The variations in film thickness, reduced elastic modulus and hardness of ion irradiated films as a function of fluence for a) H^+ irradiated films and b) N^{2+} irradiated films. The data is adapted from [158]. 61
4.21 Atomic concentration ratios of hydrogen, carbon, and oxygen compared to silicon after ion irradiation with a) 1 MeV Cu^+ b) 4 MeV Cu^{2+}, and b) 9 MeV Cu^{3+}. . . . 64
4.22 Estimated density of the films irradiated with 1 MeV Cu^+, 4 MeV Cu^{2+}, and 9 MeV Cu^{3+}. 65
4.23 Transmission FT-IR spectra of the films irradiated with 1 MeV Cu^+ ions at different fluences. 66
4.24 Transmission FT-IR spectra of the films irradiated with 4 MeV Cu^{2+} ions at different fluences. 68
4.25 Transmission FT-IR spectra of the films irradiated with the 9 MeV Cu^{3+} ions at different fluences. 70
4.26 Reflection FT-IR spectra of the 1 MeV Cu^+, 4 MeV Cu^{2+}, and 9 MeV Cu^{3+} irradiated films at different fluences. The FT-IR spectra of 4 MeV Cu^{2+}, and 9 MeV Cu^{3+} irradiated films with fluences of 10^{15} ions/cm^2 and 10^{16} ions/cm^2 is overwhelmed by a fringe pattern. 71
4.27 Raman spectra of the collected (solid line) and fitted (dashed line) silica Raman modes of ion irradiated films with 1 MeV Cu^+, 4 MeV Cu^{2+}, and 9 MeV Cu^{3+} ions. The vertical lines indicate lowest and highest center of the ω_1 Raman mode. The sharp Raman mode at 520 cm^{-1} is related to silicon substrate. 72
4.28 Raman spectra of the 1 MeV Cu^+ ion irradiated films at different fluences. 75
4.29 Raman spectra of the 4 MeV Cu^{2+} ion irradiated films at different fluences. 76
4.30 Raman spectra of the 9 MeV Cu^{3+} ion irradiated films at different fluences. 76

4.31 The XPS Si 2p spectra after irradiation with heavy ions. For comparison, the XPS spectra of heat-treated film is also included. 78
4.32 The XPS Si 2p spectra of heat-treated, light-ion irradiated and heavy-ion irradiated films. A shift toward lower binding energies with increasing ion energies can be observed. 79
4.33 XPS C 1s spectra of the films irradiated with heavy ions. 80
4.34 XPS C 1s spectra of 9 MeV Cu^{3+} irradiated film with a fluence of 10^{16} ions/cm^2 and N^{2+} irradiated film with a fluence of $5{\times}10^{15}$ ions/cm^2. The vertical lines indicate the binding energy of sp^2 bonded and sp^3 bonded carbon. 81
4.35 XPS spectra of the films ion irradiated with both light and heavy ions. The heat-treated film spectrum is also plotted for comparison. 84
4.36 Chemical composition triangle of films irradiated with a) 1 MeV Cu^{+} b) 4 MeV Cu^{2+}, and c) 9 MeV Cu^{3+}, predicting the final phases present within the ion-irradiated films based on a model developed for heat-treated films. 85
4.37 Microstructural configuration of films irradiated with different ion energies after irradiation with a fluence of 10^{16} ions/cm^2, a) 1 MeV Cu^{+}, b) 4 MeV Cu^{2+}, and c) 9 MeV Cu^{3+}. 86
4.38 Film thickness, hardness, and reduced elastic modulus of the films after ion irradiation with a) 1 MeV Cu^{+} b) 4 MeV Cu^{2+} and c) 9 MeV Cu^{3+}. The data is adapted from [158]. 89
4.39 SEM images of base-catalyzed thin films a) ion irradiated with N^{2+} ions with a fluence of 10^{16} ions/cm^2 and b) the same film after heat-treatment at 1100 °C. The arrows indicate the formed cracks. 90
4.40 Reflection FT-IR spectra of the ion irradiated base-catalyzed films after a secondary heat-treatment at 1100 °C. 92
4.41 Reflection FT-IR spectra of the ion irradiated base-catalyzed films after a secondary heat-treatment at 1350 °C. 93
4.42 XRD pattern of a based-catalyzed ion irradiated film after ion irradiation with N^{2+} ions at 10^{16} ions/cm^2 and a secondary heat-treatment at 1350 °C. The observed XRD peaks correspond to the XRD pattern of α-cristobalite (JCPDS Number: 39-1425). . 93
4.43 Raman spectroscopy results of base-catalyzed ion irradiated films after secondary heat-treatment at 1100 °C. 94
4.44 XRD Pattern of unirradiated acid-catalyzed films after heat-treatment at 1350 °C. The observed XRD peaks correspond to the XRD pattern of α-cristobalite (JCPDS Number: 39-1425). 96

A.1 Curve fitting results of C 1s spectra of N^{2+} irradiated film with a fluence of 5×10^{15} ions/cm^2. The C-C, C=O, and C-O peaks are indicated in the figure. 123

A.2 Curve fitting results of C 1s spectra of Cu^{3+} irradiated film with a fluence of 10^{16} ions/cm^2. The C-C, C=O, and C-O peaks are indicated in the figure. 124

B.1 XPS O 1s spectra of the films irradiated with light ions. 125

B.2 XPS O 1s spectra of the films irradiated with heavy ions. 126

C.1 Raman spectra of fused silica. 127

C.2 Raman spectra of the heat-treated acid-catalyzed film after heat-treatment at 800 °C. 128

E.1 Room temperature and low temperature photoluminescence spectra of the 1 MeV Cu^{+} irradiated film with a fluence of 10^{16} ions/cm^2 in the 380-480 nm range. 132

E.2 Room temperature and low temperature photoluminescence spectra of the 1 MeV Cu^{+} irradiated film with a fluence of 10^{16} ions/cm^2 in the 660-740 nm range. 133

E.3 Room temperature and low temperature photoluminescence spectra of the 9 MeV Cu^{3+} irradiated film with a fluence of 10^{16} ions/cm^2 in the 380-480 nm range. 134

E.4 Room temperature and low temperature photoluminescence spectra of the 9 MeV Cu^{3+} irradiated film with a fluence of 10^{16} ions/cm^2 in the 660-740 nm range. 135

NOMENCLATURE

AFM .... Atomic force microscopy

BWF .... Breot-Wigner-Fano

CCD .... Charge-coupled device

DFT .... Density functional theory

ERA .... Embedded ring approach

ERD .... Elastic recoil detection

FE-SEM .... Field-emission scanning electron microscopy

FT-IR .... Fourier transform infrared

FWHM .... Full width at half maximum

HPCS .... Hydridopolycarbosilane

HRTEM .... High resolution transmission electron microscopy

IR .... Infrared

j .... Vibrational level

JCPDS .... Joint Committee on Powder Diffraction Standards

k_b .... Boltzmann constant

L_a .... Carbon cluster size

LO .... Longitudinal optical

MTES .... Methyltriethoxysilane

N .... Total number of molecules

N.A. .... Numerical aperture

NMR .... Nuclear magnetic resonance

PCS .... Polycarbosilane

PDC .... Polymer-derived ceramics

PTES .... Phenyltriethoxysilane

RBS .... Rutherford backscattering spectrometry

SAXS .... Small angle X-ray scattering

SEM .... Scanning electron microscopy

SPM .... Scanning probe microscopy

SRIM .... Stopping and range of ions in matter

T .... Temperature

TEM .... Transmission electron microscopy

TEOS .... Tetraethylorthosilicate

TO .... Transverse optical

UV .... Ultra-violet

VDOS .... Virtual density of states

XPS .... X-ray photoelectric spectroscopy

XRD .... X-ray diffraction

Z .... Atomic number

θ .... Angle between x-ray and scattering plane

λ .... Wavelength

Chapter 1

INTRODUCTION

1.1 Motivation for the present study

High volume and low cost production of complex optics (aspheric lenses, free-form lenses, and lens arrays) requires the creation of wear resistant molds. These optics are manufactured by injection molding of plastic or the hot pressing of glass. Traditionally, injection-molding molds were made through multi-stage precision machining and grinding of steel alloys [1,2]. Diamond machining of the molds is more efficient and economical than a multi-stage process. However, steel acts as a catalyst for conversion of diamond to graphite and thus severe tool wear occurs during diamond machining of steel. Other metallic materials lack the hardness and wear resistance required for optical molds or are difficult to process.

Sol-gel derived organic-inorganic coatings are a suitable alternative for fabrication of the molds. The incorporation of organic materials into an inorganic system allows for workability in the green state followed by hardness and wear resistance after a conversion process. The main advantage of the organic-inorganic films in comparison to pure inorganic films is in their high critical thickness. Critical thickness is defined as the maximum crack-free film thickness that can be obtained after solvent removal [3]. For pure inorganic films (e.g., sol-gel derived ZrO_2 films), the critical thickness was found to be a few hundred nanometers [4], whereas a critical thickness of up to 5 μm can be achieved in organic-inorganic films [5]. Also, multi-layer coatings were found to create crack-free coatings of 18 μm [6]. Figure 1.1 shows the macroscopic and scanning electron microscopy (SEM) images of successful diamond machining of sol-gel derived organic-inorganic coatings.

Both ion irradiation and heat treatment have been used to convert the organic-inorganic coatings into their final inorganic phase. The conversion process is necessary to increase the hardness of the

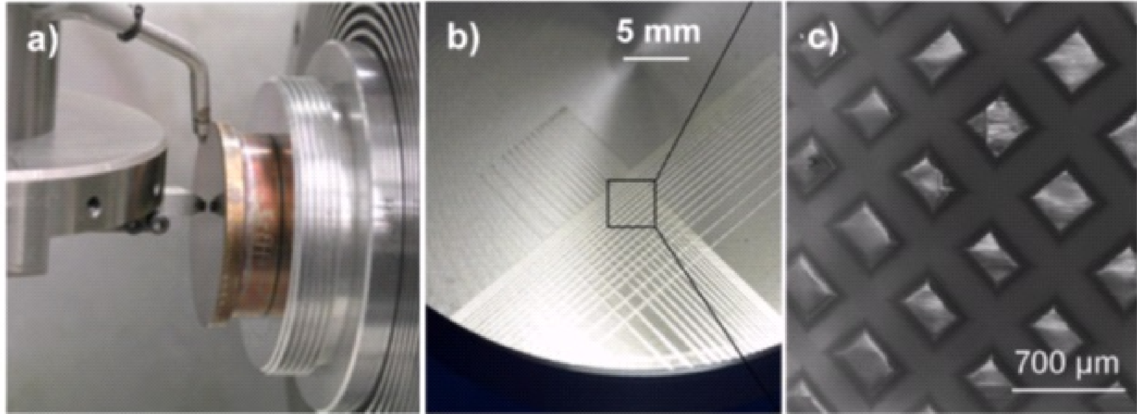

Figure 1.1: a) Diamond turning of a sol-gel coated steel mold b) steel mold with a micro-machined sol-gel derived coating c) SEM image of the micro-machined coated surface [2].

coating. Ion irradiation has many advantages over heat treatment. During heat treatment both carbon and hydrogen loss are observed, while ion irradiation leads to selective release of hydrogen and maintains the carbon within the films. The presence of carbon opens the door for the creation of many novel secondary phases in the films. Also, the hardness of the thin films is enhanced if ion irradiation is used instead of heat treatment [7]. In addition, tailoring the mechanical properties of the films using ion irradiation is possible. These advantages make ion irradiation more favorable than heat treatment in the conversion of sol-gel derived films.

1.2 Objectives

In 2001, the Transregional Collaborative Research Center SFB/TR4 entitled "'Process Chains for the Replication of Complex Optical Components"' was started as a collaborative project between Oklahoma State University, University of Bremen and RWTH Aachen University. The goal of this project was to improve the accuracy of replicated complex optics. The goal of the current project is to further investigate the fundamental chemical and microstructural nature and evolution of ion irradiated sol-gel derived thin films. The results will be useful for investigating possible new applications for the films and enhance performance for the current application. While the microstructure and mechanical properties of heat treated films have been studied extensively, there is little insight into ion irradiated sol-gel derived thin films. One major shortcoming in previous studies on sol-gel derived ion irradiated films is the assumption that the phases formed during ion irradiation and heat treatment are identical and the effects of ion irradiation is limited to changes

in the chemical composition of the films; whereas there exists empirical evidence that the nature of the phases formed during ion irradiation and heat treatment are different. This study aims to study the effects of ion irradiation on both the chemical composition of the films, as well as changes in the structure of individual phases formed during ion irradiation.

In order to achieve these goals, a variety of analytical techniques including scanning electron microscopy (SEM), atomic force microscopy (AFM), Raman spectroscopy, Fourier transform infrared (FT-IR) spectroscopy, Photoluminescence (PL) spectroscopy, X-ray diffraction (XRD), elastic recoil detection (ERD), Rutherford backscattering spectrometry (RBS), and X-Ray Photoelectron Spectroscopy (XPS) were utilized to study the chemical, microstructural, and mechanical properties of the films. It is expected that the combination of these techniques helps to understand the microstructure of the films after ion irradiation which is necessary for further improvement of the mechanical properties of the films. It is also essential for identifying other potential applications of the ion irradiated films.

Chapter 2

BACKGROUND

2.1 Silica-based sol-gel thin films

The main focus of the present study is to investigate the microstructure and chemical properties of ion irradiated sol-gel derived silica-based thin films and the effect of microstructure on the mechanical properties of the films. One example of the application of these films, mold coating, requires wear resistance. Even though steel possesses the necessary hardness, diamond turning of steel is not economical because of tool wear. Other metallic compounds do not have the hardness required for this application. The hardness of ceramic coatings, including sol-gel derived ZrO_2 is suitable for this application [8]. However, the critical film thickness of ceramic materials, the maximum achievable crack-free thickness after solvent removal, is only a few hundred nanometers [4]. The proposed solution to this problem is utilization of a hybrid organic-inorganic thin film that is machinable in the green state, and can later be converted to a hard ceramic coating by either heat-treatment or ion irradiation.

Sol-gel derived silica-based thin films obtained from tetraethylorthosilicate (TEOS) and methyltriethoxysilane (MTES) have the required properties to be used for this application and successful diamond-machining of these films has been reported [3]. These films have a critical thickness of 5 μm and, using multiple layers, a critical thickness of 18 μm is also achievable [6].

TEOS/MTES sol-gel films convert to an amorphous silicon oxycarbide (SiOC) thin film after a conversion process. SiOC materials have been extensively investigated before due to their mechanical, electrical [9], optical [10], and chemical [11] properties.

2.2 Polymer-derived SiOC ceramic materials

Polymer-derived ceramics (PDCs) were first developed for the synthesis of non-oxide ceramics from polymeric materials [12], and since have been largely developed for applications such as synthesis of silicon carbide fibers, ceramic-matrix composites, porous components, coatings, MEMS devices, and optoelectronic devices [13]. PDC films and components provide many unique properties. Tailoring chemical, mechanical, and optical properties of the final ceramic state is possible by introducing various organic components [14]. It is also possible to synthesize a range of secondary nanoscale phases in the ceramic matrix to improve the functionality of the system [15]. Currently, the synthesis of many ternary composites like SiC-SiO_2-C and SiC-Si_3N_4-C can only be achieved in PDCs [13].

The successful synthesis of various PDCs depends on the starting materials. If films are converted by heat-treatment, strong bonding of carbon and silicon is necessary to maintain carbon within the films during pyrolysis by preventing carbon release as hydrocarbon molecules. As mentioned in Chapter 1, the current study requires films with improved critical thickness and so the selection of the starting materials was based upon achieving thicker crack-free films. A mixture of TEOS and MTES has been shown to achieve a critical thickness of 18 μm. The molecular structures of TEOS and MTES are presented in Fig 2.1. During heat-treatment of pure TEOS, ethyl groups (C_2H_5) are released at about 250 °C, leaving behind an Si-O-Si network in the form of an amorphous silica phase [16]. In MTES, a methyl group (CH_3) replaces one of the oxygen-ethyl groups of the TEOS structure. However, the Si-C bonds do not break until 500 °C [17]. So the decomposition of a mixture of TEOS/MTES occurs over a range of temperatures. The gradual decomposition of TEOS/MTES is the key factor in increasing the critical thickness of the prepared films. Since the decomposition is gradual, the induced stress from volumetric shrinkage is also applied gradually, and thus thicker crack-free films are achievable. Even though this leads to a film with high critical thickness, most of the carbon is lost during the conversion of TEOS/MTES into the final ceramic form.

The films are usually produced using a sol-gel method which is based on hydrolysis and condensation of a metallic alkoxide. Alkoxides are metalorganic components with the general formula of Met$(OR)_n$, where Met is the metal (e.g., silicon) and OR is the alkoxy group (e.g., R= CH_3, CH_2CH_3, etc.). Initially, pyrolysis occurs and silanol (Si-OH) replaces the OR group. The next step is gelation during which silicon and oxygen form a network. During thin film deposition, gelation and solvent removal occur simultaneously. The resulting wet gel is then dried to form a porous xerogel, which can in turn be converted to a ceramic using heat-treatment or ion irradiation.

After decomposition through heat-treatment or ion irradiation, assuming that some carbon is

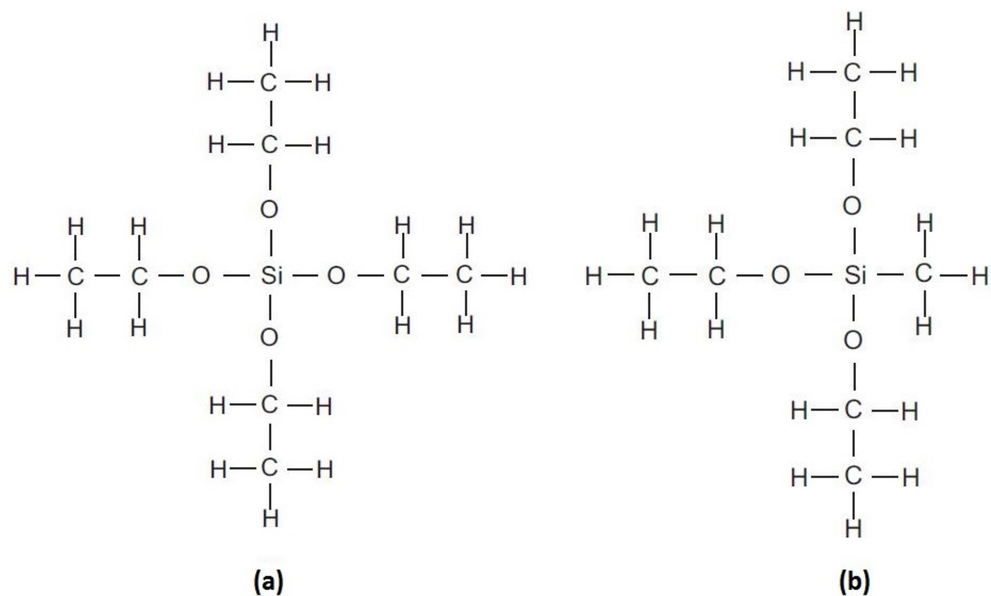

Figure 2.1: The molecular structure of a) TEOS and b) MTES.

left within the films, the thin films consist of silicon oxycarbide (SiOC). The silicon oxycarbide, or black glass, is defined as a chemical structure where silicon is simultaneously bonded to oxygen and carbon [18].

2.3 Ion irradiation of polymers

Ion irradiation is used for many processes including synthesis, surface modification, doping, and conversion. Ion beam modification of polymers has found many applications including cross-linking, polymerization of monomers, synthesis of inorganic compounds, and modification of electronic states [19]. Conversion of organic films to a final ceramic state using ion irradiation has been previously studied. Many authors have used ion irradiation to convert different kinds of polymers into their ceramic state. Specifically, the conversion of polymers into silicon oxycarbide materials using ion irradiation has been shown to increase the hardness and thermal stability of the final films [20]. Heat-treatment of MTES and TEOS causes the release of both hydrogen and carbon, leading to limited carbon content after heat-treatment [21]. One of the main advantages of ion beam conversion of polymers into ceramics is the selective release of hydrogen from the films [22, 23] and therefore, ion irradiation preserves the carbon in the films. The presence of excess carbon in the final material is crucial for the formation of silicon carbide and carbon nanoparticles. Kurmaev et al. [24]

converted phenyltriethoxysilane (PTES) into SiOC films by irradiating the films with gold or carbon ions, followed by a heat-treatment at 1000 °C. It was shown that although ion irradiation fully converted the films into a ceramic state, heat-treatment was necessary for the formation of sp^2 hybridized carbon clusters in the films. However, others [22,23] have provided results on the formation of carbon clusters in polymer derived films using only ion irradiation. The formation of diamond-like carbon clusters by ion irradiation of a combination of polysiloxanes and polycarbosilanes has also been claimed before [22]. Ion irradiation followed by heat-treatment has also been investigated and it was found that subsequent heat-treatment at 1000 °C reduced the amount of sp^3 bonded carbon [25]. The nature of the formed carbon during ion irradiation varies depending on irradiation conditions and the starting polymeric materials.

2.4 Microstructure of SiOC ceramics

The final microstructure of polymer-derived ceramics after the decomposition of the starting organic materials depends on a variety of parameters including decomposition method (e.g., heat-treatment or ion irradiation), starting organic materials, and any subsequent treatment. However, the main phases that might be present after conversion are free carbon, amorphous silica, silicon carbide, and silicon. The presence of other phases like silicon nitride has also been observed for SiCN polymer derived ceramics [26].

The difficulty in studying the microstructure of this class of materials is the small size ($\leq$10 nm) of constituent phases, known as nanodomains. The green films usually have a random, glassy structure, as confirmed by TEM, Raman spectroscopy, and XRD [27]. Subsequent heat-treatment of the green films leads to phase separation and formation of nanodomains. The presence of nanodomains has been confirmed by TEM [28], small-angle x-ray scattering (SAXS) [29], and neutron scattering [30]. The microstructure of ion irradiated films was found to be heterogeneous, as evidence of free carbon domains was observed by Raman spectroscopy of the irradiated films [25]. The small size of the nanodomains and their amorphous nature renders many conventional characterization techniques unsuitable for studying the microstructure of SiOC films.

The effect of composition on the final phases present in the microstructure of heat-treated specimens has been extensively investigated [12,13,15,29,31] and a summary of the results is presented in Fig. 2.2. It should be noted that this figure does not present an actual ternary phase diagram, as it does not show the changes in the phase composition in different temperatures, and is merely designed for better understanding of the effect of composition on the microstructure. Since the

triangle relies upon limited concentration of broken bonds and vacancies in the constituent phases, it is valid only for heat-treated specimens. Each of these phases will be further discussed in the following sections. The predicted phases in Fig 2.2 indicate the phases formed after full thermal decomposition and phase separation and does not take into account the possible effects of chemical reactions. For example, a SiOC material with the chemical composition of $SiO_{6.5}C_{2.5}$ (10% Si, 65% O, 25% C) is located in the C-O-SiO_2 triangle and thus the final composition of such materials system will only include amorphous silica and carbon.

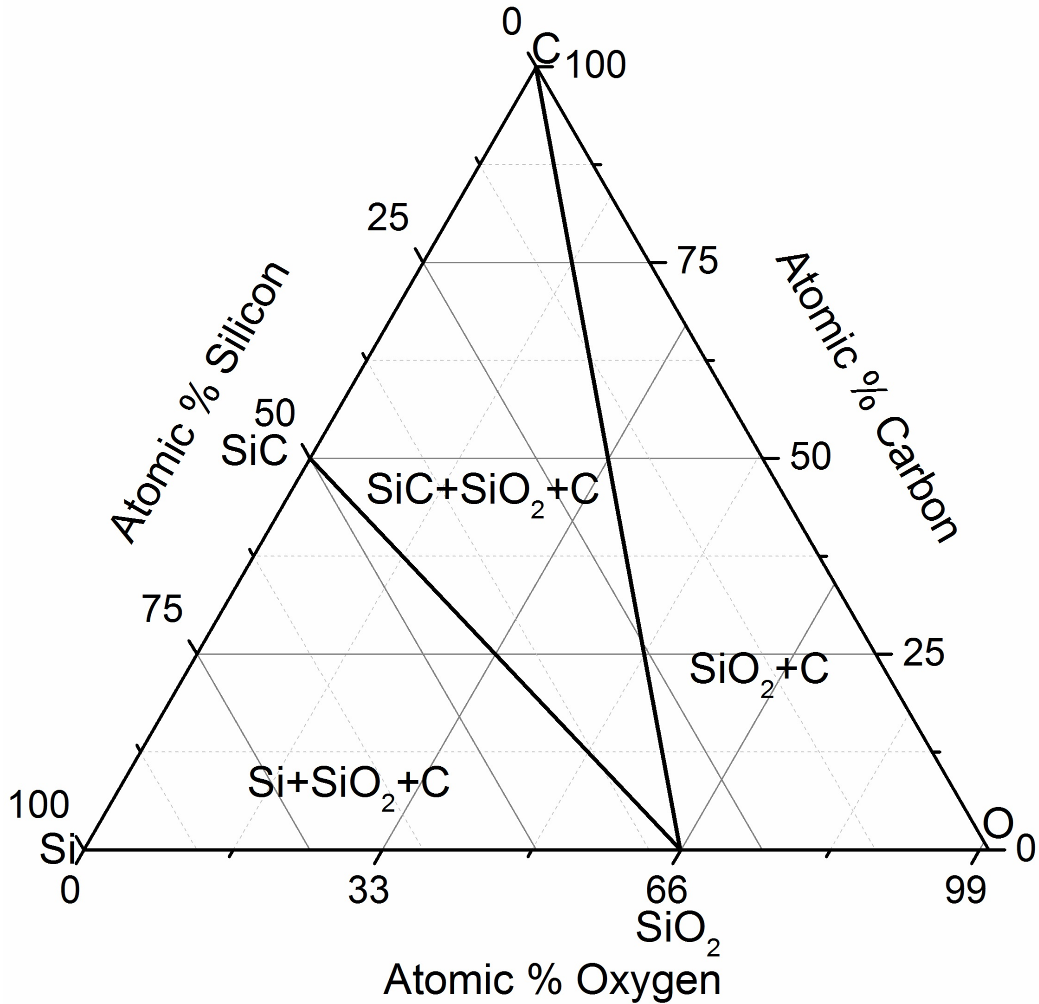

Figure 2.2: Schematic of final phases in the microstructure of heat-treated SiOC materials [12, 13, 15, 29, 31].

2.4.1 Carbon

It has been reported that if the chemical composition of the heat-treated SiOC films has excess carbon (more carbon than the amount required for the saturation of the silicon valences), the conversion process leads to the formation of free carbon in the films [13]. Many studies have confirmed the formation of free carbon, using either Raman spectroscopy or TEM [32]. It has been reported that excess carbon is dispersed homogeneously at low temperatures (as a solid-solution), but as the heat-treatment temperature increases, the carbon distribution becomes more inhomogeneous [33]. Figure 2.3 shows HRTEM images of homogeneous and inhomogenous carbon distribution in SiOC ceramics [34]. Other than TEM, Raman spectroscopy is an important tool for characterization of free carbon in the films [35]. It is possible to use Raman spectroscopy to analyze the nature of carbon bonding and hybridization of sp^2 and sp^3 bonds. A model for quantitative Raman analysis of free carbon concentration has also been developed for polymer-derived SiCN ceramics [36].

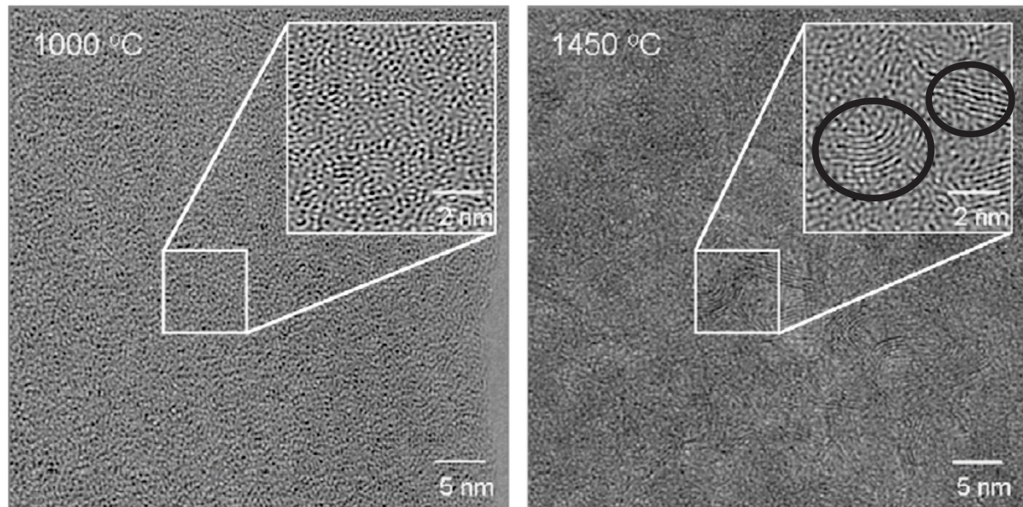

Figure 2.3: Homogeneous and inhomogeneous distribution of carbon in an SiOC matrix after heat-treatment at different temperatures, as observed by HRTEM [34]. Carbon clusters are indicated by a circle.

Formation of free carbon clusters in ion irradiated films is a result of a different synthesis mechanism. Ion irradiation breaks the C-H bonds. Then, hydrogen is released from the irradiated film as H_2 gas, leaving carbon behind [37]. Subsequently, carbon either bonds with other carbon atoms to form free carbon or bonds with silicon and enters the silica network. As a result, there would be no homogenous dispersion of carbon in the ion irradiated films after decomposition.

Raman spectroscopy is a powerful tool for studying carbon materials, especially disordered and

amorphous carbon [35, 38–40]. The Raman spectra of graphite consists of two distinct D and G modes. The G mode is the E_{2g} mode, originated from in-plane vibrations. The D mode is the disorder-induced mode, resulting from selection rule relaxation and is related to A_{1g} symmetry. D mode is forbidden in perfect graphite and its presence is an indication of defects in the six-fold structure of graphite. However, D mode intensity is strictly connected to the presence of six-fold graphitic structure, whereas the G mode is due to in-plane motions and can occur even in chains [35]. Crystalline diamond has a single Raman mode, T_{2g} at 1332 cm^{-1}. However, the Raman spectra of amorphous and disordered carbon, with a mixture of sp^2 and sp^3 bonded carbon, is dominated by the D and G modes.

A widely accepted model based on the spectral center of the G mode and the intensity ratio of the D and G modes has been used to identify the nature of amorphous carbon [35]. A schematic of the model is presented in Fig. 2.4. Ordered graphite (e.g., an infinite sheet of stacked graphene) has no D mode and its G mode is centered at 1582 cm^{-1}. However, the Raman spectra changes depending on the clustering of the sp^2 phase, bond disorder, and sp^2/sp^3 concentration ratio.

As graphene transforms to nanocrystalline graphite, there is an increase in the G mode spectral center from 1582 cm^{-1} to 1600 cm^{-1} and the intensity of the D mode increases as well. The increase in the G mode spectral center is related to the development of a new defect-induced mode, D' at 1620 cm^{-1} due to selection rules relaxation [41]. D' is not distinguishable from G mode and their combined mode is located at a higher spectral center than G mode. The increase in G mode spectra center and D mode intensity are observed by transitioning from graphene to nanocrystalline graphite with cluster size of 20 Å. If more damage is introduced into the nanocrystalline graphite, the G mode shifts to lower wavenumbers and the intensity of the D mode also decreases. The decrease in the spectral center is related to the softening of the vibrational density of states (VDOS) as a result of bond-bending and a change in bond angle [42]. Also, the destruction of graphitic six-fold rings causes a decrease in the D mode intensity. At this stage, there is a possibility that a limited concentration of sp^3 bonded carbon is also present. Finally, if the sp^3 content of amorphous carbon is increased, an increase in the spectral center of the G mode and disappearance of the D mode is expected. When a limited concentration of sp^2 bonded carbon is embedded within a sp^3 matrix, it tends to form olefinic groups instead of graphitic six-fold rings which explains both the increase in the G mode center as well as the disappearance of the D mode.

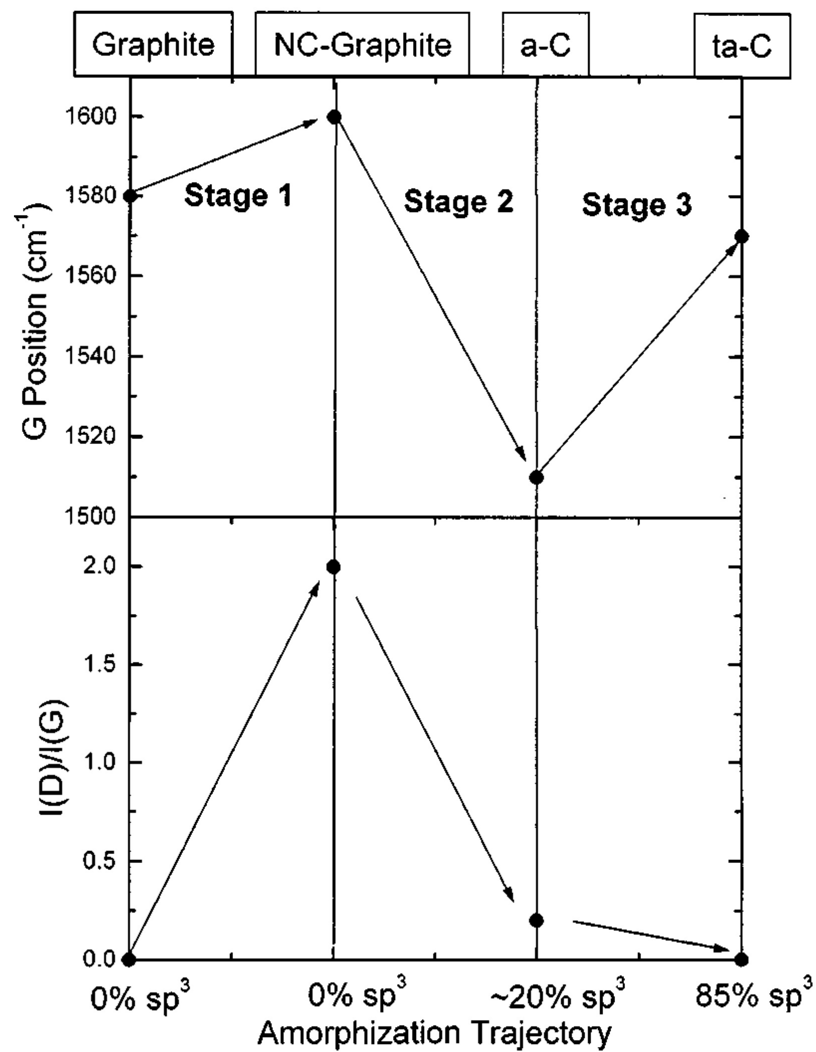

Figure 2.4: The variation of G mode spectral center and I(D)/I(G) intensity ratios with the crystalline order of carbon [35].

2.4.2 Amorphous silica

Amorphous silica is the major phase in an SiOC system. It forms in the early stages of the sol-gel process, as gelation begins. Unlike silicon carbide, silicon, or free carbon, amorphous silica is always observed in an SiOC material system. Although amorphous silica crystallizes into α-cristobalite at around 1200 °C, it has been reported that silica in SiOC specimens derived from heat-treatment remains amorphous even at temperatures as high as 1800 °C [13]. Many authors have utilized the resistance of silica to crystallization to propose microstructural models for SiOC ceramics, as will be discussed in Section 2.4.5. Silicon oxycarbide glasses are defined as chemical compounds that silicon is bonded to both carbon and oxygen. Thus, it is expected that a portion of carbon is incorporated within the amorphous silica network.

At ambient pressures, amorphous silica, the noncrystalline polymorph of SiO_2, consists of SiO_4 tetrahedra units, similar to crystalline silica. Each silicon atom is bonded to four oxygen atoms (thus building the SiO_4 tetrahedra unit) and each oxygen atom is bound to two silicon atoms. These tetrahedra are the result of four sp^3 orbitals of silicon and two 2p orbitals of oxygen atoms making bonding [43]. The structure of silica is built from the arrangement of these tetrahedra. Each two adjacent tetrahedra share only one corner (i.e., an oxygen atom). But all the corners of the tetrahedra are shared. Figure 2.5 shows the structure of silica both in crystalline and amorphous form. In both quartz and α-cristobalite, the tetrahedra are usually formed in six-member rings. A variety of ring sizes might be present in amorphous silica, but the average ring of fused silica is made of six tetrahedra. The tetrahedra in SiOC are in the form of SiO_xC_y, where one or more oxygen atoms are replaced with carbon.

One major defining feature of amorphous silica is the bond angle of the Si-O-Si bond. This bond angle is between the oxygen atom that bridges two adjacent tetrahedra and the silicon atoms from the adjacent tetrahedra, and is shown schematically in Fig. 2.6 (a). It has been previously shown that fused silica has a wide distribution of bond angles ranging from 120° to 180°, with an average of 144° [44]. Figure 2.6 (b) and (c) show the measured and calculated distributions of the bond angle of Si-O-Si bond in fused silica. A number of analytical techniques are capable of measuring the bond angle of amorphous silica, including radial distribution function analysis of XRD pattern [45], FT-IR spectroscopy [46, 47], and nuclear magnetic resonance (NMR) spectroscopy [48]. In the case of FT-IR spectroscopy, the spectral center of the Si-O-Si related transverse optical (TO) mode is sensitive to the angle of the Si-O-Si bonds.

Figure 2.6 (d) shows the vibrational modes of the Si-O-Si bond. The TO mode originates from

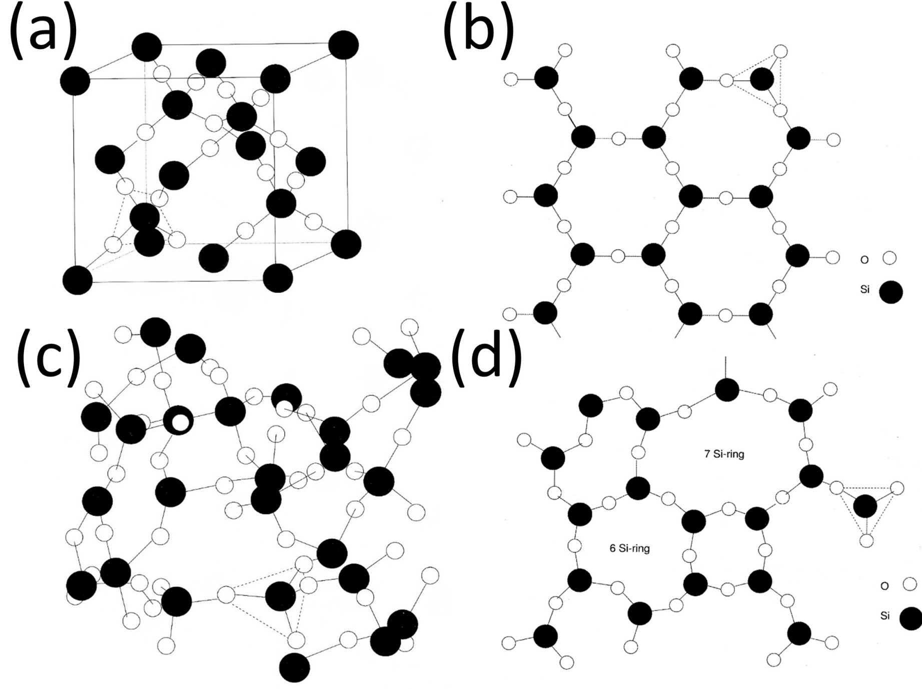

Figure 2.5: a) Three-dimensional and b) two-dimensional schematic representation of crystalline silica and c) three-dimensional and d) two-dimensional schematic representation of amorphous silica [43].

assymetrical stretching of the oxygen atom. Previous studies have shown the following relationship between the bond angle (θ) and the spectral center of the TO mode (ω) [46, 47, 51, 52]:

$$\omega = a[2(\alpha \sin^2 \theta/2 + \beta \cos^2 \theta/2)/m]^{1/2} \tag{2.1}$$

where m is the mass of the central atom (i.e., oxygen) with the value of 16 amu (2.657×10^{-26} kg), a is a constant (5.305×10^{-12}), and α and β are the central and non-central force constants, respectively. For small bond angles ($\theta\leq 150°$), the values of α and β are reported as 582 and 264, respectively [51].

A more simplified relationship between the bond angle and TO spectral center is proposed as:

$$\omega = \omega_0 \sin(\theta/2) \tag{2.2}$$

where ω_0 is a constant with a value of 1134 cm^{-1} [53].

The bond angle and the tetrahedra ring size are related, and a decrease in the bond angle of Si-O-Si decreases the tetrahedra ring size in amorphous silica [51].

The Si-O-Si bond angle has an impact on the mechanical properties of amorphous silica. Under loading, amorphous silica behaves as a perfectly elastic materials with little plastic deformation. It

has been reported that amorphous silica exhibits nonlinear behavior in the elastic region, where an increase in compaction (i.e., a decrease in bond angle) leads to an increase in the elastic modulus of amorphous silica [50]. This nonlinear (non-Hookean) behavior has been explained previously by Mallinder and Proctor [54] by describing the behavior of amorphous silica as a function of free volume. The presence of free volume in the microstructure of amorphous silica leads to an alternative method of deformation, presented in Fig. 2.6 (e), similar to a pantograph. In this process, elastic deformation is achieved by a small distortion of bond angle, rather than by a change in bond length. This alternative deformation mechanism requires smaller forces than changing the bond length [50, 54]. With a decrease in bond angle, the alternative deformation mechanism becomes more difficult and a larger portion of stress is applied to deformation through changing the bond length. This leads to an increase in elastic modulus. Many authors have confirmed the changes in elastic modulus of amorphous silica by changing the bond angle [44, 55]. The increase in the elastic modulus of amorphous silica, as a result of a decrease in Si-O-Si bond angle, has been observed previously in silica films exposed to ion irradiation [56] or pressure [57]. The effect of changes in the bond angle on the mechanical properties of silica has also been observed in self-assembled nanoporous silica as a function of assembly process as well [58]. This nonlinear behavior has also been observed in other materials with high free volume including carbon fibers [59] and bulk metallic glasses [50].

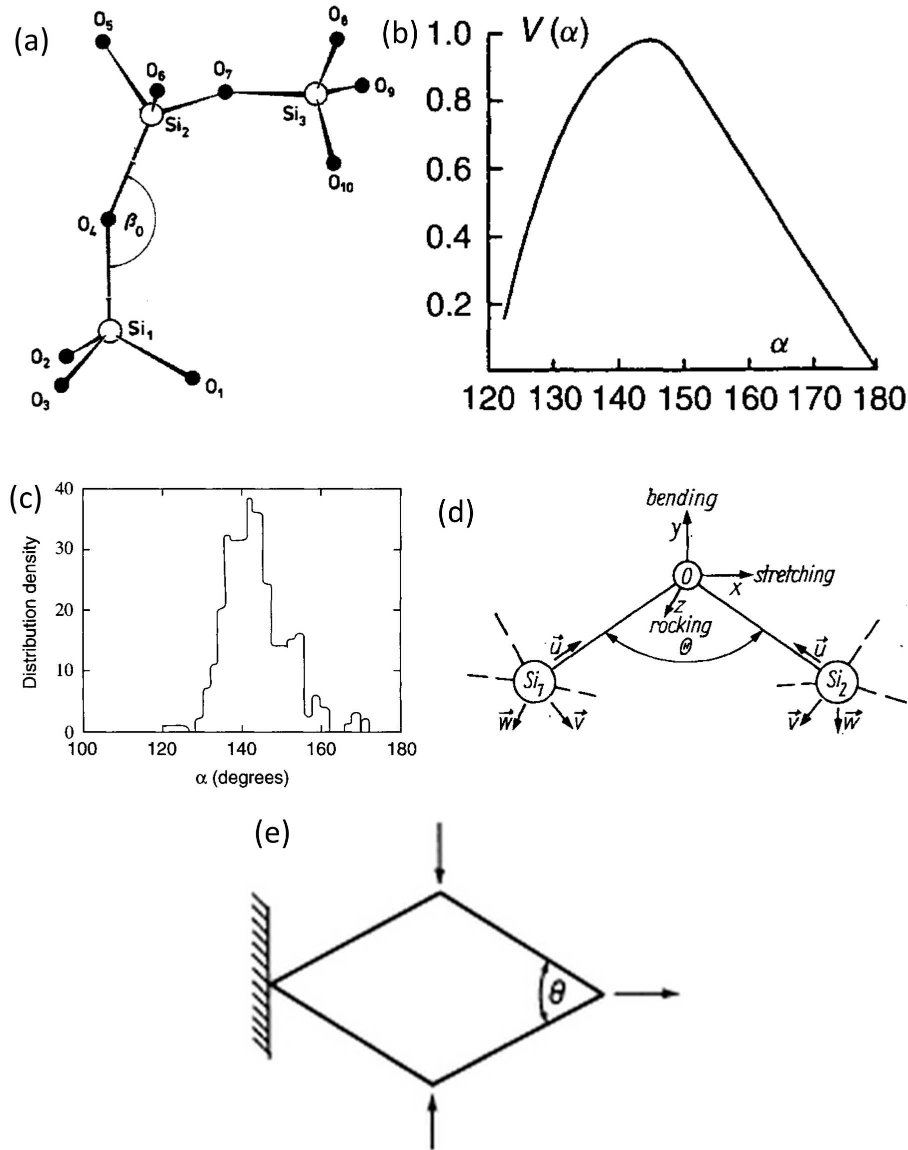

Figure 2.6: a) Schematic representation of the Si-O-Si bond angle (β_0) [49], b) distribution of the Si-O-Si bond angle as measured by XRD [44], c) calculated distribution of the Si-O-Si bond angle [44], d) vibrational modes of the Si-O-Si bond [47], and e) pantograph mechanism of deformation in amorphous silica [50].

Although at ambient pressure, the structure of silica is made from tetrahedrally bonded silicon atoms to oxygen, at high pressure silica undergoes a phase transformation from tetrahedral to octahedral coordination [60]. The high pressure phase of silica is called stishovite and has a rutile structure. As a result of a higher coordination number, stishovite is more dense than fused silica (4.3 versus 2.2 g/cm^3 [61]). In addition, stishovite is one of the stiffest known materials with an elastic modulus of 400 GPa [62]. The crystal structure of stishovite is presented in Fig. 2.7.

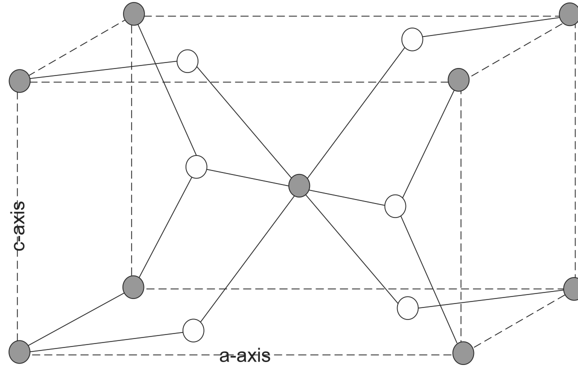

Figure 2.7: Crystal structure of the stishovite polymorph of silica. The figure is redrawn from [60]. White circles represent oxygen atoms and grey circles are silicon atoms.

2.4.3 Silicon carbide

Considering the presence of both silicon and carbon within SiOC systems, the synthesis of silicon carbide within SiOC is possible. In fact, the successful synthesis of silicon carbide within a SiOC matrix has been previously reported [28, 31, 63, 64]. Many of the silicon-containing components, including MTES, TEOS, or a combination of the two have been used for synthesis of both silicon carbide and SiOC [65, 66].

The synthesis of silicon carbide in SiOC is achieved by heat-treatment at temperatures ranging from 1000 °C to 1550 °C, depending on the starting materials. For a combination of TEOS and MTES, along with additional starting materials acting as a carbon source, silicon carbide was synthesized above 1300 °C [65].

The synthesis of silicon carbide within an SiOC matrix is a result of the following reaction [31]:

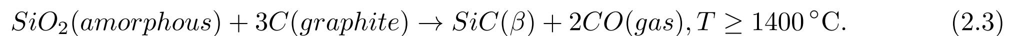

$$SiO_2(amorphous) + 3C(graphite) \rightarrow SiC(\beta) + 2CO(gas), T \geq 1400\,^{\circ}\mathrm{C}. \tag{2.3}$$

If SiOC has been prepared through heat-treatment, silicon carbide also forms in a process known as phase separation. The microstructure of heat-treatment derived SiOC ceramics at low temper-

atures consists of a random distribution of silicon, oxygen, and carbon atoms. Nevertheless, if the concentration of carbon is large enough, heat-treatment at 1200 °C or above leads to a phase separation of the amorphous network into silica, carbon, and silicon carbide. However, due to the heterogeneous microstructure of the ion irradiated specimens, phase separation is not expected within the irradiated films and chemical reaction would be the only path toward the synthesis of silicon carbide.

2.4.4 Silicon

The synthesis of silicon within SiOC has been reported previously. For materials rich in silicon, i.e., those located within the SiO_2-Si-SiC triangle in Fig 2.2, it is possible to synthesize silicon nanoparticles. The formation of Si/SiO_2 composites has also been reported [67]. It has been shown that compared to other techniques such as sputtering, sol-gel derived ceramics contain silicon nanocrystals with a narrow distribution of particle size [15]. Considering the well-known size dependence of the properties of silicon quantum dots, sol-gel synthesis of SiO_2/Si composites has the advantage of controlled particle size over other techniques.

2.4.5 Microstructural configuration of polymer-derived ceramics

There are two major competing structural models for heat-treated SiOC ceramics. As the heterogeneity of SiOC ceramics occurs at the nanometric and even molecular level, direct observation of the structural configuration of SiOC ceramics is challenging. However, based on indirect techniques and the properties of the SiOC ceramics two models have been proposed for their microstructural configuration. Both of the models are for SiOC materials containing amorphous silica and free carbon nanodomains. One model involves carbon clusters within an amorphous silica matrix and the other model is an interconnected carbon network with silica domains filling the empty spaces. The two models are presented in Fig. 2.8. The first model is based upon the thermodynamic stability of SiOC materials and their resistance to crystallization, creep resistance, and small-angle x-ray scattering (SAXS) results [29, 31]. The small angle x-ray scattering results suggested that the microstructure of the SiOC specimens consisted of 1-5 nm nanodomains. Based on the small size of the domains and the creep and crystallization behavior, it was suggested that the microstructure of the SiOC materials is an interconnected network of carbon with silica filling the voids. This model is successful in explaining the resistance to both crystallization and creep, because the carbon network acts as a barrier for the diffusion of silicon and oxygen atoms and thus suppresses any creep or crystallization

and leads to thermodynamic stability [29, 31].

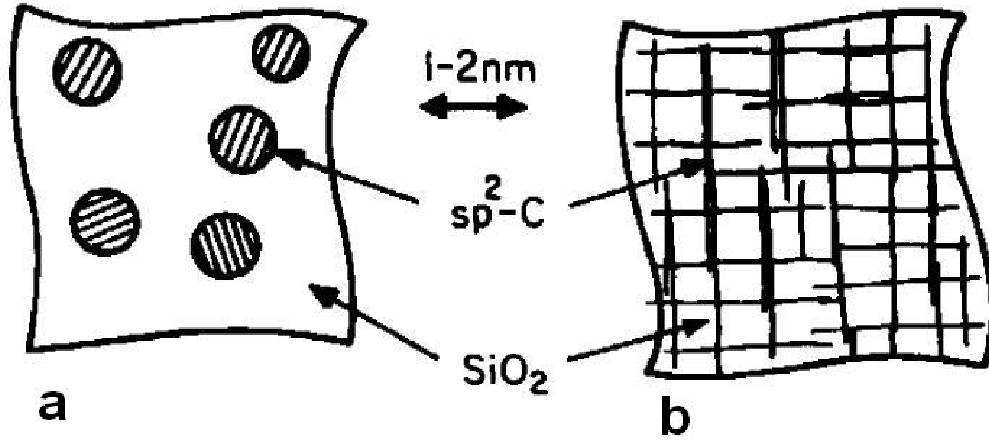

Figure 2.8: Two proposed microstructural configurations for polymer-derived SiOC materials a) isolated carbon clusters within an amorphous silica matrix and b) an interconnected carbon network with silica filling the voids [29].

The second model is based upon two-dimensional correlation NMR spectroscopy and NMR spin-lattice relaxation results [68, 69]. An example of two-dimensional correlation NMR spectroscopy results for SiOC ceramics is shown in Fig. 2.9. Four lines in the X and Y directions indicate the NMR peaks from four different tetrahedra. The figure shows the concentration of different tetrahedra along the diagonal. It also shows the prevalence of cross-peaks (number of connections between different tetrahedra), indicated by a blue symbol at the intersection of their peak lines. A variety of cross-peaks that correspond to connections between different SiO_xC_y tetrahedra were observed. The cross peaks between SiO_4-SiO_3C and SiO_4-SiO_2C_2 indicate connectivity between these tetrahedra units through Si-O-Si linkages. There is no cross-peak between SiC_4 and SiO_4. The cross-peak between SiC_4 and SiO_3C indicates that free carbon is connected to the SiO_2 network through SiO_xC_y tetraherdas. In addition, NMR spin-lattice relaxation studies of the spatial distribution of the tetrahedra units suggests an inhomogeneous distribution of these units and their porous nature. Based on NMR spin-lattice relaxation results and two-dimensional correlation NMR spectroscopy results, it appears that an interconnected network of graphene seems unlikely. Instead a porous structure of amorphous silica with individual carbon islands filling the porosities, described as "Swiss cheese" structure, is more plausible [68, 69]. According to this model, the carbon clusters are connected to the silica matrix through SiO_xC_y tetrahedra.

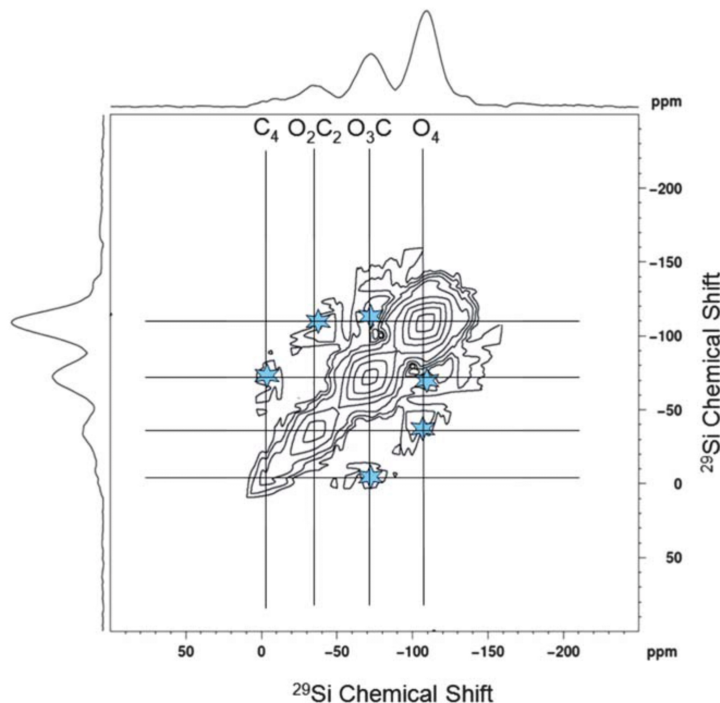

Figure 2.9: Contour plot of the ^{29}Si two-dimensional correlation NMR spectrum of a polysiloxane-derived SiOC PDC of composition $SiO_{1.5}C_{0.68}$ pyrolyzed at 1100 °C [69].

2.5 Possible effects of irradiation on polymer-derived ceramics

2.5.1 Crystallization

As previously mentioned, SiOC ceramics are resistant to crystallization and depending on the chemical composition and the processing method, crystallization may not occur even at temperatures as high as 1800 °C [70]. However, ion irradiation may alter this. The resistance to crystallization has been attributed to either the microstructural configuration of SiOC ceramics [29] or mixed bond tetrahedra (SiO_4, SiO_3C, SiO_2C_2, $SiOC_3$, SiC_4) at the interface of the amorphous carbon and silica [69]. The possible effect of microstructural configuration on crystallization is related to the difficulty of silicon and oxygen atoms to diffuse through a carbon network. On the other hand, the presence of mixed bonds at the interfaces, as observed by NMR spectroscopy [68, 69, 71], also explains the resistance to crystallization. These mixed bonds are present in every SiOC material. Due to the difference in the length of Si-O and Si-C bonds, organizing the two bonds in a periodic crystalline structure is thermodynamically and kinetically difficult [68, 69, 71]. However, ion irradia-

tion might alter the resistance to crystallization. Generally, induced damage during ion irradiation leads to amorphization, but it also aids in crystallization if it is accompanied by a subsequent heat-treatment. The disorder caused by irradiation plays a vital role in recrystallization. Bond disorder in amorphous materials leads to higher diffusion rates and it also increases the structural flexibility (the level of broken bonds, vacancies and lattic disorder) [72]. Irradiation induced crystallization has been reported for amorphous silicon [72] and silicon carbide [73]. In addition to temperature activated crystallization, athermal crystallization, due to electronic excitation during ion irradiation, is also possible [74]. Ion irradiated SiOC ceramics may have a structure that is different from heat-treated ceramics and so may be prone to crystallization. Induced bond disorder during ion irradiation may create thermodynamical drive for the crystallization process as well.

The resistance of sputtering derived SiOC ceramics to irradiation-induced crystallization was studied and it was found that even after elevated temperature ion irradiation, no sign of crystalline phases was observed by TEM or XRD [75–77]. It should be noted that these SiOC films were derived from sputtering and the behavior of sol-gel derived films might be different.

2.5.2 Synthesis of silicon carbide nanoparticles

Ion beam synthesis of silicon carbide nanoparticles is a common process. Many studies have focused on the synthesis of silicon carbide in a SiO_2 matrix by carbon ion implantation [78], silicon carbide in silicon by carbon ion implantation [79], and silicon carbide in diamond by silicon ion implantation [80, 81]. But ion implantation may not be the best approach for the synthesis of nanoparticles in hybrid films, because it leads to an incomplete decomposition of the starting films [21]. In addition, both silicon and carbon are already present in the films and there is no need to implant additional atoms.

Ion irradiation has been performed on sol-gel derived thin films to synthesize silicon carbide nanoparticles [25, 82]. But the studies were performed on carbon rich polymers like hydridopolycarbosilane (HPCS) [25] and polycarbosilane (PCS) [82] that decompose to silicon carbide after thermal decomposition. In addition, the presence of silicon carbide in carbon doped SiO_2 films after irradiation with swift heavy ions has also been observed [83, 84]. The synthesis of silicon carbide in TEOS/MTES derived films tends to be more challenging, because TEOS/MTES derived films usually contain lower levels of carbon and weaker silicon carbon bonds compared to HPCS and PCS, as evident from complete carbon loss in TEOS/MTES derived ceramics after heat-treatment. The final product of the thermal decomposition of TEOS and MTES is only silica with no residual carbon. Also, conventional ion irradiation, in contrast to swift heavy ion irradiation, deposits smaller

amounts of energy and may not lead to synthesis of silicon carbide particles.

2.6 Possible substrate-film reactions during heat-treatment

It has been previously reported that elevated temperature (≥1200 °C) heat-treatment of sol-gel derived SiOC thin films on silicon substrates leads to the formation of voids in the films and large surface defects [85]. This has been attributed to the reaction of silicon with the films. An example of such defects is shown in Fig. 2.10. As a result, elevated temperature heat-treatment should be performed on films coated on substrates other than silicon. Fused silica substrates are an ideal material, because their structure is similar to those of sol-gel derived thin films and no chemical reaction between the silica substrate and the films is expected.

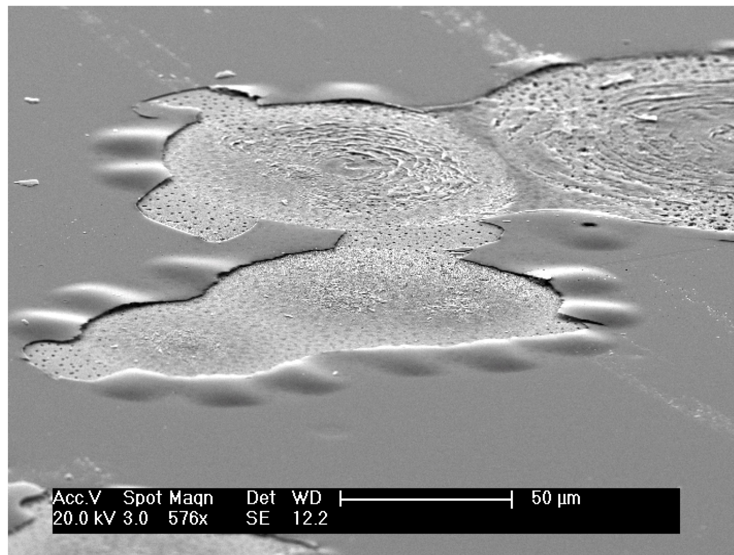

Figure 2.10: Formation of large surface defects in sol-gel derived SiOC thin films on a silicon substrate after heat-treatment at 1200 °C [85].

2.7 Summary of previous studies on ion irradiation of sol-gel derived thin films

This section summarizes the previous studies on the same subject that has been performed at Oklahoma State University. The first study on ion irradiation of sol-gel derived thin films was that by Ghisleni [21]. The work explored ion irradiation conditions where the ion range was both larger and smaller than the film thickness. Results indicated that, as expected, hardness was not

uniform throughout the film thickness in the partially converted films. The work on fully converted films focused on irradiation with 125 keV H^+ and 200 keV N^{2+} ions. The hardness and elastic modulus values obtained were noticeably higher than for heat-treated films. Possible explanations for the increase in hardness, including the development of amorphous silica network and formation of carbon clusters were proposed. The possible effect of the development of an amorphous silica structure was investigated by performing an additional heat-treatment after ion irradiation which led to further decomposition of the starting organic materials and a 30% decrease in film thickness. However, the hardness of a film irradiated with 125 keV H^+ at a fluence of 5×10^{16} decreased from 3.4 GPa to 0.8 GPa after heat-treatment at 800°C. This seems to indicate that the mere development of silica network as the dominant hardening mechanism is unlikely.

In addition, the possible effect of free carbon clusters as the microstructural feature responsible for the observed increase in the hardness, as suggested previously by others [82,86] was also examined. In order to study the effect of free carbon clusters on the mechanical properties of the irradiated films, ion irradiation was performed on films pre-heat-treated at 300°C and 800°C. The film that was heat-treated at 800°C had minimal carbon content. However, both films exhibited the same hardness values after ion irradiation, suggesting that the effect of free carbon clusters on the final hardness of the films was negligible for the films irradiated with N^{2+} ions. A summary of the hardness results is presented in Fig. 2.11 The study was inconclusive on the origin of the hardness increase after ion irradiation.

In another study performed at Oklahoma State University, Prenzel [87] focused on two sets of sol-gel derived films, acid- and base-catalyzed films converted by both ion irradiation and heat-treatment. The results indicated that even though the hardness values of heat-treated base-catalyzed films were higher than heat-treated acid-catalyzed films, ion irradiation led to higher hardness in acid-catalyzed films. The study mainly focused on base-catalyzed films and specifically, the sodium containing phases that were formed. However, some preliminary studies on the ion irradiated acid-catalyzed films were performed as well.

As a result of these studies, the current study focused on investigating ion irradiation of acid-catalyzed films, which previously had resulted in higher hardness. The ion irradiation conditions were designed such that the entire thickness of the films would be subjected to ion irradiation. Ion irradiation experiments were performed using H^+ and N^{2+} ions , but with higher energies. Additional ion irradiation experiments with heavier and higher energy Cu^+, Cu^{2+}, and Cu^{3+} ions were also performed on the films.

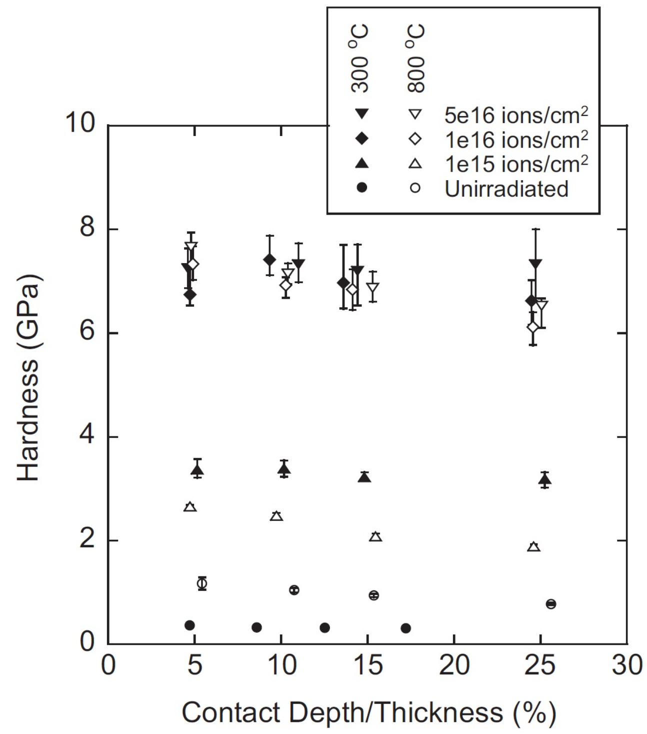

Figure 2.11: Effect of 250 keV N^{2+} ion irradiation on the hardness of sol-gel films pre-heat-treated at 300°C and 800°C. The full symbols represent the specimens preheated at 300°C and the empty symbols represent the specimens pre-heat-treated at 800°C [21].

Chapter 3

EXPERIMENTAL APPROACH

3.1 Thin film synthesis, deposition, and heat-treatment

Sol-gel derived TEOS/MTES films were prepared using either sodium hydroxide or acetic acid as a catalyst. The chemical composition of the prepared sols is presented in Table 3.1. The synthesis was performed at the Stiftung Institut für Werkstofftechnik (IWT) in Bremen, Germany.

Table 3.1: The chemical composition of acid- and base-catalyzed sols.

	TEOS (mol)	MTES (mol)	CH_3COOH (mol)	NaOH (mol)	H_2O (mol)	PVP (mol)	C_2H_5OH (mol)
Acid-Catalyzed	0.4	0.6	1	—	1	0.25	7.5
Base-Catalyzed	0.4	0.6	—	0.96	5.66	—	1

For the synthesis of acid-catalyzed sols, ethanol, distilled water and acetic acid were stirred in a beaker. While the solution was stirred, TEOS and MTES were added. In the next step, PVP was added drop by drop to the solution and the beaker was covered to prevent the evaporation of ethanol. The temperature of the mixture was raised to 50 °C and was kept constant for 30 min. The sol was stored for one day at room temperature in an argon atmosphere before deposition. A schematic of the process is presented in Fig 3.1(a) [87].

The base-catalyzed sols were prepared by dissolving NaOH in a mixture of TEOS and MTES. The solution was kept for 24 h under an argon atmosphere in a three-neck round bottom flask. Then

a mixture of water and ethanol was added drop by drop to the solution. The temperature of the mixture was kept constant at 35 °C. A schematic of the process is shown in Fig 3.1(b). Similar to the acid-catalyzed sol, the base-catalyzed sol was stored in an argon atmosphere at room temperature for one day before deposition.

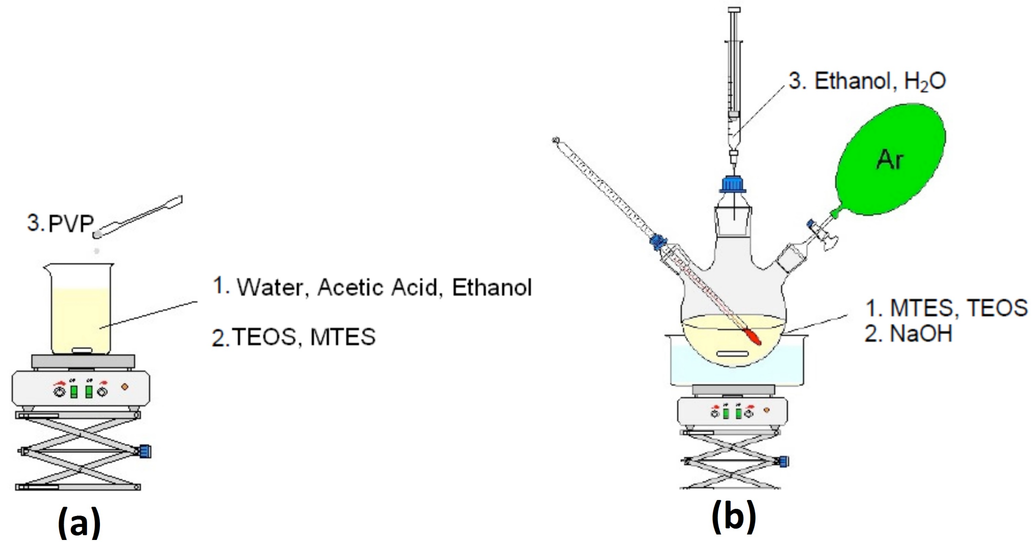

Figure 3.1: Preparation of a) acid-catalyzed sols and b) base-catalyzed sols. The numbers indicate the sequence of addition [87].

The prepared sol was coated onto polished (100) silicon wafers using spin coating. After deposition, the wafers were dried at 80 °C for 10 min. The acid- and base-catalyzed films were heat-treated in air at 300 °C for 30 min. After the initial heat-treatment, the films were either heat-treated at temperatures ranging from 500 °C to 800 °C in air for 30 min or were ion irradiated to decompose the organic compounds.

The thickness of the films was measured by step height method using atomic force microscopy (AFM). It was found that the thickness of the films before ion irradiation was about 1 μm ($\pm$0.1 μm). The thickness of the films after ion irradiation varied and is reported in the next chapter. The weight gain after coating, the film thickness, and the film dimensions were used to estimate the density of the green films. It was found to be approximately 1.0 g/cm^3 for both green acid- and base-catalyzed films.

Previous studies on ion irradiated acid- and base-catalyzed films indicated the higher hardness of the acid-catalyzed films [87]. Therefore, this study was focused on acid-catalyzed films. Unless otherwise specified, all the films in this study are acid-catalyzed films.

3.2 Ion irradiation

Ion irradiation is an alternative method of providing the required energy for decomposition of the polymers. Ion irradiation involves an energetic ion traversing a solid and the subsequent collisions of the ions with the atoms in the solid. The ion deflects from its initial trajectory after colliding with stationary target atoms. In addition, it may excite the electrons in the solid which leads to bond breaking and ionization. As a result of nuclear and electronic collisions, the energy of the ions decreases until they come to rest. The energy loss per distance traveled ($\frac{dE}{dx}$), known as the stopping power, or linear energy transfer, is expressed as the summation of the nuclear stopping power ($\frac{dE}{dx}\big|_n$) and electronic stopping power ($\frac{dE}{dx}\big|_e$):

$$\frac{dE}{dx} = \frac{dE}{dx}\bigg|_e + \frac{dE}{dx}\bigg|_n \tag{3.1}$$

Nuclear collisions usually involve larger energy transfer, causing lattice and bond disorder. Electronic stopping, on the other hand, transfers a smaller energy per collision and the resulting ion deflection is negligible. The contribution of each of the two stopping powers varies with atomic number (Z) and incident ion energy. In general, irradiation with ions with smaller atomic numbers and lower energies involves a larger portion of electronic collisions and irradiation with heavier ions and higher energies involves a larger portion of nuclear stopping.

It is also necessary to estimate the projected ion range, the distance traveled normal to the surface of the target. For this study, the projected ion ranges were calculated using the computer code SRIM (Stopping and Range of Ions in Matter) [88]. For all irradiation conditions, the projected ion range was larger than the film thickness. Electronic and nuclear stopping powers were also calculated using SRIM.

The ion irradiation experiments were carried out at Los Alamos National Laboratory. Individual coated silicon substrates were cleaved into quadrants. Ion irradiation was performed using different ion species, including H^+, N^{2+}, Cu^+, Cu^{2+}, and Cu^{3+}. For the lower atomic number ions (H^+ and N^{2+}) the dominant energy loss mechanism was electronic stopping. The stopping power for Cu^+, Cu^{2+}, and Cu^{3+} irradiation was a combination of electronic and nuclear stopping. There is an increase in nulcear stopping and a decrease in electronic stopping along the ion range for all ion species. For heavy ions at the end of ion range, the nuclear stopping power becomes larger than electronic stopping. The irradiation was performed using 200 KeV H^+, 400 KeV N^{2+}, 1 MeV Cu^+, 4 MeV Cu^{2+}, and 9 MeV Cu^{3+}. A summary of ion irradiation conditions, including electronic and nuclear stopping powers at the surface, is presented in Table 3.2.

Table 3.2: Ion irradiation conditions of films for the acid-catalyzed films.

	H^+	N^{2+}	Cu^+	Cu^{2+}	Cu^{3+}
Energy (keV)	200	400	1000	4000	9000
Fluence ($\times 10^{15}$ ions/cm^2)	0.01-200	0.01-5	0.01-10	0.01-10	0.01-10
Nuclear stopping (eV/Å-Ion)	0	1.8	31	12.7	7
Electronic stopping (eV/Å-Ion)	7.5	43	50.3	133	250
Total stopping (eV/Å-Ion)	7.5	44.8	81.3	145.7	257
Projected ion range (μm)	2.35	1.16	1.2	3.88	6.39

A secondary heat-treatment was also performed on the ion irradiated films. The secondary heat-treatments were performed on the base-catalyzed films. The heat-treatment experiments were performed at 1100 °C and 1350 °C in an argon atmosphere. The list of conditions for the secondary heat-treatment experiments are listed in Table 3.3. In addition to the base-catalyzed films, a green acid-catalyzed film was also heat-treated at 1100 °C and 1350 °C.

Table 3.3: Ion irradiation and secondary heat-treatment conditions for the base-catalyzed films.

Ion species	Fluence ($\times 10^{15}$ ions/cm^2)	Heat-treatment condition
125 keV H^+	1	1100 °C, 2 hours
125 keV H^+	10	1100 °C, 2 hours
125 keV H^+	1	1350 °C, 2 hours
125 keV H^+	10	1350 °C, 2 hours
250 keV N^{2+}	1	1100 °C, 2 hours
250 keV N^{2+}	10	1100 °C, 2 hours
250 keV N^{2+}	1	1350 °C, 2 hours
250 keV N^{2+}	10	1350 °C, 2 hours

3.3 Characterization techniques

3.3.1 Raman spectroscopy

Raman spectroscopy is based upon the interaction of light with the vibrational energy levels of the material. When a material is exposed to ultraviolet or visible laser light, the inelastically scattered light is used to study the vibrational energy levels of materials. When a molecule absorbs an incident photon, it is excited to a virtual energy level higher than its ground state. Most of the light is scattered elastically (Rayleigh scattering), however there are two inelastic scattering processes as well. One is Stokes scattering in which the energy of the photon after scattering is less than its initial energy, with the energy decrease resultant from the formation of a phonon (unit of vibrational energy arising from the oscillation of atoms in a solid material). The other inelastic scattering process is anti-Stokes scattering where the energy of the photon after scattering is more than its initial energy. In anti-Stokes scattering, the energy increases as a result of the annihilation of a phonon. Figure 3.2 shows a schematic of the three different scattering mechanisms. In addition, Fig. 3.2 shows the infrared absorption mechanism that will be discussed in Section 3.3.2. Generally, Stokes scattering is the measured response in Raman spectroscopy. According to the Boltzmann distribution, lower energy levels are more populated at lower temperatures, so Stokes scattering is much stronger than anti-Stokes scattering. According to the Boltzmann distribution, the population of vibrational level j (N_j) can be calculated as:

$$N_j = N \times exp(-\frac{(j+0.5)h\nu}{k_b T}) \tag{3.2}$$

where j represents the vibrational level, N is the total number of molecules, h is Planck's constant, ν is the frequency, k_b is the Boltzmann constant, and T is the temperature. It is obvious that higher energy levels have lower populations.

Raman spectroscopy was performed using a confocal Raman microscope (WITec alpha300). A 532 nm (2.33 eV) frequency doubled Nd:YAG laser was used as the light source. Light was focused on the surface using a 100X/0.9NA Nikon objective and was collected using the same objective. The theoretical spot size of the set-up is 0.7 μm. The collected light was focused onto a UV-visible multimode optical fiber acting as the confocal pin-hole. The core diameter of the fiber was 100 μm. Light passing through the pinhole was then directed to a 0.3 m Acton monochromator which dispersed the light with either a 600 grating/mm or 1800 grating/mm diffraction grating. The dispersed light was then detected by a 1024×128 pixel charge-coupled device (CCD) from Andor

Technology. The photoluminescence spectroscopy experiments were performed using the same set-up, but with a 150 grating/mm grating. The reported Raman spectra were are average of five separate collections.

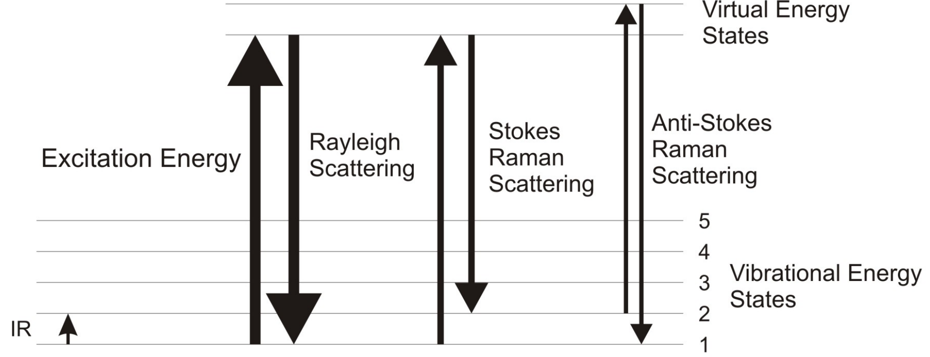

Figure 3.2: Schematic of different scattering mechanisms during Raman and FT-IR spectroscopy.

3.3.1.1 Curve fitting of the carbon D and G Raman modes

Raman spectroscopy was utilized in this study, in addition to other purposes, to evaluate the free carbon clusters formed during ion irradiation. The Raman spectra of most carbon materials consists of two main D and G Raman modes. In order to quantitatively compare different films, it is necessary to perform curve fitting on the D and G modes. For disordered carbon with broad peaks, a combination of two Gaussian peaks is suitable [35]. However, an alternative approach exits that uses a Breot-Wigner-Fano (BWF) lineshape [35,89,90]. The BWF lineshape is asymmetric which is suited for the theoretical shape of the G mode. The BWF lineshape is given by :

$$I\left(\omega\right) = \frac{I_0[1 + \frac{2(\omega-\omega_0)}{Q\Gamma}]^2}{1 + [\frac{2(\omega-\omega_0)}{\Gamma}]^2} \tag{3.3}$$

where I_0 is the peak intensity, Γ is the full width at half maximum (FWHM), ω is relative wavenumber, ω_0 is the spectral center, and Q^{-1} is the BWF coupling coefficient. The Lorentzian lineshape is the same as the BWF with Q^{-1}=0.

There are several reasons for using the BWF lineshape. Most importantly, the BWF lineshape accounts for residual Raman intensities at 1100 cm^{-1} and 1400 cm^{-1}, without adding extra peaks.

However, it accounts for a smaller D mode. The BWF lineshape is more suitable for the Raman response of larger, more ordered clusters and the Gaussian lineshape is better fitted for the Raman response of amorphous and smaller carbon clusters [35].

3.3.2 Fourier-transform infrared spectroscopy (FT-IR)

Infrared spectroscopy is the measurement of the absorption of infrared light as a function of frequency. The absorption is a result of the transition of the molecules from lower vibrational energy levels to higher vibrational energy levels. A schematic of the energy transition in infrared spectroscopy is shown Fig. 3.2. The difference between Raman spectroscopy and infrared spectroscopy can be summarized as that in Raman spectroscopy, the measured light has a different wavelength than the incident light, whereas in infrared spectroscopy, the variation of intensity for a specific wavelength is measured. The origin of the name is the utilization of the Fourier transformation to convert raw data to a spectrum.

Infrared experiments were performed using an Agilent 680 IR spectrometer in both reflection and transmission modes. The collection was performed in the 400-4000 cm^{-1} range with 4 cm^{-1} resolution. Sixteen individual collections were averaged to acquire each spectrum.

3.3.3 Rutherford backscattering spectrometry and elastic recoil detection

Rutherford backscattering spectrometry (RBS) is a quantitative analytical technique for analysis of composition and thickness of solid surfaces. In RBS, a mono-energetic ion beam, usually H^+ or He^+, is directed toward the surface and then the energies of the backscattered ions are detected. The energy loss of the backscattered ion depends on nuclear collisions as well as small-angle scattering from electronic collisions. The energy loss by nuclear collisions is a function of scattering cross-section, which itself is a function of atomic mass and atomic number of the target nucleus. Thus, two nuclei from two different elements scatter ions with different energies and angles, which is utilized to measure the chemical composition of a target surface.

RBS was performed in the Ion Beam Materials Laboratory at Los Alamos National Laboratory using a collimated beam of 3.8 MeV $^4He^+$ ions from a Pelletron tandem accelerator. The backscattered ions were detected at a scattering angle of 167° in the Cornell geometry. In the Cornell geometry, the incident beam, exit beam and sample rotation axis are in one plane.

Since in RBS, atoms with atomic numbers smaller than the projectile ions do not backscatter the ions, RBS is not capable of profiling lighter ions (i.e., hydrogen). In order to profile the hydrogen

concentration, it is necessary to perform elastic recoil detection (ERD). In ERD analysis, an energetic ion is directed toward the surface. The electronic and nuclear collisions lead to the recoil of the lighter ions which are then collected by a collector and analyzed. ERD experiments were performed in the Ion Beam Materials Laboratory at Los Alamos National Laboratory using a 2 MeV $^4He^+$ ion beam with incident angle of 75° in the IBM geometry. In the IBM geometry, the incident beam, exit beam, and surface normal are in one plane. The recoiled atoms were collected at a scattering angle of 30°.

It is also possible to use the RBS/ERD results to estimate the density of the films. First, the film thickness is measured by atomic force microscopy (AFM). Rutherford backscattering spectrometry (RBS) and elastic recoil detection (ERD) data are then used to determine the density. In the process of analyzing the chemical composition, the total number of specific atoms per unit area of the films is calculated. Knowing the thickness measured by AFM, the density of the films can then be calculated.

3.3.4 X-ray diffraction

X-Ray diffraction was utilized to study the formation of possible crystalline phases within the films. In order to perform XRD on thin films, it is necessary to utilize glancing-angle X-ray diffraction (GAXRD). This technique involves exposing the film to highly monochromatic X-ray beams at a fixed, small angle and then moving the collector position to capture the XRD pattern of the films. The small fixed angle helps to eliminate the contribution from the substrate. The XRD experiments were performed using a Cu-Kα X-ray source (1.54 Å) with a Bruker AXS D8 Discover diffractometer in the 2θ range of 10-60° with a glancing angle of 7.5°.

3.3.5 Scanning electron microscopy

Scanning Electron Microscopy (SEM) was utilized to investigate the surface structure of the thin films. SEM was performed using a field emission scanning electron microscope.

3.3.6 X-ray photoelectron spectroscopy

The chemical composition of the films, as well as the distribution of the SiO_xC_y tetrahedra were evaluated using XPS. The experiments were performed at Tascon GmbH in Germany using a PHI Quantera SXM scanning XPS microprobe Model 40-800. During the XPS experiments, first the whole spectra was collected, followed by measurement of single XPS lines for electrons coming

from C 1s, O 1s and Si 2p. The experiments were performed using Al-kα (1486.6 eV) as the X-ray source. No ion etching was performed prior to the experiments to avoid the modification of the films. Charging correction was achieved automatically by controlled electron irradiation. The analysis of the peaks were performed by Shirley background subtraction [91] and fitting the peaks using a 70% Gaussian-30% Lorentzian lineshape.

Chapter 4

RESULTS AND DISCUSSION

4.1 Surface condition of the ion irradiated and heat-treated films

The surfaces of the films after synthesis exhibit minimum roughness and are crack-free, as determined by optical microscopy. AFM characterization reveals that in a 1 μm$\times$1 μm area, the surface roughness, Rq, is less than 3 nm ranging from 1.1 nm for the film heat-treated at 300 °C to 2.6 nm for the film heat-treated at 800 °C. The surface roughness is unchanged by ion irradiation. Figure 4.1 shows SEM images from the green film, the film heat-treated at 800 °C, and a N^{2+} irradiated film with a fluence of 10^{15} ions/cm^2. SEM imaging is performed close to the scratches that are intentionally created to measure the film thickness. The surface of all films are free of any defects or any topographical features, e.g., porosity or secondary phases, and possessed minimum roughness.

4.2 Conversion of films with light ions

4.2.1 Chemical evolution of the films after heat-treatment and ion irradiation with light ions

Figure 4.2 shows the atomic concentration ratios of hydrogen, carbon, and oxygen compared to silicon for H^+ and N^{2+} irradiated thin films, as obtained by RBS/ERD analysis. The chemical composition of the film irradiated with H^+ ions with a fluence of 2×10^{17} ions/cm^2 is not measured. The films irradiated with H^+ ions exhibit a monotonic decrease in hydrogen content with increasing fluence. N^{2+} irradiated films also exhibit a decrease in hydrogen concentration with increasing

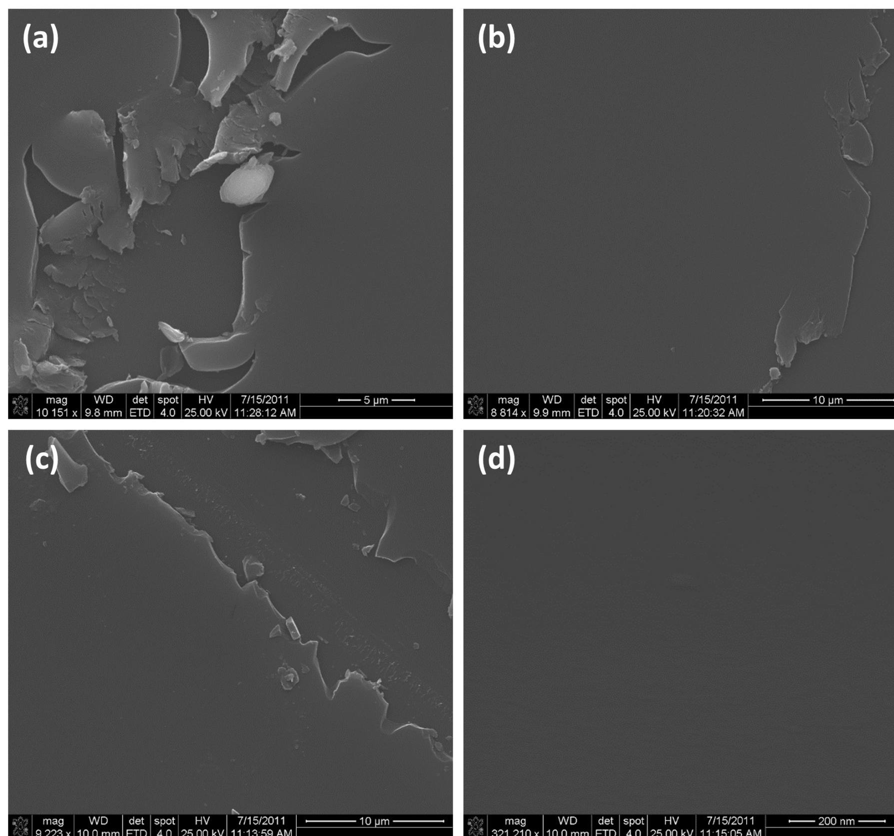

Figure 4.1: SEM images from sol-gel thin films, a) green film b) heat-treated at 800 °C c) ion irradiated with N^{2+} ions with a fluence of 10^{15} ions/cm^2 and d) irradiated with N^{2+} ions with a fluence of 10^{15} ions/cm^2 at 320,000X.

fluence. Hydrogen loss during the ion irradiation of polymers is expected and has been previously studied [82, 92]. It is reported that although most of the hydrogen is released as H_2 during ion irradiation, a small fraction of hydrogen may leave the irradiation target as CH_4 [93]. In addition, some fluctuations in oxygen content is expected due to the absorption of oxygen from the air by free radicals formed during ion irradiation [93, 94]. As a result, variations in the oxygen and carbon concentration of the films is expected. However, the changes in the oxygen and carbon concentration of the films after irradiation with H^+ and N^{2+} ions do not follow any trend.

Figure 4.3 shows the atomic concentration ratios of carbon and oxygen compared to silicon for the heat-treated films. There is a decrease in the carbon content of the films with increasing temperature, while the oxygen concentration is relatively constant. This is in agreement with previous reports on the thermal decomposition of TEOS/MTES sol-gels [17, 95]. The final product of the heat-treated TEOS/MTES derived film is amorphous silica.

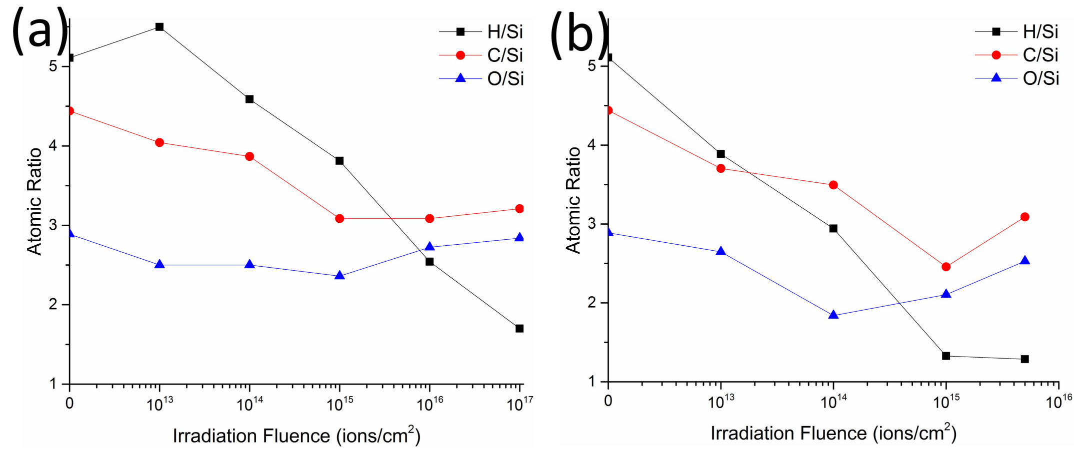

Figure 4.2: Atomic concentration ratios of hydrogen, carbon, and oxygen compared to silicon for films irradiated with a) H^+ and b) N^{2+} ions.

4.2.1.1 Changes in the density of the films after ion irradiation

Figure 4.4 shows the ERD/RBS estimated density of the films as a function of fluence for both sets of ion irradiated films. The density of the film irradiated with H^+ with a fluence of 2×10^{17} ions/cm^2 is not measured. There is an increase in density with increasing ion irradiation fluence. The increase in density follows the same general trend as the hydrogen loss (Fig. 4.2) for both H^+ and N^{2+}irradiated films and is more pronounced in the N^{2+} irradiated films. The increase in density after irradiation has also been observed in other sol-gel derived ceramic films [96,97] and is related to ion-matter interactions (electronic and nuclear stopping). The increase in density is accomplished by condensation/cross linking reactions, structural modification, and bond breaking [96]. The increase in density is related both to film shrinkage as a result of decomposition of the starting materials, as well as changes in the structure of constituent final phases, as will be discussed later in the text.

4.2.1.2 XRD characterization of possible crystalline phases within the ion irradiated films

Figure 4.5 shows the XRD patterns of the H^+ and N^{2+} irradiated thin films. The XRD pattern of all films after ion irradiation exhibit no crystalline peaks. The only observable feature in the XRD patterns is a broad peak centered around 25°, attributed to amorphous silica [98, 99]. The small peak at 47° may have originated from the (220) peak of the silicon substrate (JCPDS Number: 27-1402). The origin of the peak at 44.8° is not clear.

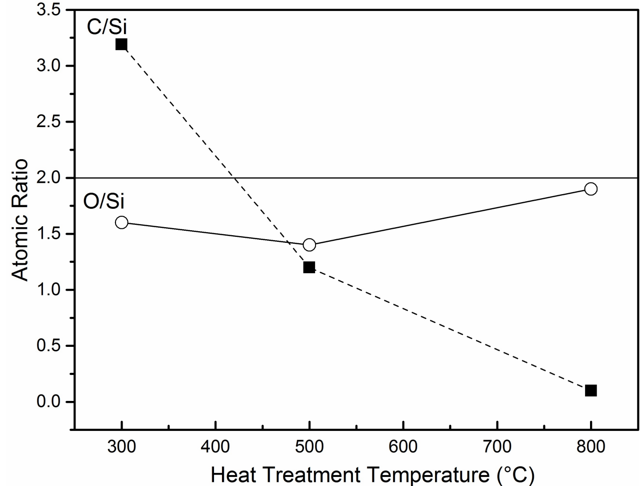

Figure 4.3: Atomic concentration ratios of carbon, and oxygen compared to silicon for heat-treated thin films [87]. The horizontal line is the theoretical composition of SiO_2.

4.2.2 FT-IR spectroscopy characterization

4.2.2.1 Decomposition of the starting organic materials

In order to study the decomposition of the starting materials during ion irradiation, FT-IR spectroscopy was performed on the films in the transmission mode. For transmission experiments, the background signal was first collected with a bare silicon substrate in place to remove the effect of the substrate, as described previously [100]. The results are presented in Figs. 4.6, 4.7, and 4.8 for the heat-treated, H^+ irradiated and N^{2+} irradiated films, respectively.

The peaks observed around 750-800 cm^{-1} are either related to the Si-C stretching or SiC-CH_3 rocking mode [101]. However, since no Si-C bond is present in the green film, yet this peak is still present in its FT-IR spectra, it is concluded that these peaks are related to the SiC-CH_3 rocking mode. Different peaks located between 900 to 1300 cm^{-1} are related to the amorphous silica network and will be discussed further. The peak at 1275 cm^{-1} is related to C-H bond in Si-CH_3 and again is an indication of the presence of the starting organic materials. The peak at 1450 cm^{-1} originates from the C-H in-plane bending mode [102] and is from the starting acetic acid. The peak around 1670 cm^{-1} is due to OH vibrations [103] from adsorbed or entrapped water. The peaks between 2850-3000 cm^{-1} are from C-H_x (x=1, 2, 3) [100,104] and are again related to the starting materials. The intensity of all these peaks, except for the silica related peaks, decreases with increasing heat-treatment temperature or irradiation fluence. As expected, the decrease in the intensity of the mentioned peaks is consistent with the hydrogen concentration in the irradiated films (Fig. 4.2).

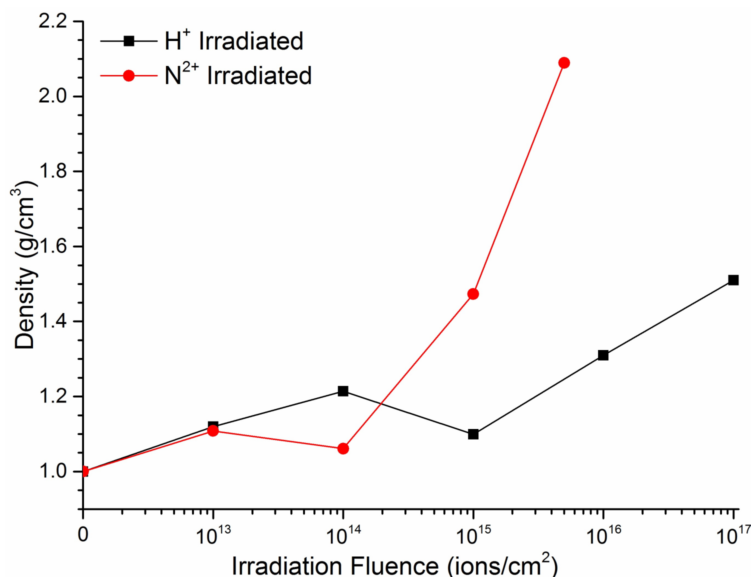

Figure 4.4: Variations in the density of H^+ and N^{2+} irradiated films as a function of fluence.

The peaks around 2300 cm^{-1} are related to C=O bond from carbon dioxide in air and insufficient background subtraction and are not related to the films.

The FT-IR results are consistent with both Figs. 4.2 and 4.4, where a gradual hydrogen loss and increase in density is observed. The decrease in the intensity of the FT-IR peaks of the starting materials follows the same trend as hydrogen loss and densification. The results indicates the success of ion irradiation in the decomposition of the starting organic materials.

4.2.2.2 Development of an amorphous silica network

The FT-IR peaks located between 900 to 1300 cm^{-1} are related to Si-O-Si bonds. In order to study the Si-O-Si peaks, reflection FT-IR spectroscopy was performed to eliminate any possible effect from the substrate or film/substrate interaction (e.g., possible oxidation of the silicon substrate before or during ion irradiation or heat-treatment). The results for the reflection FT-IR spectroscopy in the range of 600-1450 cm^{-1} are presented in Fig. 4.9. The presence of Si-O-Si peaks in all films indicates that an amorphous silica network is present in all of the irradiated and heat-treated films. However, the structure of the amorphous network varies between the different films. In addition to the Si-O-Si FT-IR peaks, an additional peak around 1275 cm^{-1} is also visible in Fig. 4.9 that is related to a Si-CH_3 rocking mode and is an indicator of the presence of the starting precursor materials.

There are three main FT-IR peaks present between 900 to 1300 cm^{-1}. The strongest peak,

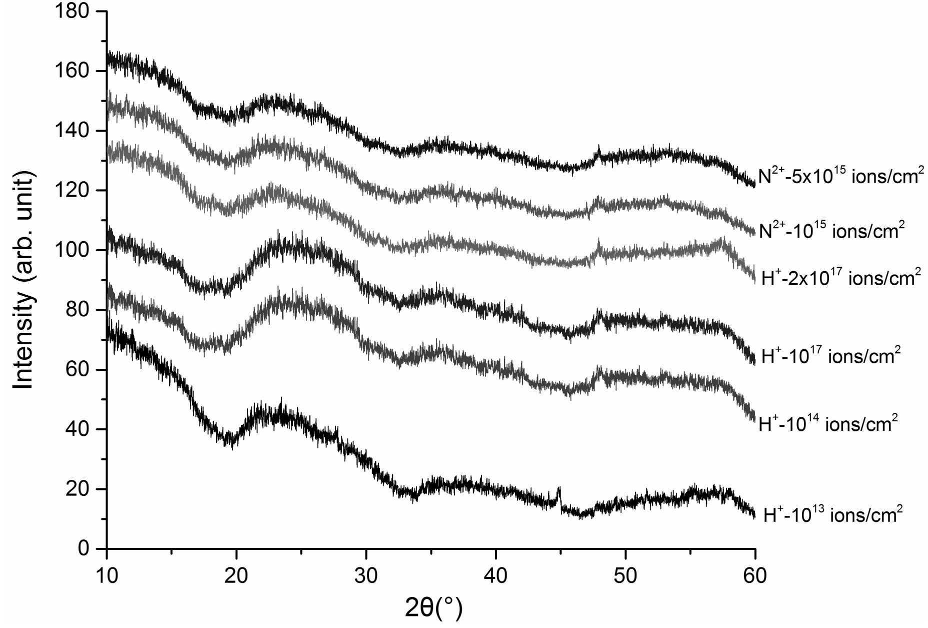

Figure 4.5: XRD patterns of H^+ and N^{2+} irradiatied thin films.

originating from the Si-O-Si bond, is the TO peak. For fused silica, it is located around 1080 cm^{-1}. The FT-IR peak around 1200 cm^{-1} is the longitudinal optical (LO) peak, which, in sol-gel derived silica-based films, is considered an indication of porosity [105–107]. In addition to the two main peaks, the introduction of carbon into the silica network and the formation of O-Si-C bonds gives rise to an additional peak around 1140 cm^{-1} [108, 109]. The incorporation of carbon into the silica network has another effect, a shift in the spectral center of the TO peak to lower wavenumbers. This phenomenon is explained by a bonding structure model and differences in electronegativity of carbon and silicon [110]. In the absence of any carbon atom, the Si-O-Si bond angle of amorphous silica varies between 120-180° with an average of 144° [111]. When carbon replaces one of the oxygen atoms in the SiO_4 tetrahedra, the difference between the electronegativity of carbon (2.5) and oxygen (3.5) causes a distortion in bond angles as a result of distortion of electron clouds and electrostatic forces. Carbon has a lower electronegativity than oxygen, so the electrons in the Si-C bonds are located closer to the silicon atoms, compared to the electrons in the Si-O bonds. The result of this uneven electron positioning in SiO_xC_y tetrahedra is an increase in the bond angle of O-Si-C and a decrease in the Si-O-Si bond angle. The decrease in the bond angle, in return, leads to a decrease in the spectral center of the TO peak.

Carbon incorporation is not the only factor that changes the Si-O-Si bond angle. Other factors like bond scission [53], destruction of the SiO_4 tetrahedra six fold rings [52], residual compressive

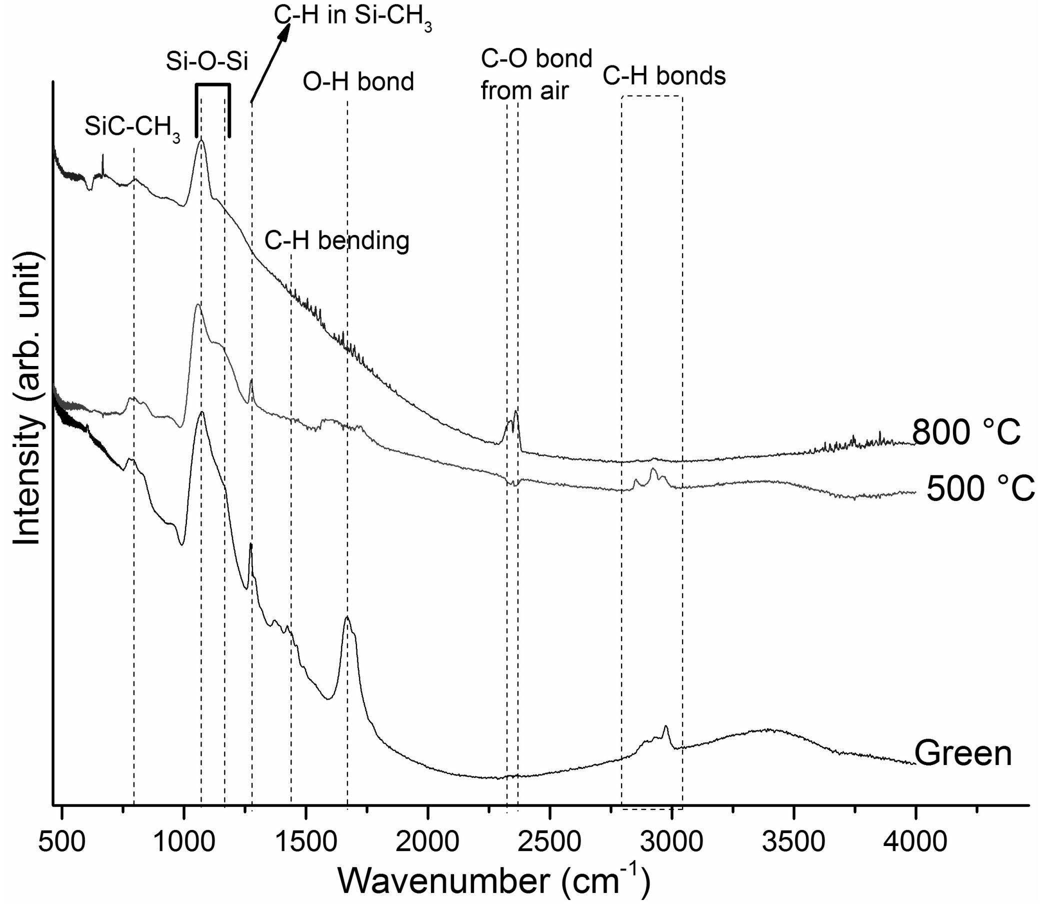

Figure 4.6: Transmission FT-IR spectra of heat-treated thin films.

stress [112], and thickness [113] also change the spectral center of the TO peak, because they all affect the bond angle of the Si-O-Si bond. Ion irradiation also affects the Si-O-Si bond angle [52,114–116]. The reason for the decrease in the Si-O-Si bond angle after ion irradiation is related to the combined effects of thermal spikes, defined as the local melting and fast quenching of formed localized melt during ion irradiation, and induced defects (vacancies and interstitial atoms) during ion irradiation [114–117]. Thermal spikes cause local melting and a subsequent quenching that yields a more compact structure (i.e., smaller bond angle) [116]. In addition, induced point defects during ion irradiation and a subsequent structural relaxation (re-orientation and re-bonding of tetrahedra [114, 115, 117]) also leads to a decrease in the Si-O-Si bond angle [114, 115]. The combination of thermal spikes, structural relaxation, and carbon incorporation leads to a silica structure with smaller bond angle. It should be noted that both experimental results [116] and molecular dynamics simulations [114, 115] indicated that the structure of silica compacted by ion irradiation is similar to the structure of silica compacted by applying pressure. In addition, it has been shown that the

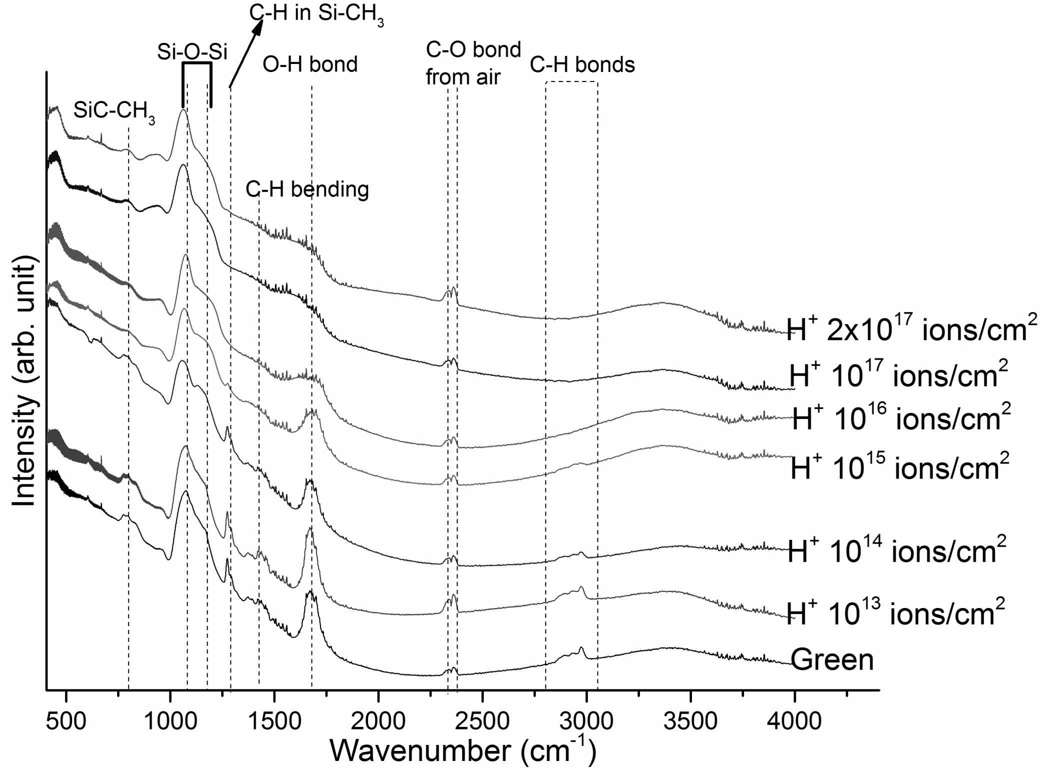

Figure 4.7: Transmission FT-IR spectra of the H^+ irradiated thin films.

vibrational states of silica after compaction with ion irradiation is similar to the vibrational states of silica after compaction with applied pressure [114].

In order to study the evolution of the FT-IR peaks, curve fitting was performed using three Lorentzian peaks for the Si-O-Si TO peak, Si-O-Si LO peak, and O-Si-C peak on the reflection FT-IR spectra. The results of the curve fitting are presented in Table 4.1. The green film exhibit two distinct TO and LO peaks, which is expected due to the porosity of the green film. The spectral center of the TO peak for the green films is 1083 cm^{-1}, corresponding to a Si-O-Si bond angle of 145°. The bond angle can be estimated from Equations 2.1 and 2.2, as described in Section 2.4.2. Since no bond scission or induced defects are expected after heat-treatment, the decrease in the TO peak spectral center to 1051 cm^{-1} after heat-treatment at 500 °C is solely related to the incorporation of carbon within the silica network. The O-Si-C peak is also observed after heat-treatment at 500 °C. After heat-treatment at 800 °C, most of the carbon within the films is removed. This is inferred by the absence of the O-Si-C peak and the return of the TO peak spectral center to higher wavenumbers (1080 cm^{-1} and corresponding bond angle of 144°). The intensity of the LO peak decreases after heat-treatment at 800 °C, because sintering of the amorphous silica at 800 °C leads to an increase in density.

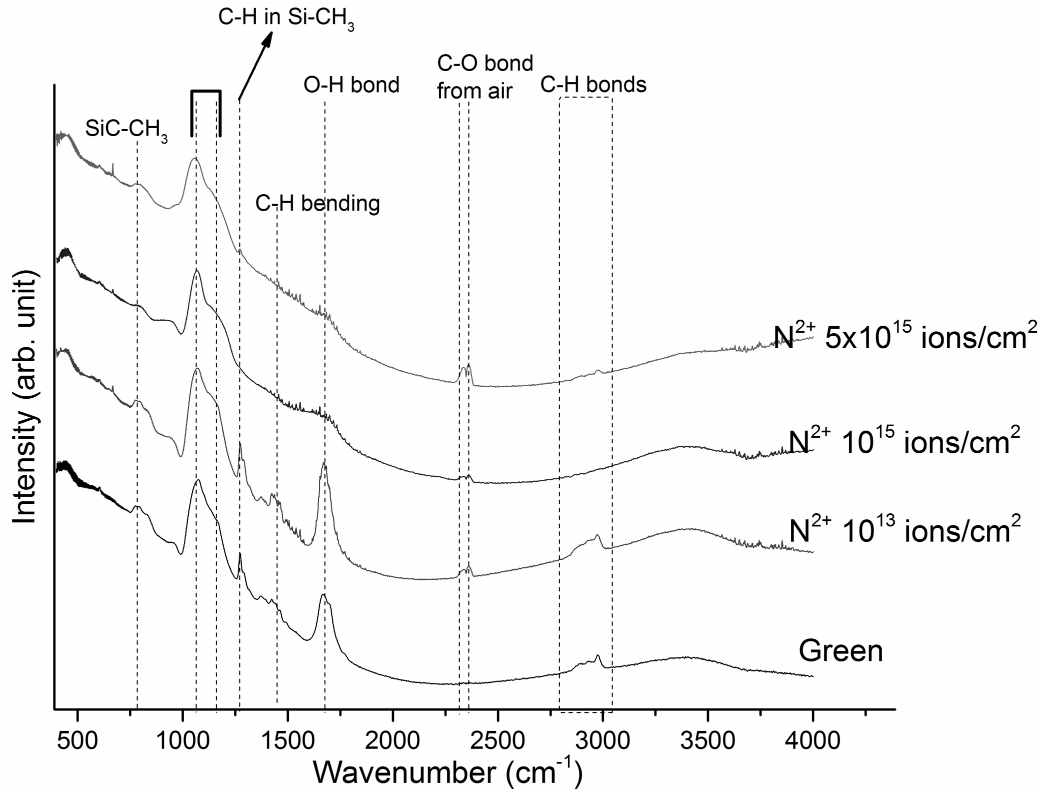

Figure 4.8: Transmission FT-IR spectra of the N^{2+} irradiated thin films.

The FT-IR spectra of H^+ irradiated films at lower fluences (10^{13}, 10^{14} and 10^{15} ions/cm^2) are similar to the green film. This is in agreement with the results shown in Fig. 4.2 where no major differences between the chemical composition of the green films and the films irradiated at lower fluences are observed. The O-Si-C peak is only observed after irradiation with a fluence of 10^{16} ions/cm^2. After irradiation with H^+ ions at 10^{16} ions/cm^2, the TO peak spectral center is still close to that of the green film and there is a decrease in the intensity of LO peak as a result of a reduction in porosity. The films irradiated at the highest fluence (2×10^{17} ions/cm^2) have a TO peak spectral center of 1064 cm^{-1} (bond angle of 139°) and a higher O-Si-C peak intensity which is an indication of the incorporation of carbon within the silica network, as well as irradiation-induced decrease in the bond angle. The decrease in the LO peak intensity after irradiation with H^+ ions with a fluence of 10^{16} ions/cm^2 or higher follows the same trend as density (Fig. 4.4).

The spectra for the N^{2+} irradiated films with a fluence of 10^{13} ions/cm^2 are similar to the green film. However, after irradiation with a fluence of 10^{15} ions/cm^2, the O-Si-C peak is present, and there is a shift in the TO peak spectral center to lower wavenumbers which is again an indication of bond disorder and carbon incorporation within the silica network. After ion irradiation with

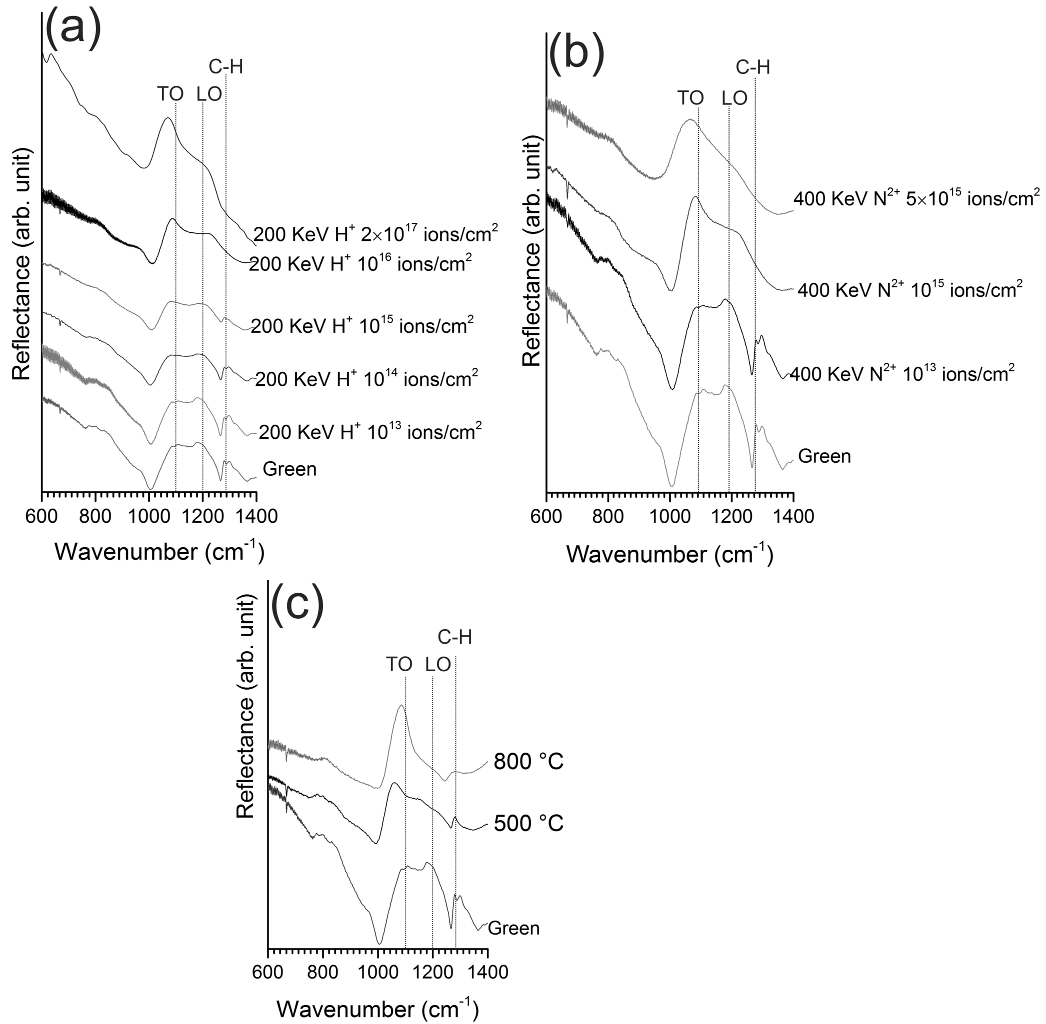

Figure 4.9: Reflection FT-IR spectra of the H^+ irradiated, N^{2+} irradiated, and heat-treated films.

N^{2+} ions with a fluence of $5{\times}10^{15}$ ions/cm^2, the position of the TO peak shifts to 1050 cm^{-1}, corresponding to a bond angle of 135°. There is a decrease in the intensity of the LO peak, related to a decrease in porosity which is consistent with results shown in Fig. 4.4. The intensity of the O-Si-C peak is the highest for this fluence.

The results indicate that with increasing ion irradiation fluence and ion energy, the incorporation of carbon within the silica structure is increased. In addition, the combined effect of thermal spikes and structural damage due to irradiation, and incorporation of carbon within the silica network, decreases the Si-O-Si bond angle and leads to a more compact silica network structure. In addition, a reduction of porosity in the films as a result of ion irradiation is confirmed by the FT-IR spectroscopy results. The increase in the density of the films (Fig. 4.4) should be attributed to both a decrease

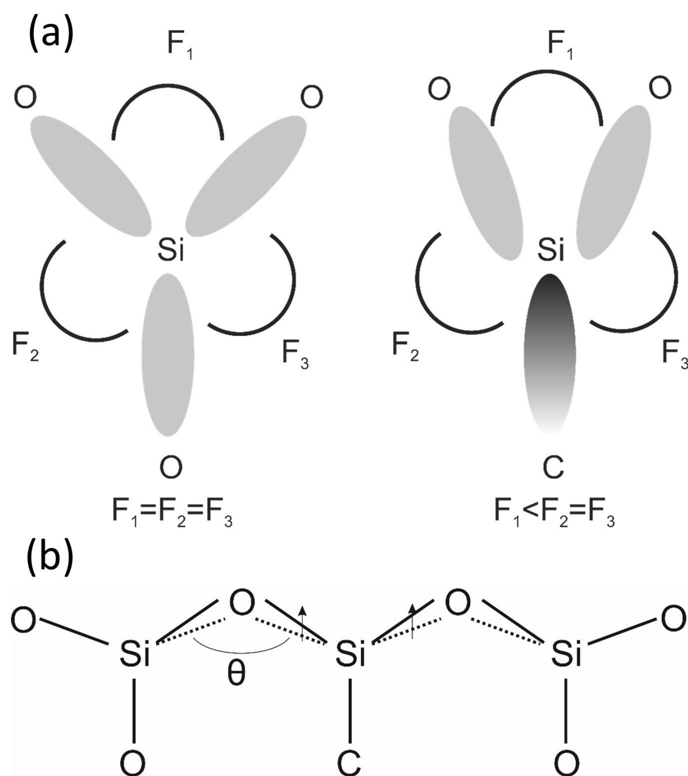

Figure 4.10: (a) Schematic of changes in the location of electron clouds and repulsive electrostatic forces (F_1, F_2, F_3) in a carbon incorporated silica tetrahedra as a result of electronegativity difference between carbon and oxygen, (b) the resulting decrease in the Si-O-Si bond angle as the result of carbon incorporation. The figure is adapted from [110].

in the porosity of the films and also the smaller Si-O-Si bond angles and a more compact silica structure (i.e., higher density silica).

Table 4.1: Curve fitting results of the FT-IR spectra of the heat-treated and H^+ and N^{2+} ion irradiated films.

Film condition	TO peak center (cm^{-1})	Si-O-Si bond angle(°)	I(LO)/I(TO)	I(O-Si-C)/I(TO)
Green	1083	145	1.15	0
H^+-10^{13} ions/cm^2	1080	144	1.2	0
H^+-10^{14} ions/cm^2	1075	142	1.18	0
H^+-10^{15} ions/cm^2	1077	142	1.2	0
H^+-10^{16} ions/cm^2	1079	144	0.83	0.48
H^+-2×10^{17} ions/cm^2	1064	139	0.27	0.27
N^{2+}-10^{13} ions/cm^2	1078	144	1.23	0
N^{2+}-10^{15} ions/cm^2	1072	142	0.79	0.46
N^{2+}-5×10^{15} ions/cm^2	1050	135	0.19	0.62
500 °C	1051	136	1.02	1.42
800 °C	1080	144	0.37	0.12

4.2.3 Raman spectroscopy characterization of free carbon clusters

In order to characterize the free carbon within the films, Raman spectroscopy was performed. Based on the heat-treatment temperature and irradiation conditions, different films exhibit carbon related D and G Raman modes. In general, the films ion irradiated at the highest fluences or heat-treated at intermediate temperatures exhibit carbon related Raman modes. This is discussed below.

The Raman spectroscopy results are presented in Figs. 4.11, 4.12, and 4.13 for the heat-treated, H^+ irradiated, and N^{2+} irradiated films, respectively. In addition to signature Raman D and G modes in the 1200-1700 cm^{-1} range, it is possible to observe weaker modes from the silicon substrate in the same region. The Raman modes between 2700-3000 cm^{-1} originate from C-H bonds in CH_3. The broad mode between 2400-3400 cm^{-1} is the second order Raman mode of amorphous or nanocrystalline carbon [35, 118].

The green film does not exhibit any Raman mode and the spectrum is overwhelmed by a broad, featureless emission. The thin film heat-treated at 500 °C exhibits carbon related D and G modes. This is an indication of the formation of free carbon during heat-treatment. However, after heat-

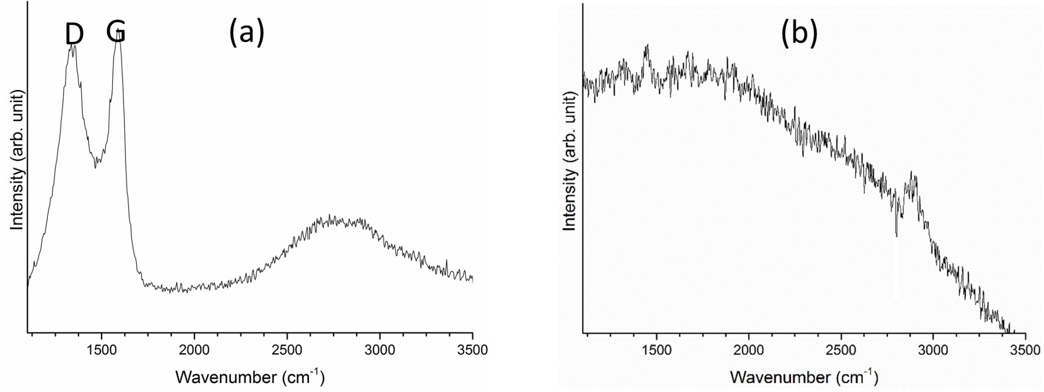

Figure 4.11: Raman spectra of the films heat-treated at a) 500 °C and b) 800 °C.

treatment at 800 °C, the D and G modes disappear. The Raman responses of both heat-treated films are consistent with the thermal decomposition of TEOS and MTES [17, 119]. The final product of the thermal decomposition of thin films is simply amorphous silica and therefore it is not expected to observe any carbon modes after heat-treatment at 800 °C. Some traces of C-H related modes, located between 2700-3000 cm^{-1}, are still visible after heat-treatment at 800 °C. The background emission observed in the Raman spectra of the films after heat-treatment at 800 °C may be related to the remaining organic materials.

Films irradiated with H^+ ions at lower fluences (10^{13} and 10^{14} ions/cm^2) do not exhibit any carbon related Raman modes. The spectra of films irradiated at 10^{15} and 10^{16} ions/cm^2 fluences are overwhelmed by a strong background emission and so, no possible Raman modes can be observed. However, the films irradiated at higher fluences (10^{17} and 2×10^{17} ions/cm^2) exhibited D and G Raman modes. Similarly, the low fluence N^{2+} irradiated film (10^{13} ions/cm^2) does not exhibit any D and G modes. However D and G Raman modes are present in the Raman spectra of the films irradiated at high fluences (10^{15} and 5×10^{15} ions/cm^2).

In order to identify the nature of free carbon in the ion irradiated and heat-treated films, in particular the size of the free carbon clusters, curve fitting was performed on the Raman spectra. Curve fitting with two Gaussian peaks resulted in the best fit for the Raman response of the irradiated films. The Raman spectrum of the film heat-treated at 500 °C is better fitted using a BWF lineshape. Prior to curve fitting, a linear background subtraction is performed. The linear background originates from the presence of residual hydrogen atoms within the carbon clusters [120]. A summary of the results is presented in Table 4.2.

Free carbon formed during H^+ irradiation has a similar Raman response for all fluences, where the G mode spectral center is located around 1580 cm^{-1} and the I(D)/I(G) intensity ratio is approx-

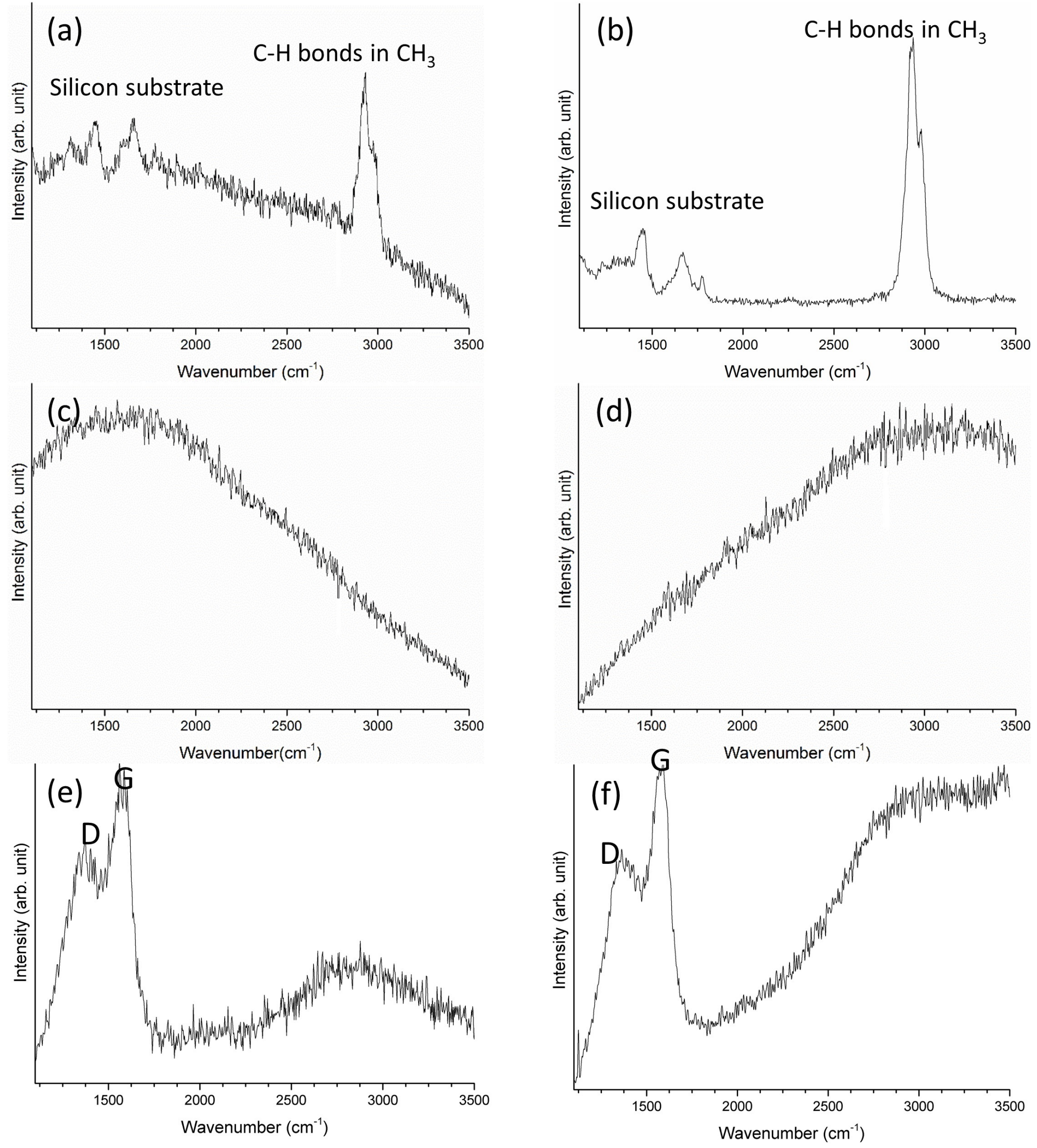

Figure 4.12: Raman spectra of the H^+ irradiated films at different fluences: a) 10^{13} ions/cm^2 b) 10^{14} ions/cm^2 c) 10^{15} ions/cm^2 d) 10^{16} ions/cm^2 e) 10^{17} ions/cm^2 and f) 2×10^{17} ions/cm^2.

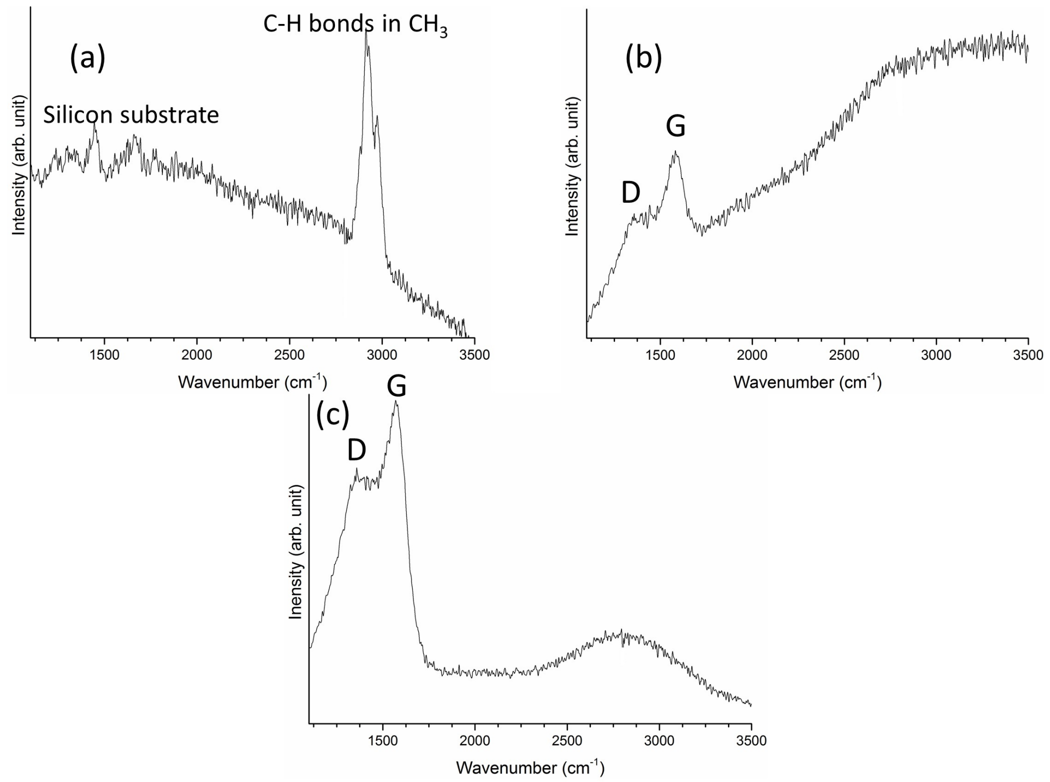

Figure 4.13: Raman spectra of the N^{2+} irradiated films at different fluences: a) 10^{13} ions/cm^2 b) 10^{15} ions/cm^2 and c) 5×10^{15} ions/cm^2.

Table 4.2: Curve fitting results of the Raman spectra of the heat-treated and H^+ and N^{2+} irradiated films exhibiting carbon related D and G Raman modes.

Film condition	W(G) (cm^{-1})	FWHM(G) (cm^{-1})	I(D)/I(G)
H^+-10^{17} ions/cm^2	1583	112	1.15
H^+-2×10^{17}ions/ cm^2	1582	115	1.11
N^{2+}-10^{15} ions/ cm^2	1577	107	1.06
N^{2+}-5×10^{15} ions/ cm^2	1561	160	1.09
Heat-treated at 500 °C	1596	94	1.75

imately 1.1. Raman spectrum of the film irradiated with N^{2+} ions with a fluence of 10^{15} ions/cm^2 is also similar to that of the H^+ irradiated films. However, the film irradiated with N^{2+} ions with a fluence of 5×10^{15} ions/cm^2 exhibits a lower G mode spectral center (1560 cm^{-1}) with the same intensity ratio, which is an indication of a higher level of disorder (destruction of the graphite sixfold rings), as discussed in Section 2.4.1. This film also has a higher G mode peak width which is another indication of higher disorder. Based on the spectral center of the G mode and intensity ratio of the D and G modes (I(D)/I(G)) and the discussion in Section 2.4.1, it can be stated that for all the irradiated films, free carbon consists of disordered and almost entirely sp^2 hybridized carbon with cluster sizes of less than 20 Å. The nature of free carbon formed from heat-treatment is different than the free carbon formed from ion irradiation. The Raman spectrum of the film heat-treated at 500°C, exhibits a I(D)/I(G) intensity ratio of 1.75 and a G mode spectral center of approximately 1600 cm^{-1}. Based on the discussion in Section 2.4.1, These are indicators of nanocrystalline graphite with average size larger than 20 Å.

In addition, Raman spectroscopy results can also be used to estimate the size of free carbon clusters within the films. For disordered carbon with small cluster sizes ($\leq$ 20 Å), the cluster size is estimated from the equation:

$$\frac{I(D)}{I(G)} = C'(\lambda)L_a^2 \quad (L_a \leq 20 \text{ Å}) \tag{4.1}$$

where C' is a constant related to the laser wavelength, λ is the excitation wavelength, and L_a is the cluster size [35]. For a 532 nm laser source, C'(532 nm) has not been reported. The following method is utilized to estimate the value of C'(532 nm). This value is necessary in order to estimate the size of the carbon clusters in the ion irradiated films.

For larger clusters ($L_a \geq$ 20 Å), the cluster sizes can be estimated from

$$\frac{I(D)}{I(G)} = C(\lambda)/L_a \quad (L_a \geq 20 \text{ Å}) \tag{4.2}$$

where C(λ) is estimated from the equation [121]:

$$C(\lambda) = C_0 + \lambda C_1 \tag{4.3}$$

where C_0 and C_1 are constants with values of C_0= -126 Å and C_1=0.033 [121]. So, for a 532 nm laser, C(532 nm) is estimated as 50 Å. Assuming continuity between Equations 4.1 and 4.2, the right side of equations are going to have an identical value at L_a=20 Å. By equating the two equations at L_a=20 Å and knowing the value of C(532 nm), C'(532 nm) is estimated as 0.006. Based on this value, the average cluster size for all of the irradiated films is estimated from Equation 4.1 to be about 1.3 nm. The variations in the carbon cluster size of different ion irradiated films are not large.

The crystallite size of graphite in the heat-treated film is estimated from Equation 4.2 to be about 2.8 nm.

The same method has been previously utilized for estimating the value of $C'(514 \text{ nm})$ [35, 122]. The validity of the approach has been confirmed previously as well by comparing Raman spectroscopy and TEM results. Previous studies have shown the presence of two different regions ($L_a \geq 20$Å and $L_a \leq 20$Å) in the relationship between the I(D)/I(G) intensity ratio and cluster size and have confirmed the continuity of the two regions for various laser excitation sources used in studies performed on ion irradiated carbon [123, 124].

4.2.3.1 Residual hydrogen bonds within the ion irradiated films

Although after irradiation, even at the highest fluences, there is still residual hydrogen left within the films (Fig. 4.2), there is no sign of any hydrogen related modes in the Raman and FT-IR spectra. Figure 4.14 shows the Raman spectra of two films irradiated with H^+ ions at fluences of 10^{14} and 2×10^{17} ions/cm^2. For clarity, the spectra are presented after background subtraction. After irradiation at the lower fluence, two well-defined Raman modes at 2930 and 2980 cm^{-1} can be observed that are related to C-H vibrations [125]. The Raman modes between 1200-1700 cm^{-1} are related to the silicon substrate. However, after irradiation at the higher fluence (2×10^{17} ions/cm^2), the C-H related Raman modes disappear. The D and G modes are present after irradiation at the higher fluence along with a broad, featureless Raman mode between 2400-3400 cm^{-1} which is the second order Raman mode of amorphous or nanocrystalline carbon [35, 118]. In addition, all the C-H_x related FT-IR peaks disappear after ion irradiation at higher fluences (Figs. 4.7, and 4.8). The absence of any methyl-related mode in both the FT-IR and Raman response of the films indicates that the methyl groups are not present in the final microstructure of the films after high fluence ion irradiation. Residual hydrogen might be present within the free carbon clusters, as it has been reported before that hydrogen stabilizes the graphite structure by terminating dangling bonds on the aromatic rings, especially in disordered carbon [126, 127]. The presence of C-H bonds which are not part of any methyl group was also speculated before as the reason for lack of the methyl-related peaks in the FT-IR spectra of the ion irradiated polymer films [94]. In order to test this hypothesis, photoluminescence spectra of ion irradiated films that exhibit carbon D and G modes are also collected, and are presented in Fig. 4.15. The spectra in Fig. 4.15 are normalized to the maximum intensity. No C-H related mode is observed in the FT-IR and Raman spectra of any of these films. However, there is a broad peak centered between 600 to 700 nm in the PL spectra of all the films, which is an indication of the hydrogen content of carbon clusters. The peaks between 550-

600 nm and 625-650 nm are carbon Raman modes. This PL emission is reportedly due to electron hole pair recombination within sp^2 bonded carbon [120, 127]. The introduction of hydrogen to the carbon structure increases the intensity of this peak, primarily due to the saturation of non-radiative recombination sites (i.e., dangling bonds) by hydrogen [127]. Thus, it can be claimed that residual hydrogen is primarily located within the free carbon clusters as individual C-H bonds. In addition, a decrease in the hydrogen content of the films (Fig. 4.2) is accompanied by a decrease in the intensity of the emission, further confirming this hypothesis.

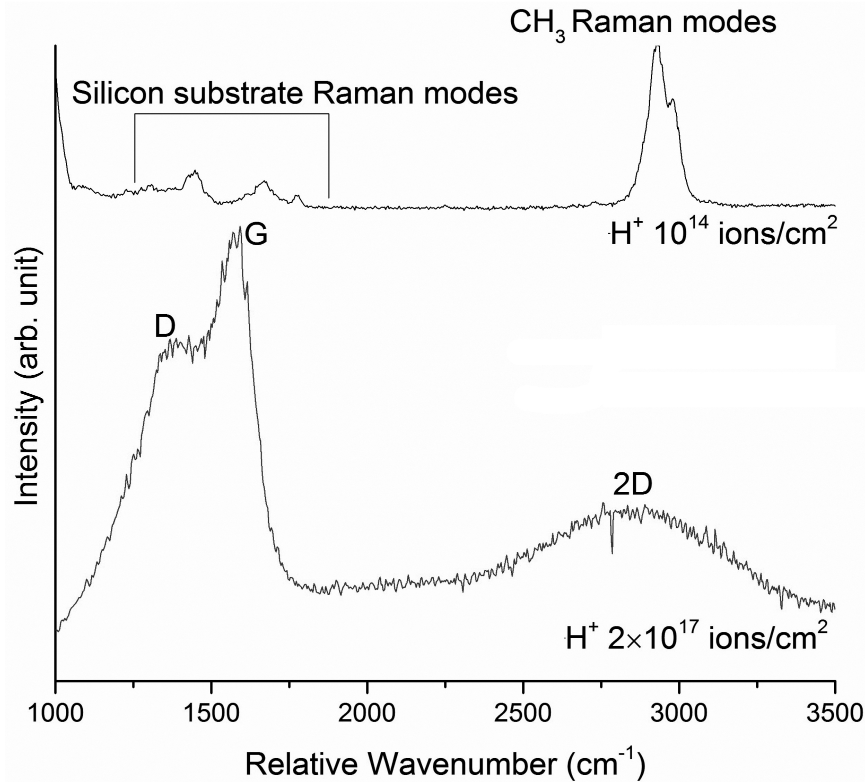

Figure 4.14: Raman spectra of two H^+ irradiated films at fluences of 10^{14} and $2{\times}10^{17}$ ions/cm^2.

4.2.4 XPS characterization of the films irradiated with N^{2+} ions

As discussed previously, one major feature of SiOC glasses is the incorporation of carbon within the silica. Previous studies using NMR [69], FT-IR [108, 109], and XPS [128–131] have confirmed the incorporation of carbon within the silica network. Our studies using FT-IR spectroscopy also confirmed carbon incorporation within the silica network, as discussed in Section 4.2.2. XPS experiments were performed on ion irradiated and heat-treated films. XPS spectroscopy is capable of

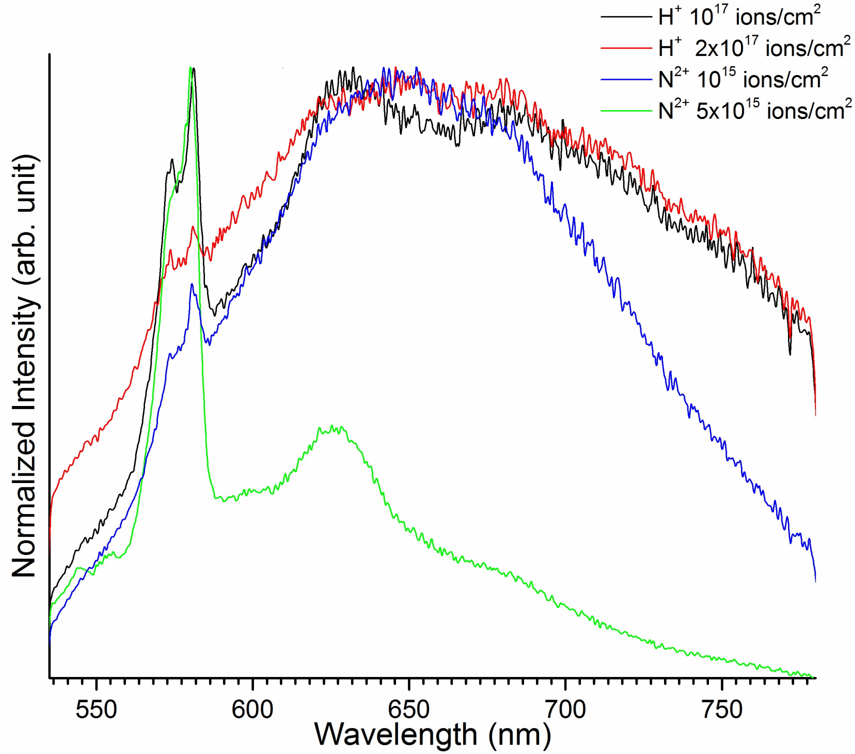

Figure 4.15: Photoluminescence spectra of ion irradiated films that possess free carbon clusters. The peaks between 550-600 nm and 625-650 nm are carbon Raman modes.

differentiating between different SiO_xC_y tetrahedra. Based on the difference between the binding energy of the Si 2p line of silica and silicon carbide, the binding energies of various SiO_xC_y tetrahedra (SiO_4, SiO_3C, SiO_2C_2, $SiOC_3$, as well as SiC_4) have been determined previously as 103.5, 102.7, 101.9, 101.1 and 100.3 eV, respectively [129, 130, 132]. The validity of this method has been confirmed by comparing XPS and NMR results [131]. Thus, a shift toward lower binding energies can be related to the incorporation of carbon within the silica network and the formation of carbon rich tetrahedra.

The XPS Si 2p spectra of different films after ion irradiation with light ions are presented in Figure 4.16. For comparison, the spectra of a heat-treated film is also included in the figure. The Raman and FT-IR results have previously indicated that there are organic bonds in the film irradiated with N^{2+} with a fluence of 10^{13} ions/cm^2 (e.g., Si-CH_3). The Si 2p line of Si-CH_3 bond has lower binding energy than silica [133, 134]. Therefore, the Si 2p line of the film irradiated with N^{2+} ions at a fluence of 10^{13} ions/cm^2 is located at a lower binding energy than the other two film (heat-treated film and N^{2+} irradiated film at a fluence of $5{\times}10^{15}$ ions/cm^2) which both have predominantly inorganic silica bonds.

When two films with inorganic bonds are compared, the XPS results indicate that compared to the heat-treated film, the Si 2p line of the film irradiated with N^{2+} at 5×10^{15} ions/cm^2 shifts to lower binding energies. This is an indication of carbon incorporation in the silica structure after ion irradiation.

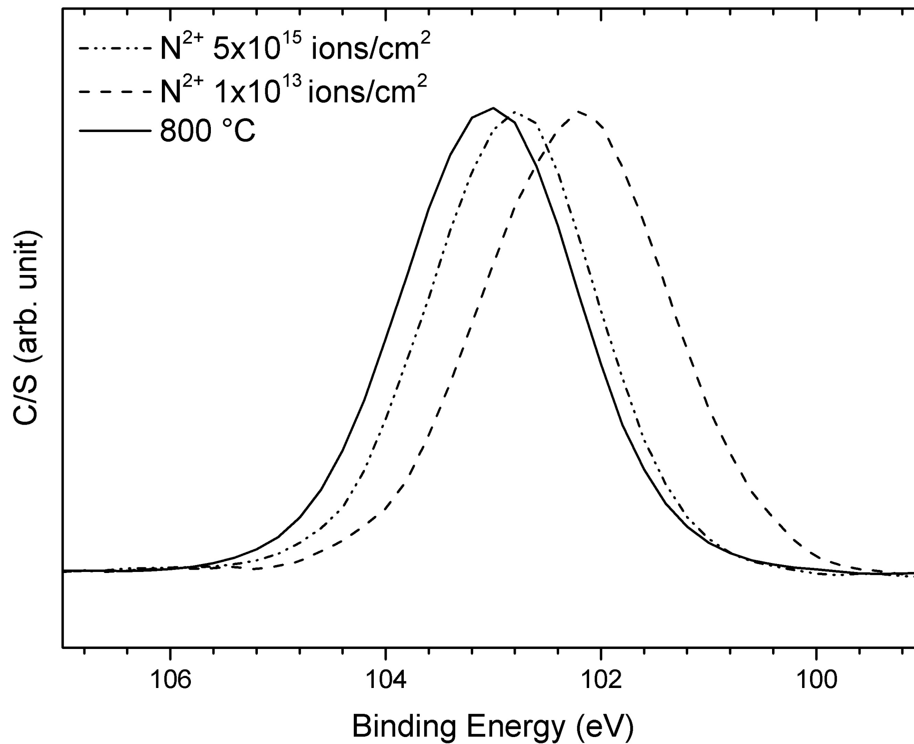

Figure 4.16: The XPS Si 2p spectra after irradiation with N^{2+} ions. For comparison, the XPS spectra of a heat-treated film is also included.

Figure 4.17 shows the C 1s XPS spectra of the films after ion irradiation with N^{2+} ions. For comparison, the XPS spectra of a heat-treated film is also shown. The main C 1s peak has either originated from C-C or CH_3 bonds [130]. After ion irradiation with N^{2+} at a fluence of 10^{13} ions/cm^2, Raman and FT-IR results indicate that the film mostly consists of organic bonds. The Raman spectrum of the film heat-treated at 800 °C (Fig. 4.11 (b)) also indicates that there is still residual CH_3 within the heat-treated films. So, the observed C 1s peak of the heat-treated film and the film irradiated with N^{2+} at a fluence of 10^{13} ions/cm^2 is related to organic carbon bonds. No sign of C-C bonds is observed in the Raman spectra of either films.

The Raman and FT-IR results also indicate that the organic Si-CH_3 bonds are not present in the N^2 irradiated film at a fluence of 5×10^{15} ions/cm^2. Raman spectrum of the film indicates the presence of predominantly sp^2 bonded carbon clusters. Therefore, the peak in the C 1s XPS spectra

of the film irradiated with a fluence of N^{2+} at 5×10^{15} ions/cm^2 has originated from the free carbon clusters. The binding energy of the C 1s XPS peak is close to 284.4 eV, which is the binding energy of sp^2 bonded carbon [135]. The shoulder on the higher binding energy side of the main peak consists of a C=O peak at approximately 286 eV and a C-O peak at 287-290 eV [136]. The location of these peaks on the shoulder are indicated in Appendix A.

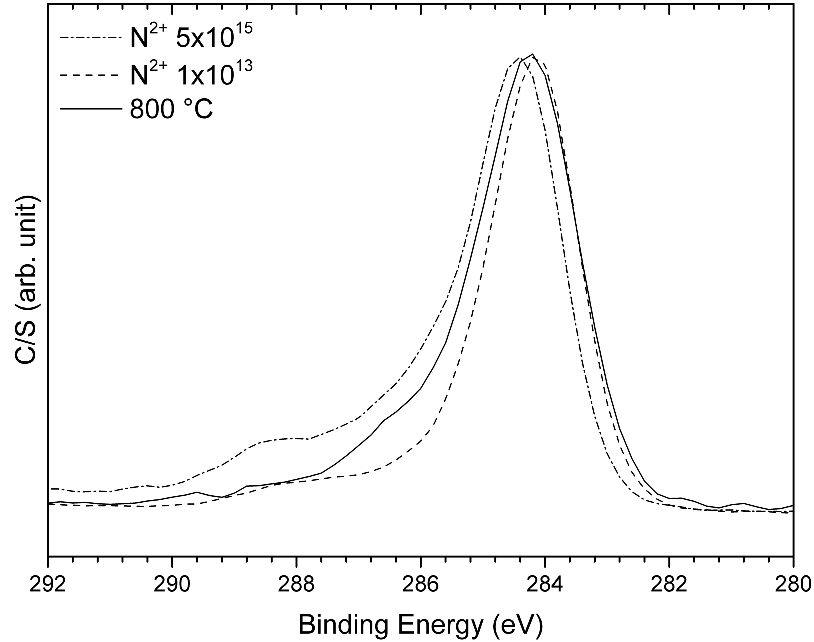

Figure 4.17: XPS C 1s spectra of the films irradiated with N^{2+} ions. For comparison, the XPS spectra of a heat-treated film is also included.

The O 1s XPS spectra of the films after ion irradiation was also collected, but the differences between the spectra of the ion irradiated film with N^{2+} ions at a fluence of 5×10^{15} and the heat-treated film is minimal. There is a small shift in the O 1s binding energy of the irradiated film towards lower binding energies, which may originate from a decrease in the Si-O-Si bond angle, as the decrease in the Si-O-Si bond angle decreases the binding energy of the O 1s spectra [137]. However, the shift is too small to draw a conclusion. The O 1s spectra of the ion irradiated and heat-treated films are presented in Appendix B.

4.2.5 Microstructural configuration of the films irradiated with light ions

The Raman spectroscopy results are consistent with both the FT-IR and ERD/RBS results. The appearance of carbon Raman modes occurrs at the same fluences that a significant hydrogen loss and incorporation of carbon into the silica structure is observed. In addition, XPS also confirms the

incorporation of carbon within the silica network. It can be concluded that after hydrogen release during irradiation, carbon either bonds with other carbon atoms to form free carbon clusters, as inferred from the Raman spectroscopy results, or bonds with silicon, as inferred from the FT-IR spectroscopy and XPS results.

Figure 4.18 shows the chemical composition of the ion irradiated and heat-treated films, presented in the chemical composition triangle. The chemical composition triangle has been designed to predict the final phases of a heat-treated SiOC material as a function of chemical composition. One underlying assumption in building the chemical composition triangle is that all the phases have a near-stoichiometric formualtion (e.g., SiC, SiO_2). However, ion irradiation may lead to the formation of phases that are not stoichiometric (i.e., SiO_x, Si_yC_z). The formation of non-stoichiometric silica as a result of ion irradiation has been shown before [52]. The reason is that ion irradiation of silica induces a large concentration of vacancies in silica which leads to a non-stoichiometric composition and may render the chemical composition triangle unsuitable for the predicting the final phases in an ion irradiated SiOC. As shown in Fig. 4.18, the predicted microstructure of H^+ and N^{2+} irradiated films is a combination of free carbon and silica for all irradiation, which is in agreement with the experimental results. Therefore, it can be stated that the chemical composition triangle can predict the final present phases in the films irradiated with H^+ and N^{2+} ions. The concentration of individual phases, however, may be different from what can be estimated from the chemical composition triangle.

For the heat-treated films in the present study, there is a decrease in the carbon content with increasing temperature, until the chemical composition of the films is located close to SiO_2 after heat-treatment, which is in agreement with the observed microstructure of heat-treated thin films.

The exact configuration of carbon within the silica structure is yet to be determined. Previous studies on heat-treated silicon oxycarbide materials have suggested two models for the microstructural configuration of carbon and silica: either 1.) an interconnected network of carbon with silica nanodomains [29, 31] or 2.) a porous silica network with isolated free carbon clusters filling the voids [68, 69]. A schematic of the two models is presented in Fig. 2.8. The observation of incorporation of carbon within the silica network from XPS and FT-IR results is most likely related to the atomic bonds at the interface of carbon and silica. However, FT-IR, XPS, and Raman spectroscopy results are inadequate to determine the final microstructural configuration of the irradiated films.

In the following, it will be argued that isolated free carbon clusters within a silica network is a plausible configuration in the ion irradiated films. In most cases, ion irradiation and ion implantation lead to the synthesis of isolated nanoparticles within the irradiated matrix. Examples include

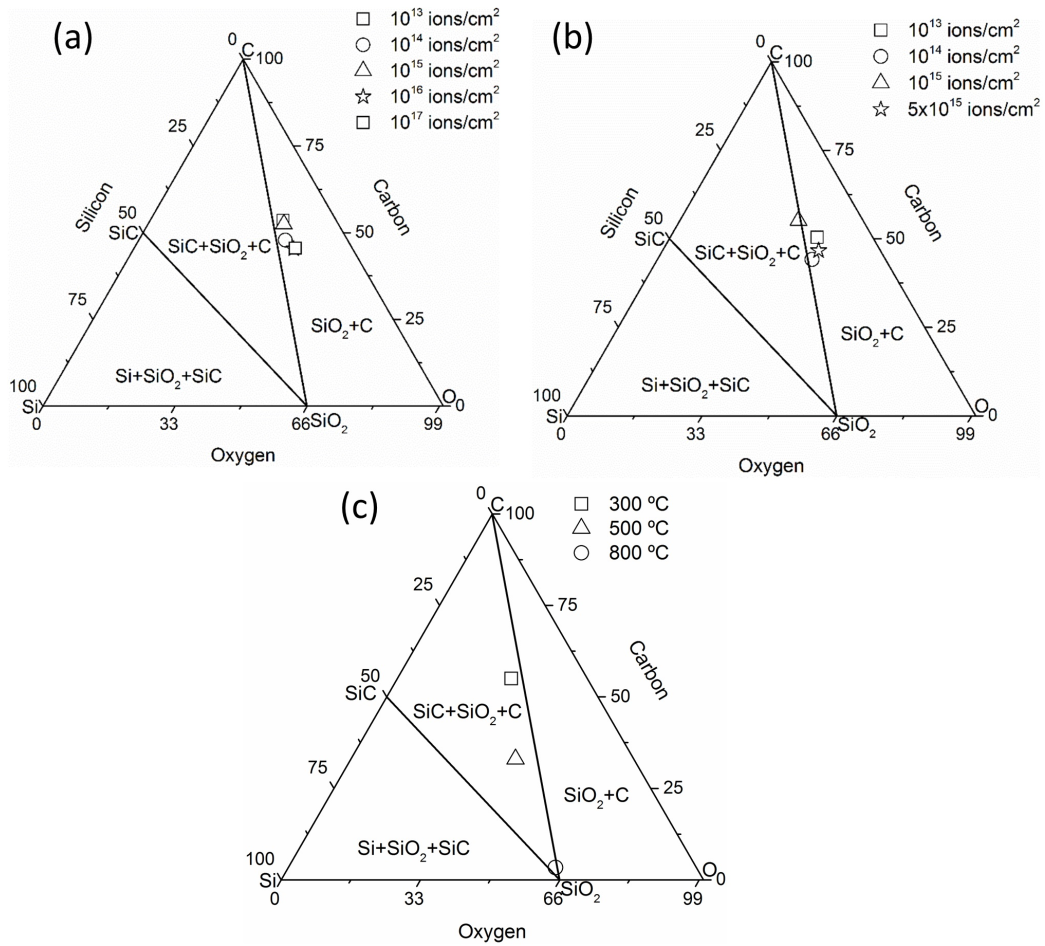

Figure 4.18: Chemical composition triangle of a) H^+ ion irradiated b) N^{2+} ion irradiated and c) heat-treated films, predicting the final phases present within the films based on a model developed for heat-treated films

synthesis of secondary phases through ion implantation [138, 139], as well as synthesis of diamond nanoparticles within highly oriented pyrolytic graphite by low energy ion irradiation [140, 141]. In the case of nanodiamond synthesis, HRTEM revealed that the synthesis was localized to the regions around the ion tracks, and that the nanodiamond particles were isolated particles within the matrix, rather than a homogenous transformation of all the graphite to diamond. It may be argued that because, unlike heat-treatment, the energy deposition within the film is not uniform during ion irradiation, the formation of an interconnected network seems unlikely. That being said, there is evidence that an interconnected network has formed during ion irradiation [142, 143].

Previously, scanning probe microscopy (SPM) images showed that the ion irradiation of polymers with 120 MeV gold ions led to the formation of isolated surface features ranging in size from 25 to

70 nm [144]. In addition, the formation of isolated clusters of free carbon with average size of 4 nm in silicon oxycarbide films irradiated with 3-120 MeV gold ions was confirmed by TEM results [86,145]. The synthesized free carbon clusters in the present study were the results of ion irradiation with lower energies and had smaller size than previous studies [86, 144, 145].

The utilization of lower energy ions in the current study may also lead to a different microstructure than those of heavy ions. So, in the following, the effect of ion energy on the possible formation of an interconnected network is examined. The formation of an amorphous interconnected network of carbon nanowires by ion irradiation was previously studied [142]. It was shown that increasing the deposited energy enhances the formation of an interconnected carbon network and so, the formation of an interconnected carbon network after irradiation with lower energies is unlikely. The reason is that the formation of an interconnected carbon network depends on the total deposited energy during irradiation that induces bond disorder and vacancies within the carbon structure and thus creates the driving force for the merging of individual carbon clusters. Even though there is a difference between irradiation of carbon nanotubes and sol-gel derived polymers, the same mechanism may be assumed to be responsible for a hypothetical formation of an interconnected carbon network. The formation of an interconnected carbon network is a result of bonding between highly disordered carbon clusters (e.g., dangling bonds, damaged graphite sixfold rings) to form a continuous carbon network. Ion irradiation with high energy ions in previous studies was not sufficient for the formation of an interconnected network [86, 145] and irradiation with higher energy ions led to formation of isolated free carbon clusters. So, an argument can be made that ion irradiation with lighter ions, including the current study, also leads to formation of isolated free carbon clusters within the silica network.

Based on the Raman, FT-IR, and photoluminescence spectroscopy results, as well as the XPS and XRD results, a microstructure for the films after ion irradiation with H^+ and N^{2+} ions is proposed. A schematic of the proposed microstructural configuration of the films irradiated with H^+ and N^{2+} ions is shown in Fig. 4.19. Figure 4.19 (a) shows the microstructure of the films after ion irradiation with H^+ ions at the highest fluence. The structure is composed of isolated carbon clusters within a silica matrix. The silica phase was amorphous silica with an average bond angle of 139°. Carbon clusters consist of hydrogenated and defective sp^2 bonded carbon. The interface of carbon and silica consists of carbon-rich SiO_xC_y tetrahedra. The microstructure of the N^{2+} irradiated films with the highest fluence (Figure 4.19 (b)) also consists of amorphous carbon and silica. The amorphous silica has an average bond angle of 135°. Carbon clusters in N^{2+} irradiated films were also defective sp^2 bonded carbon. While the carbon clusters in both films are hydrogenated, the

hydrogen concentration of carbon clusters is lower in N^{2+} irradiated film. The interface of carbon and silica consists of carbon-rich SiO_xC_y tetrahedra.

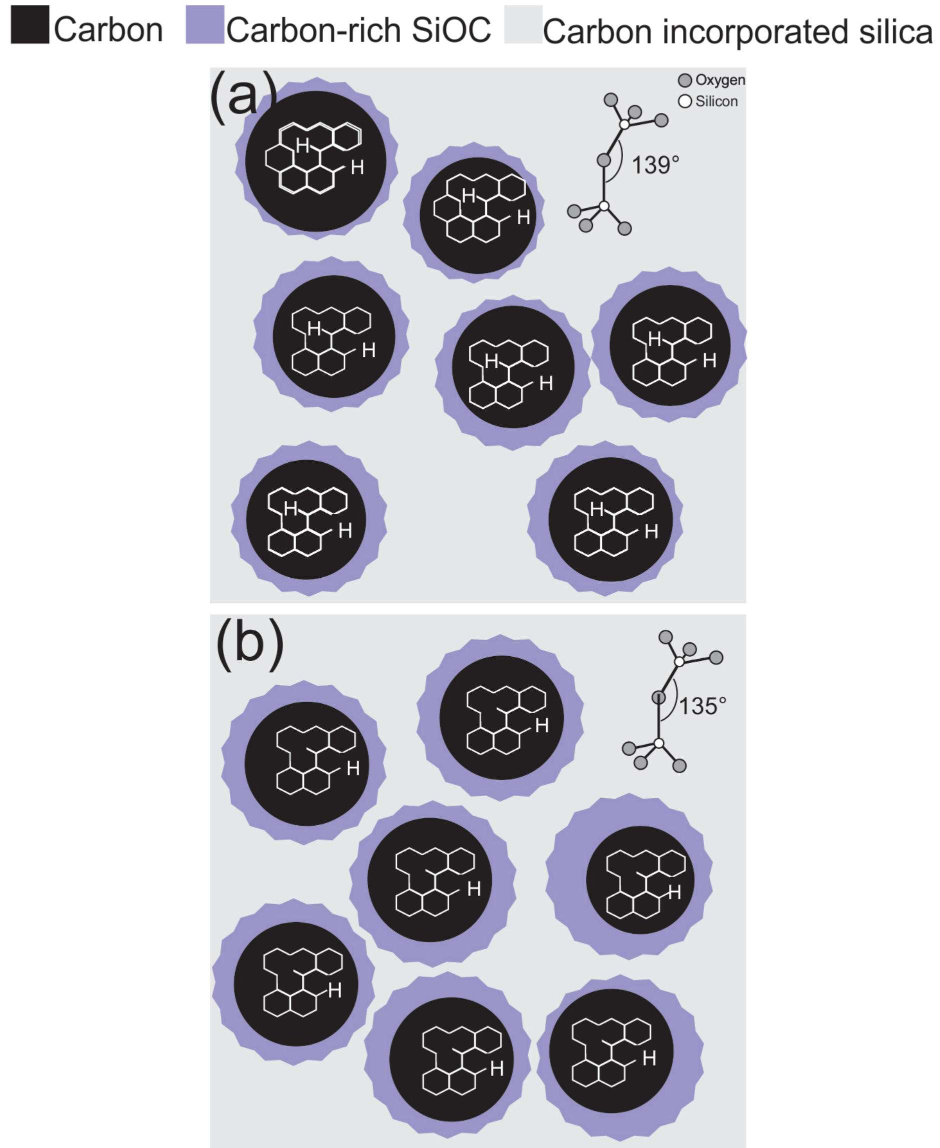

Figure 4.19: Microstructural configuration of films after irradiation with a) H^+ ions at a fluence of 2×10^{17} ions/cm^2 and b) N^{2+} ions at a fluence of 5×10^{15} ions/cm^2.

4.2.6 Mechanical properties of the films after ion irradiation with light ions

Figure 4.20 shows the variations of film thickness, reduced elastic modulus and hardness of the films as a function of fluence. The variations in the film thickness follows the same trend as density

(Fig. 4.4). For both ion species, there is an increase in hardness and reduced elastic modulus with increasing fluence. The hardness and reduced elastic modulus of the H^+ irradiated film after irradiation at the highest fluence (2×10^{17}) are 4.3 GPa and 46 GPa, respectively. After irradiation with N^{2+} with the highest fluence, the hardness and reduced elastic modulus of the film are 7.3 GPa and 79.3 GPa, respectively. Factors including decomposition of the starting organic materials and a decrease in the porosity of the films have contributed to the increased hardness and elastic modulus of the films after irradiation at higher fluences. For comparison, the hardness and reduced elastic modulus of the heat-treated film at 800°C are measured to be 1.3 GPa and 19.5 GPa, respectively.

The introduction of carbon within the silica network affects the elastic modulus of the films in two ways. One is the formation of inorganic Si-C bonds as a result of the formation of carbon-rich SiO_xC_y tetrahedra, and the other is the reduction of the Si-O-Si bond angle. In addition to carbon incorporation within the silica network, the atomic displacement and vacancies introduced by ion irradiation, in combination with thermal spikes, also decrease the Si-O-Si bond angle in silica. This reduction in the bond angle of silica, in combination with the elastic deformation mechanisms of amorphous silica may explain the increase in reduced elastic modulus. The presence of free volume in amorphous silica leads to an alternative elastic deformation mechanism, referred to as pantograph deformation [50], which explains the dependence of the elastic modulus on bond angle. This mechanism involves elastic deformation not by pure bond length change, but through a small decrease in the bond angle of the bridging oxygen atoms. This mechanism requires smaller forces compared to pure bond length change. As the bond angle decreases as a result of ion irradiation, a higher proportion of stress is applied for pure bond length change [50], which leads to higher elastic modulus. The positive effect of compaction (reduction in bond angle) on increasing elastic modulus of silica has been demonstrated [146]. As discussed in Section 2.4.2, reducing the bond angle of silica will increase the elastic modulus.

Many studies have focused on the positive effect of ion irradiation on the elastic modulus of amorphous silica. Ion irradiation is found to increase elastic modulus of both amorphous [147] and nanoporous [148, 149] silica. In addition, it has been found that other parameters that affect the Si-O-Si bond angle of silica, e.g., temperature or applied pressure, also affect the elastic modulus [57, 150, 151]. It has been reported that increasing the indentation temperature to 400 °C, can increase the elastic modulus to 80 GPa [152]. As discussed before, the exact mechanism of reduction of bond angle has been studied previously by molecular dynamics simulations [114, 115], and it was found that the introduction of vacancies and displacement of atoms leads to a structural relaxation that results in a decreased bond angle. In addition, thermal spikes also lead to a decreased bond

angle [114, 116]. The introduction of carbon to the silica network and formation of carbon rich SiO_xC_y tetrahedra and formation of Si-C bonds may also increase the elastic modulus of the films.

The bond angle of films irradiated with H^+ with a fluence of 2×10^{17} ions/cm^2 is estimated to be 139° and previous studies on the effect of bond angle on the elastic modulus of silica have indicated that this level of reduction in the bond angle is similar to the structure of silica under 4 GPa pressure and does not affect the elastic modulus of silica [57]. Thus, the enhancement in the elastic modulus of H^+ irradiated films compared to the heat-treated film is only the result of decomposition of the starting organic materials and reduction in porosity.

The combined effect of the formation of carbon rich SiO_xC_y tetrahedra and a reduction in the bond angle may explain the elastic modulus of the films after irradiation at 5×10^{15} ions/cm^2 with N^{2+} ions. Previous studies have shown that bond angle of 135°, similar to the structure of silica under the pressure of 6.4 GPa, is the onset angle where the decrease in bond angle leads to enhancement of the elastic modulus [57], and so a slight increase in the elastic modulus of the silica phase in the film in comparison to fused silica is expected. In order to compare the results in the literature with the findings in the current study, the measured reduced elastic modulus is converted to elastic modulus using the procedure described in the literature and the ISO-14577-1:2002 standard [153, 154], where the reduced elastic modulus is related to the elastic modulus of the test specimen through the following equation:

$$\frac{1}{E_r} = \frac{1-\nu_s^2}{E_s} + \frac{1-\nu_i^2}{E_i} \tag{4.4}$$

where E_r is the reduced elastic modulus, ν_s and E_s are the Poisson's ratio and elastic modulus of the test specimen, respectively, and ν_i and E_i are the Poisson's ratio and elastic modulus of the indenter, respectively. The Poisson's ratio and elastic modulus of the diamond indenter are indicated as 0.07 and 1140 GPa, respectively [153,154]. The Poisson's ratio of the irradiated films are not known. The Poisson's ratio of SiC varies between 0.19 to 0.29 [155], graphene has a Poisson's ratio of 0.165 [156], and the Poisson's ratio of silica varies between 0.17 to 0.38, depending on the inter-atomic spacing of silicon and oxygen atoms [57]. Thus, Poisson's ratio is estimated to be 0.25 which is close to the Poisson's ratio of all the possible constituent phases. Based on this assumption, the elastic modulus of the films after irradiation at 5×10^{15} ions/cm^2 with N^{2+} ions is estimated to be 80 GPa which is similar to the expected elastic modulus of silica with the bond angle of 135°. It should be noted that even if the Poisson's ratio estimate is not accurate, the value of elastic modulus will not change significantly. Changing Poisson's ratio from 0.25 to 0.3 or 0.2 changes the value of estimated elastic

modulus by less than 3%.

In addition to Si-O-Si bond angle and formation of carbon rich SiO_xC_y tetrahedra, the hydrogen content of amorphous carbon also affects the elastic modulus of the films. Hydrogenated amorphous carbon has a polymeric nature and is deteriorating to the elastic modulus of the films. The hydrogen release at higher ion energy and fluences and formation of carbon clusters with less hydrogen (Fig. 4.15) is also responsible for the enhancement in the elastic modulus of the films after irradiation with N^{2+} ions. Thus, the higher elastic modulus of the film irradiated at 5×10^{15} ions/cm^2 with N^{2+} ions may be explained by the effect of the formation of carbon rich SiO_xC_y, a reduction in the bond angle of fused silica, and hydrogen release from free carbon clusters. It should be noted that the formation of carbon rich SiO_xC_y is not the dominant mechanism in increasing the elastic modulus of the films, as previous studies on similar ion irradiated films showed that the presence of carbon has a minimal effect on the elastic modulus of N^{2+} irradiated sol-gel derived thin films (Fig. 2.11 and reference [21]). The effect of the changes in the Si-O-Si bond angle on the elastic modulus of the ion irradiated films is consistent with previous results on similar films where a decrease in spectral center of the FT-IR TO peak and an increase in the elastic modulus of the ion irradiated films was observed [21, 157].

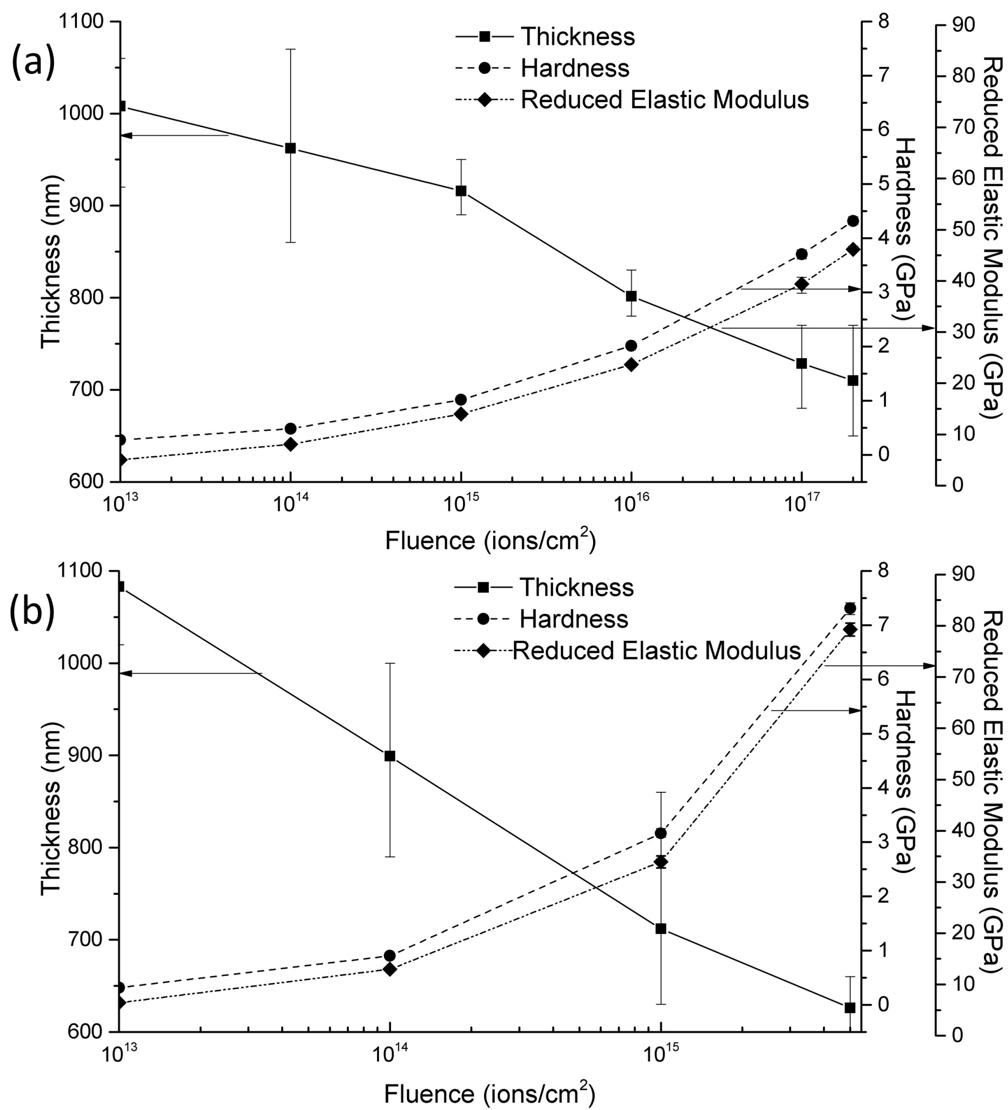

Figure 4.20: The variations in film thickness, reduced elastic modulus and hardness of ion irradiated films as a function of fluence for a) H^+ irradiated films and b) N^{2+} irradiated films. The data is adapted from [158].

4.3 Conversion of films with heavy ions

4.3.1 Chemical evolution of the films after ion irradiation with heavy ions

Figure 4.21 shows the atomic concentration ratio of hydrogen, carbon, and oxygen compared to silicon for films irradiated with 1 MeV Cu^{+}, 4 MeV Cu^{2+}, and 9 MeV Cu^{3+} ions.

After ion irradiation with 1 MeV Cu^{+} ions, there is a decrease in hydrogen, oxygen, and carbon concentration. Ion irradiation with a fluence of 10^{16} ions/cm^2 with 1 MeV Cu^{+} ions leads to almost complete hydrogen depletion. This is an indication of complete conversion of the starting organic materials into a final inorganic phase. In addition, a decrease in both carbon and oxygen concentration can be observed. The carbon loss may be related to the release of carbon as CH_4 during irradiation [93], as discussed in Section 4.2.1.

Ion irradiation with 4 MeV Cu^{2+} and 9 MeV Cu^{3+} ions leads to higher carbon, oxygen, and hydrogen loss. Unlike the light ion species, irradiation with heavy ions decreases the concentration of all three elements. The carbon concentration ratio decreases from 4.4 to 0.8 after ion irradiation with 9 MeV Cu^{3+} at a fluence of 10^{16} ions/cm^2. Similarly, the oxygen ratio decreases from 2.9 to 0.8. High oxygen loss, although not unprecedented [159–163], is not common and is mostly observed in high energy ion irradiation with heavy ions [159,162]. A plausible explanation for carbon and oxygen depletion after ion irradiation with 1 MeV Cu^{+}, 4 MeV Cu^{2+}, and 9 MeV Cu^{3+} ions may be related to the bond dissociation energy of different bonds within the starting materials. Table 4.3 shows the dissociation energy for various TEOS and similar compounds chemical bonds. Assuming that the surrounding chemical environment has minimal effect on the bond energy of a large molecule, e.g., TEOS or MTES, a conclusion can be made about the origin of carbon and oxygen loss. The dissociation energies in Table 4.3 indicate that, in general, breaking bonds that involves carbon and hydrogen bonding (e.g., X-H and X-CH_y bonds) requires less energy than breaking bonds that involve oxygen and silicon bonding (e.g., Si-C_yH_z and X-OC_yH_z). As a result, ion irradiation with lower energies only leads to hydrogen loss. However, higher energy ion irradiation is capable of breaking stronger bonds and leads to oxygen, carbon, and hydrogen loss.

4.3.1.1 Changes in density of the films after ion irradiation

Figure 4.22 shows the variations in the ERD/RBS estimated density of the 1 MeV Cu^{+}, 4 MeV Cu^{2+}, and 9 MeV Cu^{3+} irradiated films. The increase in the density of the films irradiated with 1 MeV Cu^{+} follows the same trend as hydrogen loss. The density of films irradiated with 4 MeV Cu^{2+}, and

Table 4.3: Bond dissociation energy of various chemical bonds in TEOS and similar compounds. The symbol Me stands for methyl (CH_3).

Chemical Bond	Bond Dissociation Energy (KJ/mole)	Reference
$Si(OC_2H_5)_4 \rightarrow Si(OC_2H_5)_3OCH_2+CH_3$	243	[164]
$Si(OC_2H_5)_4 \rightarrow Si(OC_2H_5)_3OCHCH_3+H$	272	[164]
$Me_3SiCH_3 \rightarrow Me_3Si+CH_3$	376	[165]
$Me_3SiOC_2H_5 \rightarrow Me_3SiO+C_2H_5$	390	[165]
$Si(OC_2H_5)_4 \rightarrow Si(OC_2H_5)_3O+C_2H_5$	418	[166, 167]
$Me_3SiOC_2H_5 \rightarrow Me_3Si+OC_2H_5$	485	[165]
$Si(OC_2H_5)_4 \rightarrow Si(OC_2H_5)_3 +OC_2H_5$	552	[166, 167]
Si-O bond in SiO_2	799	[168]

9 MeV Cu^{3+} after ion irradiation with a fluence of 10^{15} and 10^{16} ions/cm^2 is above the density of amorphous silica (2.2 g/cm^3 [168]). The increase in density is at least partially related to the decrease in the Si-O-Si bond angle and compaction of the silica structure, as discussed in Section 4.2.2.2. However, the formation of free carbon (with a density of 2.30-2.72 g/cm^3 [168]) might also aid in increasing the density of the films.

A decrease in the density of the 9 MeV Cu^{3+} irradiated films is observed after irradiation with a fluence of 10^{16} ions/cm^2 which may be related to the removal of larger molecules, as discussed in Section 4.3.1 and the formation of atomic size voids. The formation of porosity after ion irradiation was observed before [169–171] and was attributed to the merging of point defects formed during ion irradiation. The same phenomenon, the formation of atomic-scale voids during ion irradiation due to excessive element removal after ion irradiation with 9 MeV Cu^{3+} may be considered responsible for the decrease in the density of the films after ion irradiation with a fluence of 10^{16} ions/cm^2.

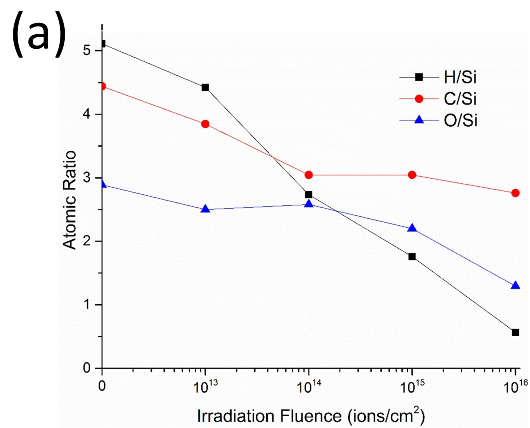

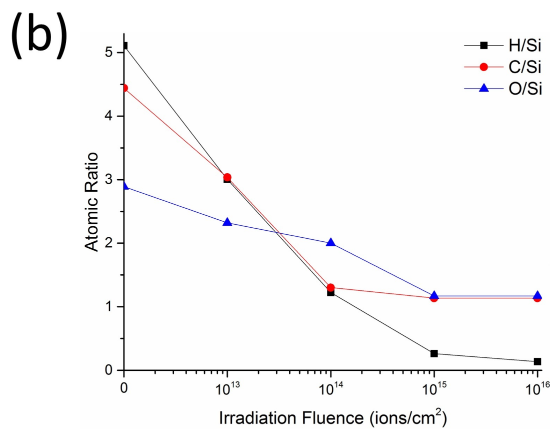

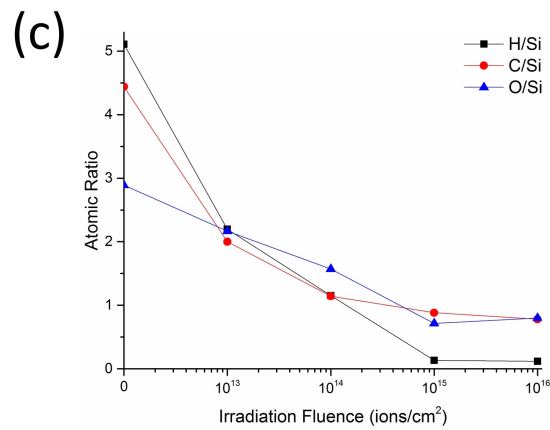

Figure 4.21: Atomic concentration ratios of hydrogen, carbon, and oxygen compared to silicon after ion irradiation with a) 1 MeV Cu^{+} b) 4 MeV Cu^{2+}, and b) 9 MeV Cu^{3+}.

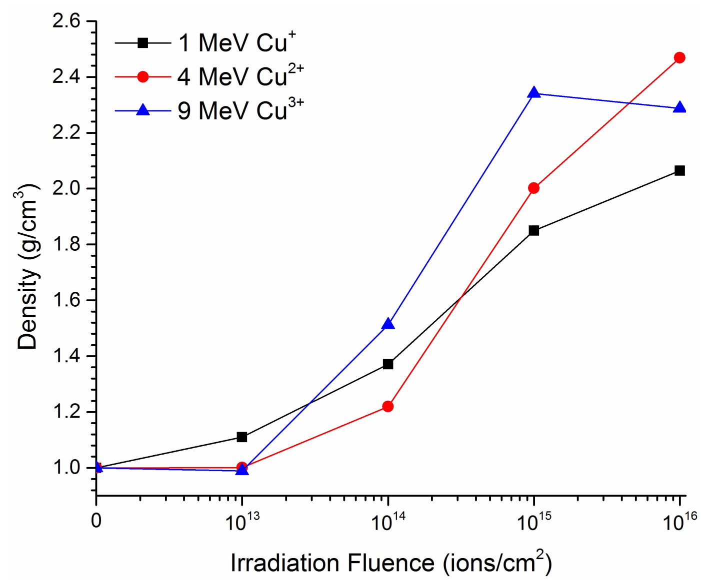

Figure 4.22: Estimated density of the films irradiated with 1 MeV Cu^{+}, 4 MeV Cu^{2+}, and 9 MeV Cu^{3+}.

4.3.2 FT-IR spectroscopy characterization

Figures 4.23, 4.24, and 4.25 show the transmission FT-IR spectra of the films after ion irradiation with 1 MeV Cu^{+}, 4 MeV Cu^{2+}, and 9 MeV Cu^{3+} ions, respectively. Figure 4.26 also shows the reflection FT-IR spectroscopy results of the irradiated films. Similar to the films irradiated with H^{+} and N^{2+} ions, a decrease in the FT-IR peaks related to the starting organic materials is observed. The peaks between 750-800 and 1275 cm^{-1} are from $SiCH_3$ [101]. The small peak at 1450 cm^{-1} is from a C-H bond [102]. The peak around 1670 cm^{-1} is from OH vibrations of adsorbed or entrapped water [103] and the peaks between 2850-3000 cm^{-1} are from C-H_x(x=1,2,3) [100, 104]. All of these peaks are related to the starting materials and there is a decrease in their intensity with increasing fluence for all three ion energies (1 MeV Cu^{+}, 4 MeV Cu^{2+}, and 9 MeV Cu^{3+}). The peaks around 2300 cm^{-1} are related to C=O bonds and originate from the carbon dioxide in the air and insufficient background subtraction and are not related to the films.

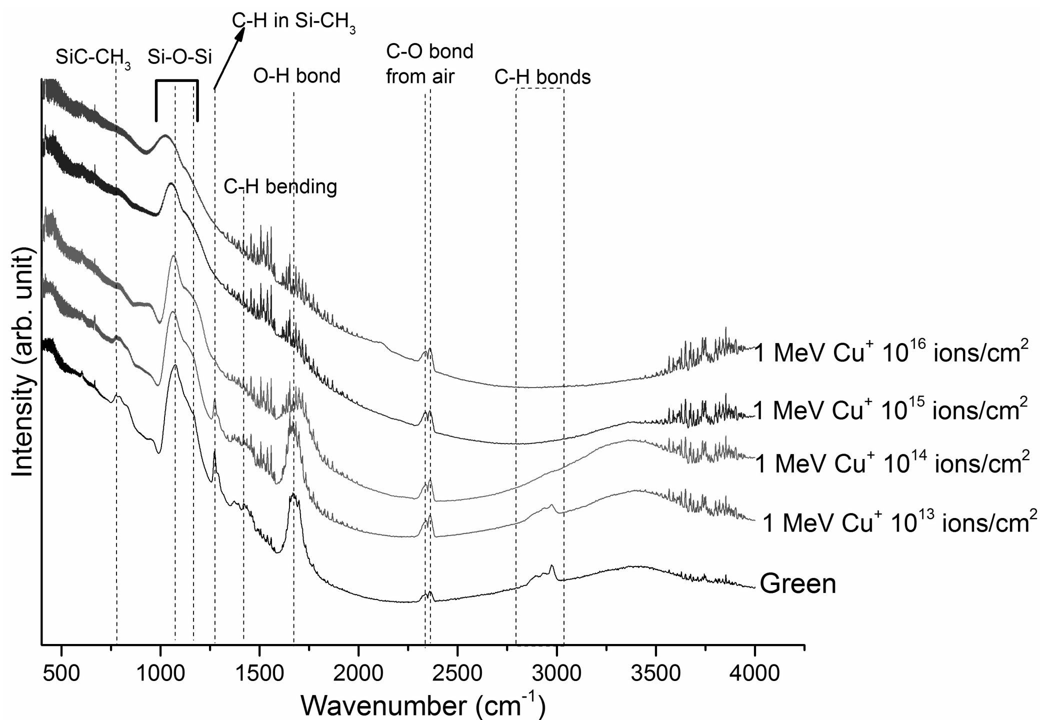

Figure 4.23: Transmission FT-IR spectra of the films irradiated with 1 MeV Cu^{+} ions at different fluences.

The peaks between 900 to 1300 cm^{-1} are related to the Si-O-Si bond and the amorphous silica structure. After irradiation with 1 MeV Cu^{+} ions, no significant changes in the silica related FT-

IR peaks of the films irradiated with a fluence of 10^{13} and 10^{14} ions/cm^2 are observed. However, further increase in the fluence leads to the development of the O-Si-C related peak (at 1140 cm$^-1$) and elimination of the LO peak (at 1200 cm^{-1}). After irradiation at the highest fluence (10^{16} ions/cm^2), the position of the TO peak is decreased to 1030 cm^{-1}, corresponding to a bond angle of 130°. Previous molecular dynamics simulations have shown that bond scission and displacements of atoms as a result of ion irradiation are follows by a structural relaxation that results in a more compact structure with decreased bond angle [114, 115]. In addition, thermal spikes (local melting along the ion tracks and the subsequent rapid solidification and quenching) during ion irradiation also result in a decreased bond angle and a more compact silica structure through a transition from six-fold tetrahedra rings to three- and four-member rings during rapid solidification [114–116]. A combination of these two phenomena (thermal spikes and bond scission and atomic displacement) decreases the Si-O-Si bond angle and subsequently compacts the silica structure. The combination of these two mechanisms simulates a silica structure at elevated pressures. For comparison, the spectral center of the TO peak of the film heat-treated at 800 °C, in air is located at 1080 cm^{-1} (Fig. 4.6), corresponding to the Si-O-Si bond angle of 144°. The results of curve fitting of the FT-IR spectra of the films irradiated with 1 MeV Cu^+ are presented in Table 4.4.

Ion irradiation with 4 MeV Cu^{2+} does not induce any changes in the TO spectral center of the films after irradiation with a fluence of 10^{13} and 10^{14} ions/cm^2. However, after ion irradiation with a fluence of 10^{15} and 10^{16} ions/cm^2, a decrease in the peak position of the TO peak and elimination of the LO peak is observed. The TO peak spectral center in the FT-IR spectra of the film irradiated with a fluence of 10^{16} ions/cm^2 with 4 MeV Cu^{2+} ions shifts to 1015 cm^{-1}, corresponding to the bond angle of 124°, indicating a more compact silica structure. The small thickness of the films makes it difficult to observe reflection FT-IR spectra of the films irradiated with 4 MeV Cu^{2+} and 9 MeV Cu^{3+} ions with fluences of 10^{15} and 10^{16} ions/cm^2 and the reflection FT-IR spectra of these films are overwhelmed by a fringe pattern due to small thickness of the films and internal reflections [172].

After irradiation with 9 MeV Cu^{3+} with a fluence of 10^{15} and 10^{16} ions/cm^2, all the previously observed silica peaks disappear. The only visible peaks are a broad FT-IR peak between 600-900 cm^{-1} and a fringe background pattern. The background pattern originates from the small thickness of the films and internal reflections that gives rise to a wavy sinusoidal background pattern [172]. The broad peak between 600-900 cm^{-1} originates from the partial transformation of SiO_2 from tetrahedral to octahedral coordination. Williams and Jeanloz [173] studied the effects of pressure on the infrared spectra and structure of amorphous silica. They noted that with increasing

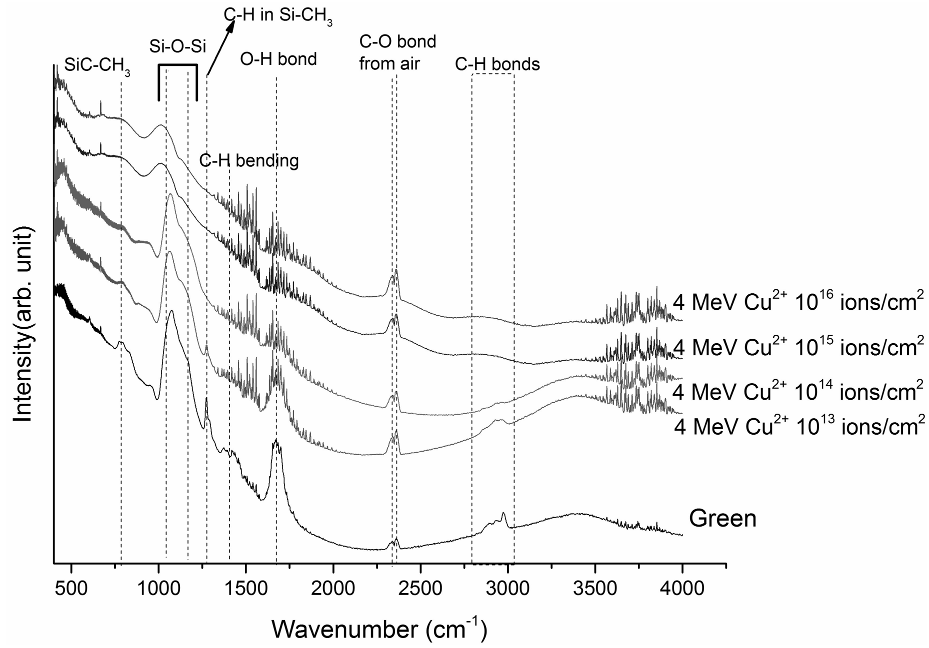

Figure 4.24: Transmission FT-IR spectra of the films irradiated with 4 MeV Cu^{2+} ions at different fluences.

Table 4.4: Curve fitting results of the FT-IR spectra of the films irradiated with 1 MeV Cu^{+} ions.

Film condition	TO peak center (cm^{-1})	Si-O-Si bond angle(°)	I(LO)/I(TO)	I(O-Si-C)/I(TO)
Green	1083	145	1.15	0
1 MeV Cu^{+} 10^{13} ions/cm^2	1075	143	1.22	0
1 MeV Cu^{+} 10^{14} ions/cm^2	1078	144	1.15	0
1 MeV Cu^{+} 10^{15} ions/cm^2	1061	139	0.24	0.54
1 MeV Cu^{+} 10^{16} ions/cm^2	1030	130	0.25	0.44

the pressure, the intensity of the SiO_4 related peaks around 1100 cm^{-1} is reduced significantly relative to the intensity of the new peaks between 600-900 cm^{-1}. Bending and stretching of the O-Si-O bond in octahedrally coordinated silicon (SiO_6) has peaks at the same region. Other studies have also noted that with increasing applied pressure, the SiO_4 peaks disappear and signs of additional SiO_6 related peaks are present in the infrared spectra [174, 175]. The transformation has been confirmed by both X-ray absorption [176] and Raman spectroscopy [177]. The shift from tetrahedral to octahedral coordination number is gradual [178–180], and so at the beginning of the increase in the coordination number, the FT-IR spectra of silica is defined by a broad featureless peak between 600-900 cm^{-1} and the absence of amorphous silica peaks between 900-1300 cm^{-1}. It should be noted that the broad featureless spectra originates from the small size of the octahedrally coordinated clusters [175]. It is also a feature of the FT-IR spectra of ion irradiated films that the small size of the compounds formed may render the well-defined peaks into broad featureless peaks [94]. The driving force behind coordination transformation as a result of applied pressure has been attributed to the structural changes in silica to enable compaction. As the pressure increases, there is a decrease in Si-O-Si bond angle through a decrease in the ring size of the silica from six to three or four. However, with further increase in pressure and a decrease in the bond angle, the coordination number changes to a more compact packing coordination, i.e., octahedral, to accommodate the high pressure [177]. Ion irradiation with energetic ions and the resulting bond scission and disorder and thermal spikes simulates the high level of pressure. Irradiation with 1 MeV Cu^{+} and 4 MeV Cu^{2+} decreases the bond angle, the same way that higher applied pressure results in smaller bond angle, and after ion irradiation with 9 MeV Cu^{3+}, the level of compaction forces a change in the coordination number of silica to accommodate the high density of the structure. Previous experimental [116, 181] and simulation [114, 115] studies of ion irradiated silica have confirmed that ion irradiation causes a decrease in Si-O-Si bond angle and a compaction of structure, similar to applied pressure. In addition, it was found that, regardless of compaction process (i.e., irradiation or applied pressure) structural and vibrational structure of silica after compaction is the same [115, 116, 181]. This indicates that the previous findings on the vibrational response of silica under applied pressure can be applied to ion irradiated films as well.

In order to test this hypothesis, low wavenumber Raman spectroscopy was performed on the films to study the Raman response of the silica structure. Figure 4.27 shows the Raman spectra of the films in the 200-900 cm^{-1} range after ion irradiation with all three ions at a fluence of 10^{16} ions/cm^2. The main two observable Raman modes are located at approximately 450 and 720 cm^{-1}, corresponding to the ω_1 Raman mode of amorphous silica, and carbon incorporated amorphous silica [182],

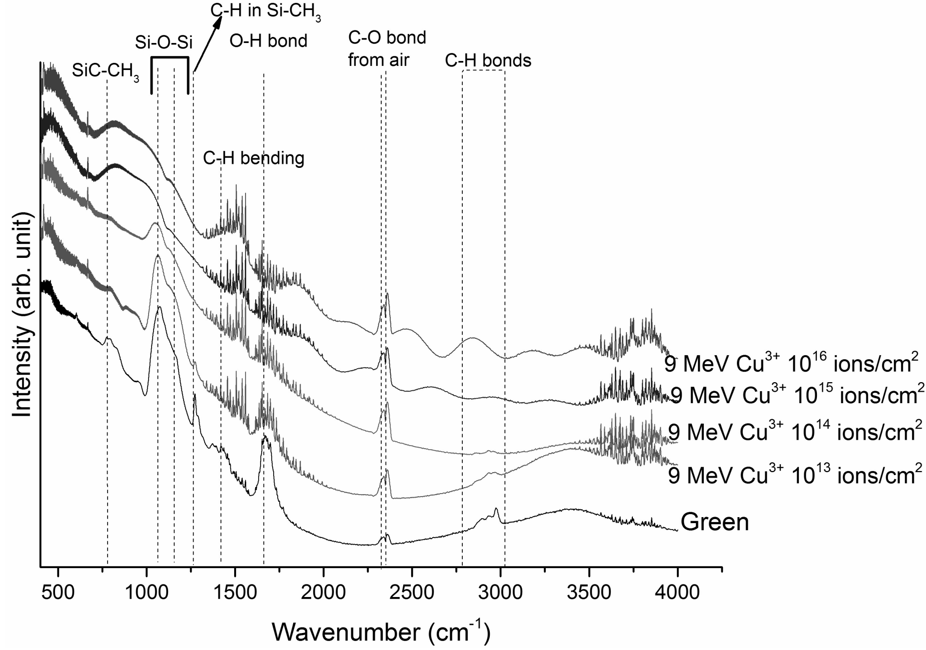

Figure 4.25: Transmission FT-IR spectra of the films irradiated with the 9 MeV Cu^{3+} ions at different fluences.

respectively. With increasing ion energy and irradiation fluence, there is an increase in the spectral center of the ω_1 mode up to 490 cm^{-1} for the 9 MeV Cu^{3+} irradiated film at a fluence of 10^{16} ions/cm^2. In addition, the 720 cm^{-1} mode disappears after irradiation with 9 MeV Cu^{3+} ions with a fluence of 10^{16}. The increase in the spectral center of the ω_1 mode is consistent with previous high pressure Raman studies of silica [177, 183] and is related to the decrease in the Si-O-Si bond angle and the formation of three and four fold tetrahedra rings. The disappearance of the Raman mode at 720 cm^{-1} after irradiation with higher energy ions is related to the changes in the coordination of silicon in amorphous silica, as the presence of different coordinations and silicon sites results in the broadening of the Raman modes and loss of intensity [173]. In addition, the changes in coordination number may induce a decrease in the polarizability of the ions and a decrease in Raman intensity [173]. The Raman results confirm FT-IR results that the silica structure formed after ion irradiation is similar to the silica structure after the application of high pressure. For comparison, the Raman spectra of fused silica glass and heat-treated films are presented in Appendix C.

Raman results confirm the presence of a silica network within the films, even after irradiation at fluences and energies that do not result in the presence of silica-related FT-IR peaks between 900-1300 cm^{-1}. In addition, the results also confirm a gradual transition toward a more compact silica structure with increasing ion energy and fluence.

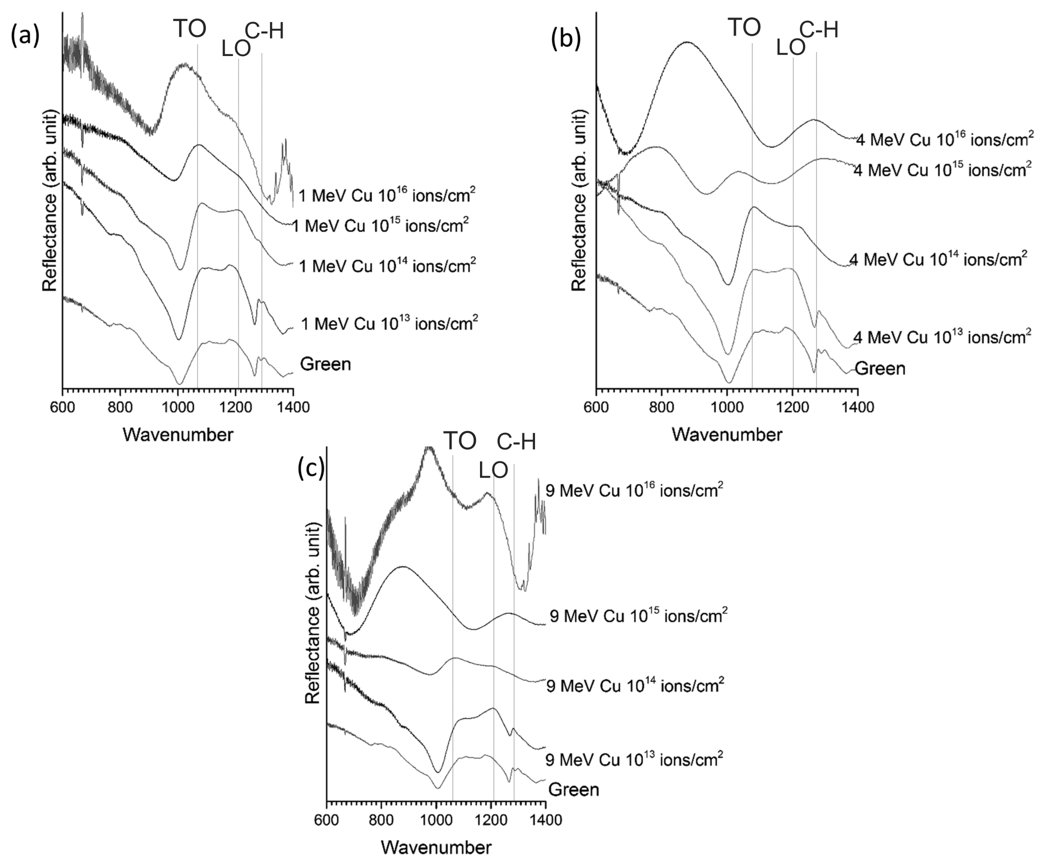

Figure 4.26: Reflection FT-IR spectra of the 1 MeV Cu^{+}, 4 MeV Cu^{2+}, and 9 MeV Cu^{3+} irradiated films at different fluences. The FT-IR spectra of 4 MeV Cu^{2+}, and 9 MeV Cu^{3+} irradiated films with fluences of 10^{15} ions/cm^2 and 10^{16} ions/cm^2 is overwhelmed by a fringe pattern.

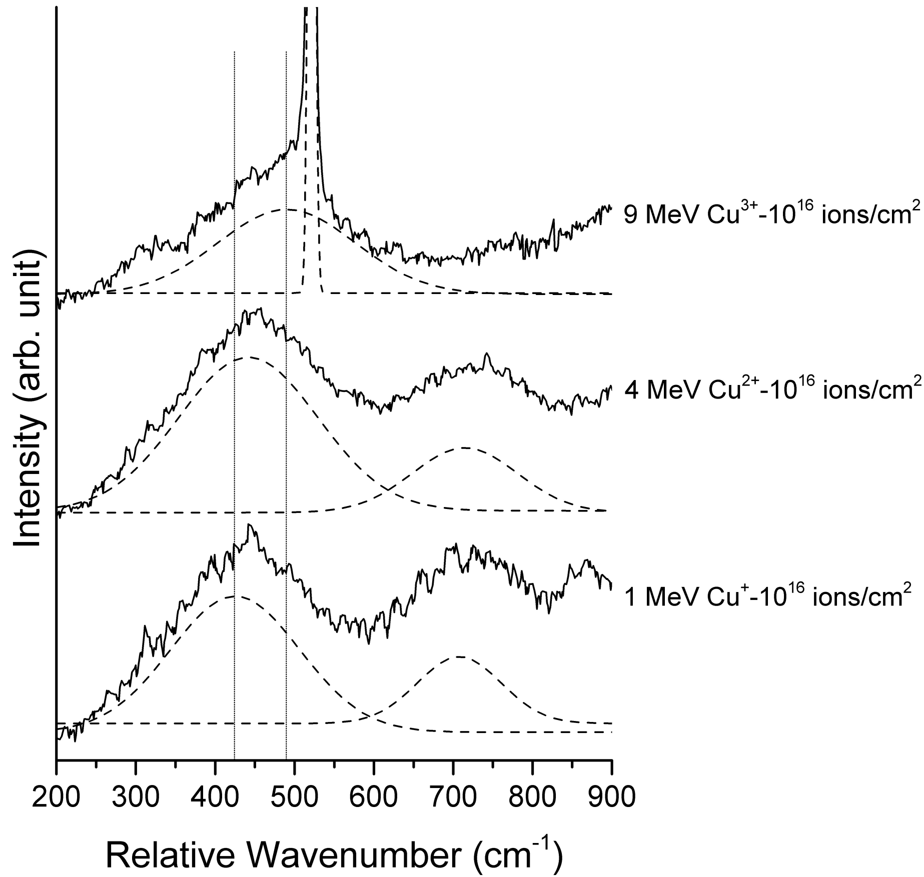

Figure 4.27: Raman spectra of the collected (solid line) and fitted (dashed line) silica Raman modes of ion irradiated films with 1 MeV Cu^{+}, 4 MeV Cu^{2+}, and 9 MeV Cu^{3+} ions. The vertical lines indicate lowest and highest center of the ω_1 Raman mode. The sharp Raman mode at 520 cm^{-1} is related to silicon substrate.

4.3.3 Raman spectroscopy characterization of free carbon clusters

Raman spectroscopy results for the characterization of free carbon clusters are presented in Figs. 4.28, 4.29, and 4.30 for films irradiated with 1 MeV Cu^{+}, 4 MeV Cu^{2+}, and 9 MeV Cu^{3+} ions, respectively. The Raman response of the films irradiated with 1 MeV Cu^{+} is similar to the films irradiated with H^{+} and N^{2+} ions. After irradiation at low fluences (10^{13} and 10^{14} ions/cm^2) no sign of any carbon related Raman modes is observed. The broad background emission after irradiation with 1 MeV Cu^{+} with a fluence of 10^{14} ions/cm^2 is possibly related to intermediate organic compounds. After irradiation at higher fluences (10^{15} and 10^{16} ions/cm^2) signature carbon related D and G modes are observed. The free carbon formed during ion irradiation with 1 MeV Cu^{+} was studied by curve fitting its Raman response. Two Gaussian peaks are used for the D and G Raman modes. A summary of the

results are presented in Table 4.5. The free carbon formed in the film irradiated with a fluence of 10^{15} ions/cm^2 is amorphous sp^2 bonded carbon. The background in the Raman spectra of the film irradiated at 10^{15} ions/cm^2 with 1 MeV Cu^+ ions originates from an electron hole pair recombination within sp^2 bonded clusters and the intensity of this emission tends to increase with increasing the hydrogen concentration, primarily due to the saturation of non-radiative recombination sites (i.e., dangling bonds) by hydrogen [120,127]. Based on the approach described in Sections 2.4.1 and 4.2.3, after irradiation with a fluence of 10^{16} ions/cm^2, the free carbon is amorphous and only a limited concentration of sp^3 bonded carbon may be present. The lower intensity ratio (I(D)/I(G)) and large peak width of the G mode after irradiation at this fluence indicates a higher level of defects than the films irradiated with light ions. The average carbon cluster size is estimated from Equation 4.1 to be 1.2 nm.

The Raman response of the ion irradiated films with 4 MeV Cu^{2+} and 9 MeV Cu^{3+} is different from 1 MeV Cu^+, H^+, and N^{2+} irradiated films. The films irradiated with 4 MeV Cu^{2+} and 9 MeV Cu^{3+} exhibit no visible Raman response after ion irradiation with a fluence of 10^{13} ions/cm^2. No visible Raman mode is observed after ion irradiation with 4 MeV Cu^{2+} with a fluence of 10^{14} ions/cm^2. After ion irradiation with 9 MeV Cu^{3+} ions with a fluence of 10^{14} ions/cm^2 some evidence of carbon related Raman modes is observed between 1100-1700 cm^{-1}. However, the Raman modes are too weak to draw a conclusion. After irradiation with 10^{15} and 10^{16} ions/cm^2 fluences, a single Raman mode centered at 1430 cm^{-1} is present in the films irradiated with 4 MeV Cu^{2+} and 9 MeV Cu^{3+}. This Raman mode cannot be deconvoluted to the D and G modes and is a different mode. Although the carbon Raman response almost always consists of D and G modes (with the exception of pure diamond, where the Raman response is a single mode at 1332 cm^{-1}), there are rare cases where the carbon Raman response is a single mode centered around 1430 cm^{-1} instead of the D and G modes [184–192]. This peak is usually observed in silicon carbide [184, 186, 188, 191, 192] or Ge_xC_{1-x} [185, 187, 189, 190] compounds. All the specimens exhibiting the 1430 cm^{-1} Raman mode were either ion irradiated or sputtered. Therefore, this Raman mode has only been observed in defective carbon structures. The Raman mode was first observed by Gorman and Solin, in amorphous silicon carbide [188]. It was concluded that the Raman mode is not related to impurities or oxygen containing compounds. This study was performed in a silicon carbide compound with carbon deficiency and the occurrence of the 1430 cm^{-1} Raman mode was always accompanied by the formation of Si-Si bonds, and so the study concluded that the Raman mode was related to a C-C bond. Based on the dependence of the peak position on carbon content and Monte Carlo simulations, other studies have also confirmed that this mode is a result of a homonuclear carbon

bond [184].

The fact that this Raman mode originates from carbon bonds in disordered and amorphous compounds is generally accepted. However, there is no agreement about the nature of the C-C bond. Different studies have suggested that the Raman mode is either from sp^2 or sp^3 bonded carbon. The lack of the D and G modes was used by some to suggest that this mode is related to sp^3 bonded carbon [185, 190]. However, this is a questionable conclusion. All materials systems with a Raman mode at 1430 cm^{-1} are amorphous, and it has consistently been shown that the Raman response of amorphous sp^3 bonded carbon, with a limited content of sp^2 bonded carbon, may also consist of D and G Raman modes. In addition, no sign of sp^3 bonded carbon Raman modes is observed in the Raman spectra. Others have claimed that the peak is related to amorphous carbon [187] which again is questionable since the D and G modes are not indicators of the carbon crystallinity and are also present in the Raman response of amorphous carbon. Other authors have suggested that the Raman mode is a result of sp^2 bonded carbon, but that the carbon is not in the form of graphitic rings [189]. It has been suggested that even though this Raman mode originates from sp^2 bonded carbon, no graphitic rings are present. No sp^3 bonded carbon Raman mode is expected at wavenumbers higher than 1400 cm^{-1} [193], which further confirms the sp^2 bonded origin of the observed Raman mode. Some studies have shown that subsequent annealing transforms this carbon structure into graphitic carbon [186, 190, 192].

There also exists a number of theoretical studies of the Raman spectra of non-graphitic sp^2 bonded amorphous carbon which might explain the origin of the observed Raman mode in the ion irradiated films. Doyle and Dennison used a theoretical approach called the embedded-ring approach (ERA) to calculate the Raman spectra of various graphitic rings [194]. This approach combines the vibrational modes of n-member rings to predict the vibrational spectra of an amorphous random network. The study indicated that the A'_{1g} vibrational mode of a five-member ring generates a Raman mode at 1444 cm^{-1}. Tarrant et. al., also used first principles density functional theory (DFT) calculations and discovered that this Raman mode may have originated from either five- or seven-member sp^2 bonded rings or the aggregation of linearly aggregated six-member graphitic rings [195]. However, linearly aggregated graphitic rings are always accompanied by D and G modes. Since no additional D and G modes are observed in the present study, this mode does not originate from linearly aggregated graphitic rings. XPS results also confirm the sp^2 bonded nature of the carbon within the films in the present study, as will be discussed in Section 4.3.4.

In summary, the Raman spectroscopy results indicate that the free carbon structure after ion irradiation with 1 MeV Cu^+ ions consists of defective graphitic rings. Raman spectroscopy also

shows that the structure of the free carbon clusters after ion irradiation with 4 MeV Cu^{2+} and 9 MeV Cu^{3+} consists of sp^2 bonded carbon in a configuration other than graphitic rings, and has possibly a five-ring or seven-ring structure.

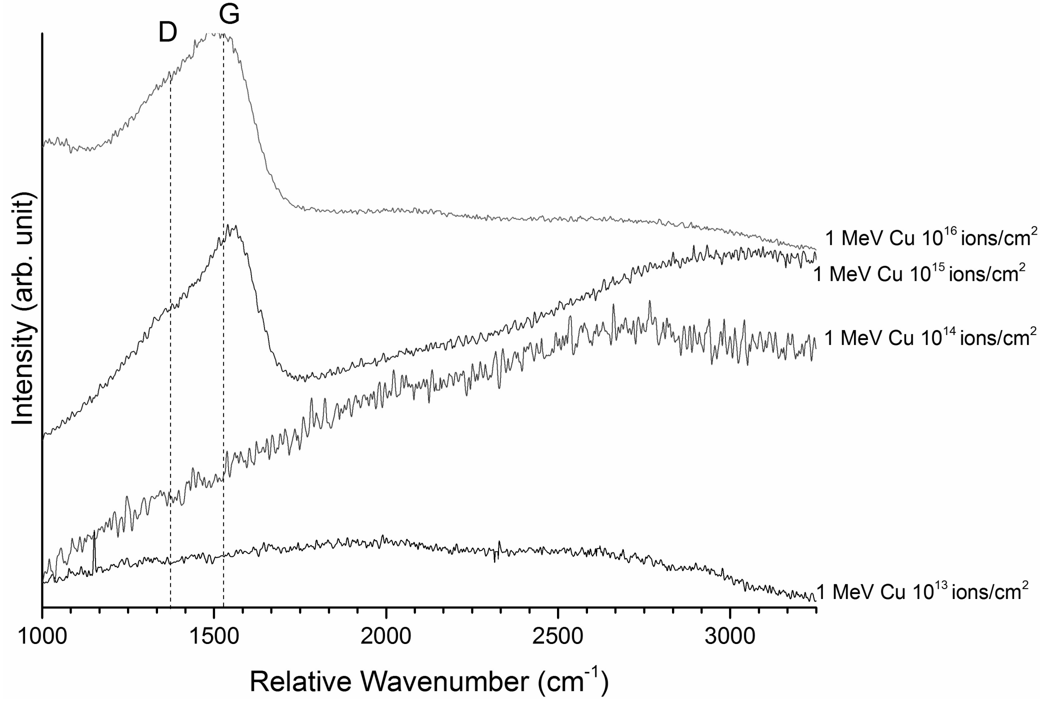

Figure 4.28: Raman spectra of the 1 MeV Cu^+ ion irradiated films at different fluences.

Table 4.5: Curve fitting results of the Raman spectra of 1 MeV Cu^+ irradiated films exhibiting carbon related D and G Raman modes.

Film condition	W(G) (cm^{-1})	FWHM(G) (cm^{-1})	I(D)/I(G)
1 MeV Cu^+-10^{15} ions/cm^2	1556	144	0.9
1 MeV Cu^+-10^{16} ions/cm^2	1518	195	0.85

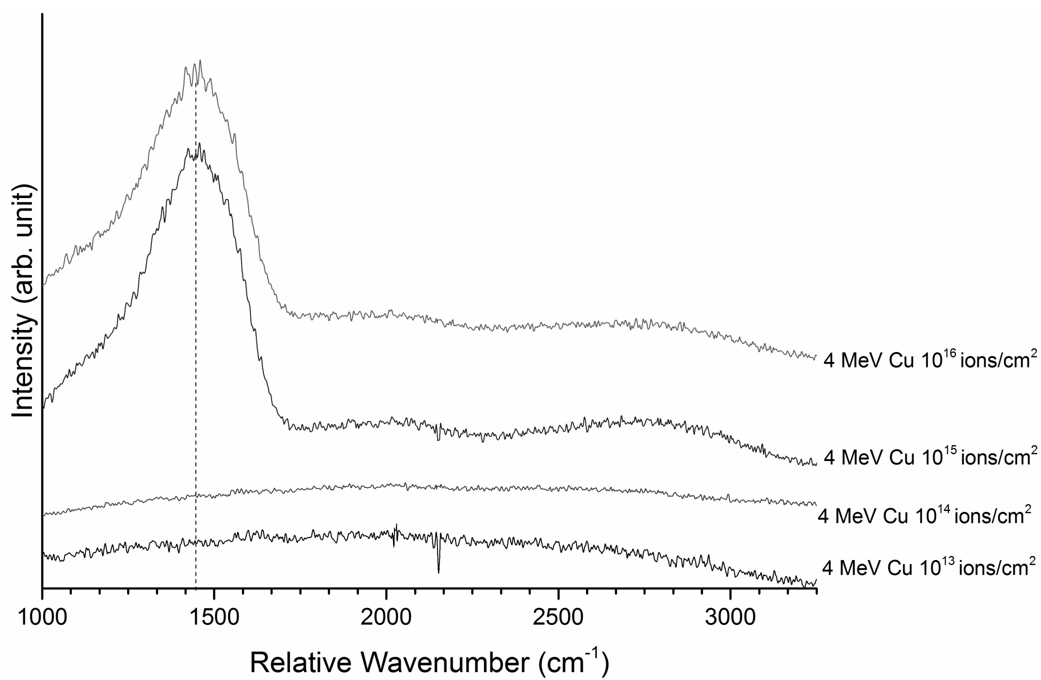

Figure 4.29: Raman spectra of the 4 MeV Cu^{2+} ion irradiated films at different fluences.

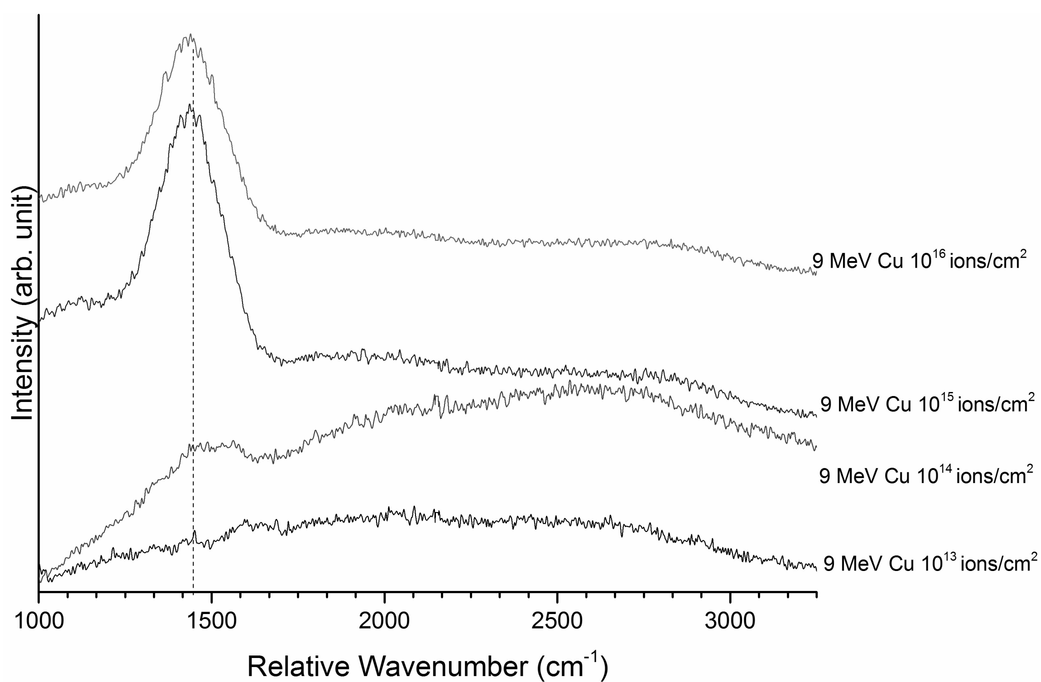

Figure 4.30: Raman spectra of the 9 MeV Cu^{3+} ion irradiated films at different fluences.

4.3.4 XPS characterization of the films irradiated with heavy ions

Figure 4.31 shows the XPS Si 2p spectra of two films irradiated with heavy ions. Similar to what was discussed in Section 4.2.4, with increasing ion energy and fluence, there is a decrease in the binding energy of the Si 2p peak. Although this shift may be related to the incorporation of carbon within the silica structure, it should be noted that the shift after ion irradiation with 9 MeV Cu^{3+} with a fluence of 10^{16} ions/cm^2 is, at least partially, related to the formation of octahedrally coordinated silica. Previous studies on the effect of phase transformations on the XPS spectra of silica have shown a decrease in the binding energy of silicon after tetrahedral to octahedral transformation. The reason for the decrease in the binding energy is the higher extra-atomic relaxation energy of octahedrally coordinated silica compared to tetrahedrally coordinated structure [196, 197].

Figure 4.32 exhibits the measured Si 2p spectra of the films irradiated with 9 MeV Cu^{3+} ions with a fluence of 10^{16}, 4 MeV Cu^{3+} ions with a fluence of 10^{15}, and N^{2+} ions with a fluence of 5×10^{15} ions/cm^2. In addition, the spectrum of the heat-treated film is also included. There is a monotonic decrease in the Si 2p binding energy with increasing ion energy and fluence which is an indication of carbon incorporation within the silica structure. It should be noted that the Si 2p peak of SiC (located at 100.3 eV [129, 130, 132]) is not observed in any of the films.

Figure 4.33 shows the C 1s XPS spectra of the films after ion irradiation with heavy ions. For comparison, the XPS spectrum of the heat-treated film is also included. The results indicate the presence of a C-C peak after ion irradiation. The shoulder on the higher binding energy side of the main peak consists of a C=O peak at approximately 286 eV and a C-O peak at 287-290 eV [136]. The location of these peaks on the shoulder are indicated in Appendix A.

In order to study the nature of free carbon formed after ion irradiation, the C 1s XPS spectra of the 9 MeV Cu^{3+} irradiated film after ion irradiation with a fluence of 10^{16} ions/cm^2 and N^{2+} irradiated film with a fluence of $5{\times}10^{15}$ ions/cm^2 are compared and the results are presented in Fig. 4.34. Figure 4.34 shows that the nature of carbon in the 9 MeV Cu^{3+} irradiated film is similar to the N^{2+} irradiated film, which as discussed in Section 4.2.3, is predominantly sp^2 bonded. The only difference between the XPS C1s spectra of two films is the asymmetric broadening in the C 1s spectra of the film irradiated with 9 MeV Cu^{3+} ions. The binding energy of the XPS C 1s spectra of sp^2 bonded and sp^3 bonded peaks are located at 284.4 eV and 285.3 eV, respectively [135,198] and are indicated in Fig. 4.34. Curve fitting is performed using three 30% Lorentzian-70% Gaussian peaks for C-C, C=O, and C-O bonds. The fitted curves are presented in Appendix A. The results indicate

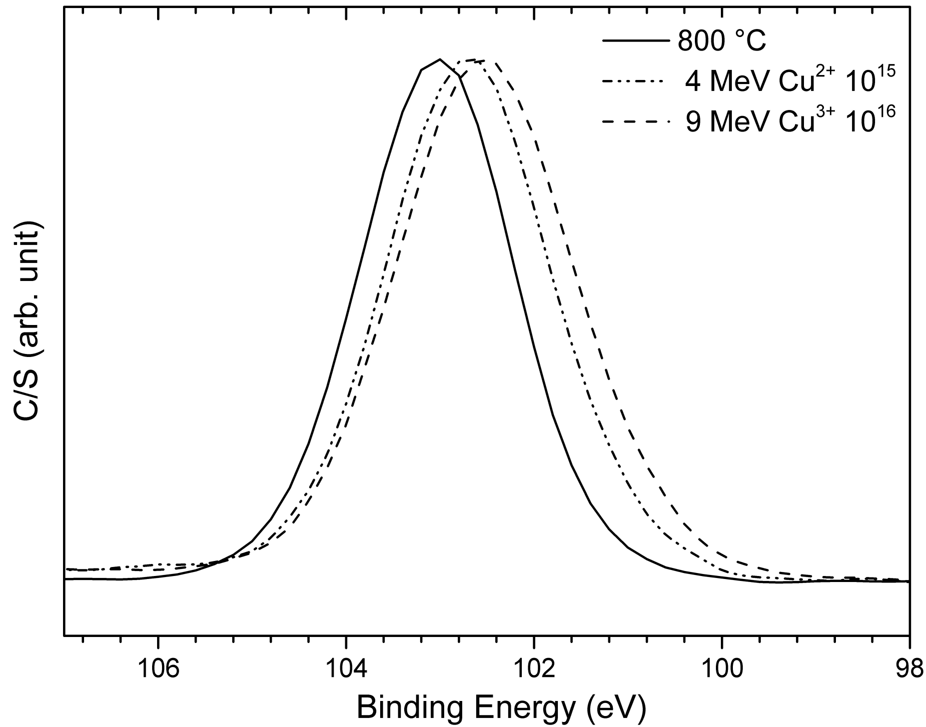

Figure 4.31: The XPS Si 2p spectra after irradiation with heavy ions. For comparison, the XPS spectra of heat-treated film is also included.

that the C 1s spectra of both films is located at 284.4 eV. The peak width of the film irradiated with 9 MeV Cu^{3+} ions is 1.9 eV, which is larger than the peak width of the N^{2+} irradiated film (1.6 eV). The asymmetric broadening of the C 1s line after ion irradiation with 9 MeV Cu^{3+} may be related to the incorporation of carbon within silica and the formation of carbon rich SiO_xC_y tetrahedra, as the C 1s spectra of a carbon atom incorporated within a silica network is located at 283.6 eV [199–201]. The binding energy of the C 1s spectra for both films indicates that the carbon formed after ion irradiation with both ion species is sp^2 bonded. The C 1s XPS spectra of the irradiated films confirm the Raman spectroscopy results that the free carbon clusters are predominantly sp^2 bonded.

In addition, XPS spectroscopy can be utilized to study the chemical composition of the films. Figure 4.35 shows the overall XPS spectra of the ion irradiated and heat-treated films. However, due to the small photoionization cross-section of hydrogen, it is not possible to detect hydrogen with XPS [202]. In addition, the chemical compositions obtained from XPS and ERD/RBS would be different, as ERD/RBS probes the whole thickness of the films but XPS is limited to a few nanometers from the surface. As the stopping powers during ion irradiation vary along the thickness of the films, variations in the chemical composition of the films along the thickness are expected. However, the same trend in changes of the chemical compositions obtained by XPS and ERD/RBS

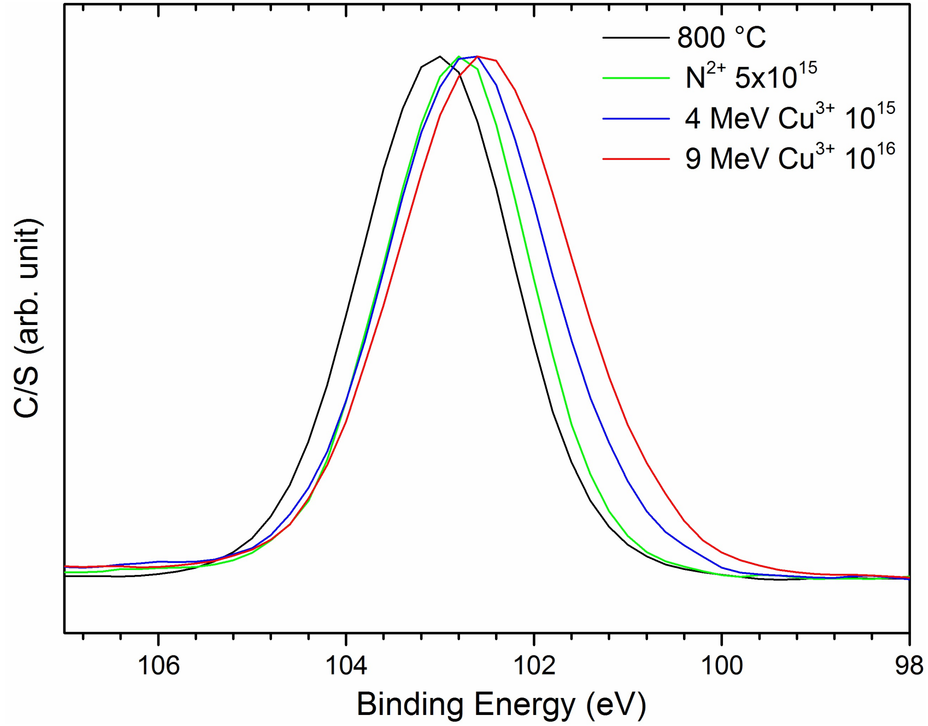

Figure 4.32: The XPS Si 2p spectra of heat-treated, light-ion irradiated and heavy-ion irradiated films. A shift toward lower binding energies with increasing ion energies can be observed.

should exist.

As XPS is a quantitative technique, the areas of the O 1s peak, Si 2p peak, and C 1s peak can be utilized to measure the chemical composition of the films. The observed fluorine peak most likely originates from surface contamination from the specimen containers. After background removal, the peak areas are utilized to estimate the chemical composition of the films. Prior to the calculation of composition, peak areas are normalized according to the XPS sensitivity factors of different elements. The concentration of element A is calculated using the following equation:

$$C_A = \frac{I_A/S_A}{\sum_{i=1}^{n} I_i/S_i} \tag{4.5}$$

where I_A and S_A are the peak area and sensitivity factor of element A, respectively. I_i and S_i are the peak area and sensitivity factor of the i-th element, respectively. C_A is the mole fraction of element A. The sensitivity factors for O 1s, C 1s, and Si 2p are 0.66, 0.25, and 0.27, respectively [203]. Table 4.6 shows the chemical composition of the films as measured by XPS and ERD/RBS.

The XPS results are in agreement with the ERD/RBS derived chemical composition. While the exact composition is different from the ERD/RBS results, the trends in changes of chemical

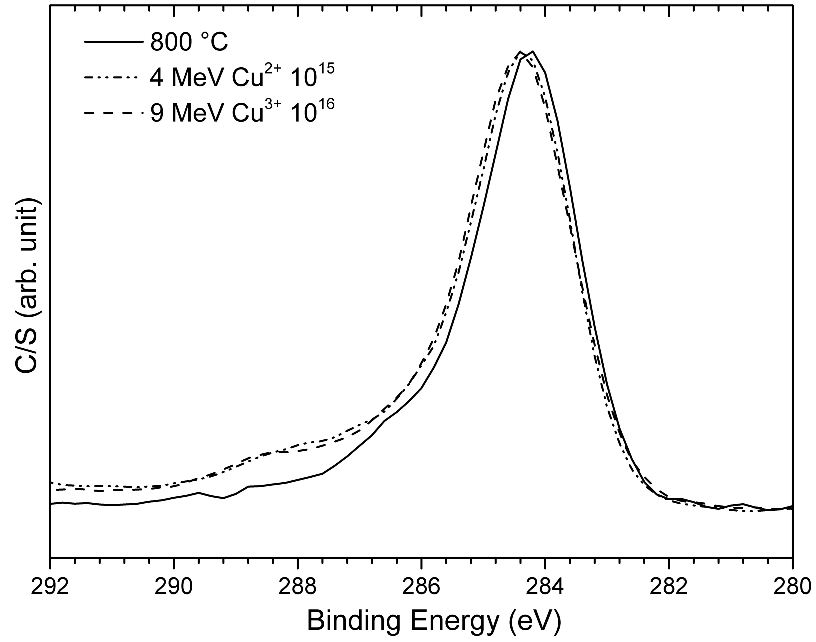

Figure 4.33: XPS C 1s spectra of the films irradiated with heavy ions.

Table 4.6: XPS and ERD/RBS measured chemical composition of the films

Conversion conditions	Chemical composition (XPS)	Chemical composition (ERD/RBS)
N^{2+} 10^{13} ions/cm^2	$SiO_{2.1}C_{6.9}$	$SiO_{2.64}C_{3.7}$
N^{2+} 5×10^{15} ions/cm^2	$SiO_2C_{2.9}$	$SiO_{2.5}C_{3.09}$
4 MeV $Cu^{2+}10^{15}$ ions/cm^2	$SiO_{1.75}C_{2.25}$	$SiO_{1.17}C_{1.13}$
9 MeV Cu^{3+} 10^{16} ions/cm^2	$SiO_{1.5}C_{1.95}$	$SiO_{0.8}C_{0.78}$

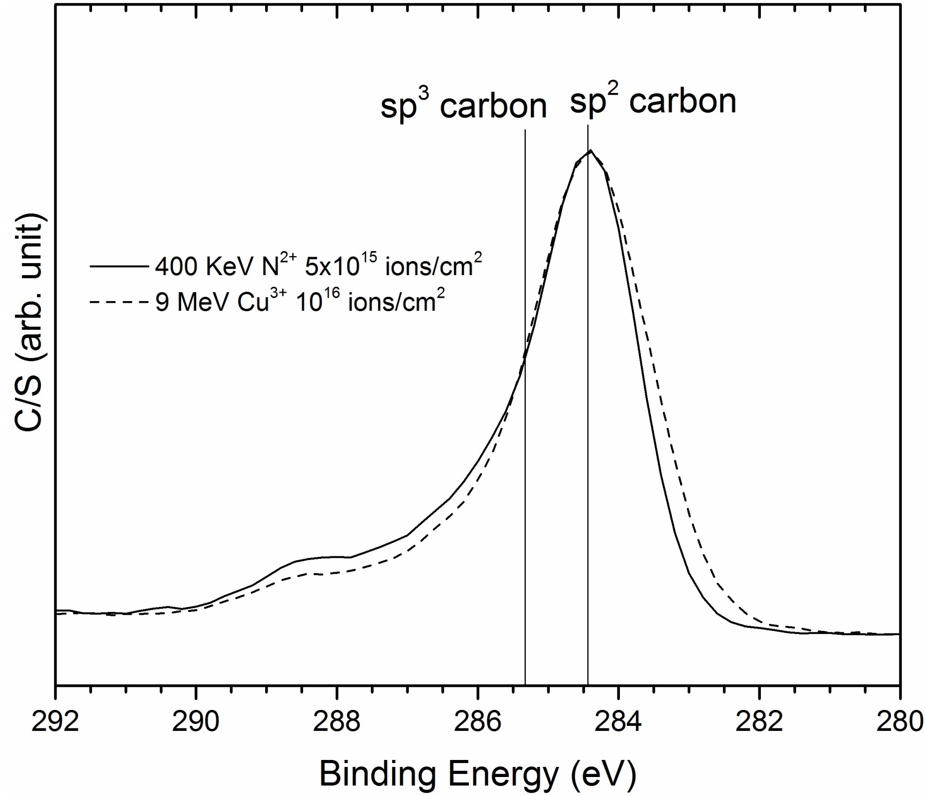

Figure 4.34: XPS C 1s spectra of 9 MeV Cu^{3+} irradiated film with a fluence of 10^{16} ions/cm^2 and N^{2+} irradiated film with a fluence of 5×10^{15} ions/cm^2. The vertical lines indicate the binding energy of sp^2 bonded and sp^3 bonded carbon.

composition is similar to the ERD/RBS results where light ion irradiated films only exhibit carbon loss and ion irradiation with heavy ions leads to both carbon and oxygen loss. The XPS results confirm and complement the ERD/RBS results.

The O 1s XPS spectra of the films after ion irradiation was also collected, but the differences between the spectra of the films are not large enough to draw a conclusion. A small shift towards lower binding energies in the O 1s spectra of the 4 MeV Cu^{2+} and 9 MeV Cu^{3+} irradiated films in comparison to the heat-treated films is observed that can be related to changes in bond angle of the Si-O-Si bonds [137]. In addition, the partial transformation from tetrahedral to octahedral coordination in silica can lower the binding energy of the O 1s core level spectra as well [196, 197]. The O 1s spectra of the films show a decrease in the binding energy, but the shifts are not large enough to make a conclusion. The XPS O 1s spectra of the films irradiated with heavy ions are presented in Appendix B. XPS spectroscopy has also been used to estimate the ratio of free carbon (i.e., carbon that is bonded to other carbon atoms) to bonded carbon (i.e., carbon that is bonded

to silicon atoms) in the heat-treated SiOC. This approach and the following results are presented in Appendix D. However, this approach assumes a near-stoichiometric composition of the constituent phases and applying the method to the current study results in inaccurate results.

4.3.5 Microstructural configuration of the films after ion irradiation with heavy ions

It is shown that irradiation with heavy ions imposes disorder to the films up to the point that the Si-O-Si FT-IR peaks, and the Raman D and G modes disappear due to the destruction of graphitic structure and a transformation of silica from tetrahedrally bonded to octahedrally bonded structure. However, even at this level of disorder, heterogeneity still exists and the microstructure is composed of separate amorphous silica and carbon phases. Figure 4.36 shows the predicted final phases present in the films for different compositions. The chemical triangle model was developed for the heat-treated films and its prediction is not consistent with the findings in this study. The model predicts that the composition of phases after irradiation with all three ions with the highest fluence results in the formation of SiC along with amorphous carbon and silica. However, no sign of SiC is observed in the Raman, FT-IR, and XPS spectra of the films. This is another indication of the differences between the heat-treated and ion irradiated films.

It should be noted that the room temperature and low temperature photoluminescence spectra of 1 MeV Cu^+ and 9 MeV Cu^{3+} films irradiated with a fluence of 10^{16} ions/cm^2 was also investigated from room temperature down to 10 K, but no emission relating to SiC (a broad peak ranging from 400-900 nm, as observed previously in the literature [204, 205] for SiC within an ion irradiated SiOC film) is observed. The photoluminescence spectra are presented in Appendix E. The results in Fig. 4.36 indicate that, unlike heat-treated films, the final phase composition of the films can not be predicted solely based on the chemical composition.

It is suggested in Section 4.2.5 that high energy ion irradiation in some cases might lead to the formation of an interconnected carbon network. The Raman response of the films after ion irradiation with heavy ions is found to be non-graphitic sp^2 bonded carbon and there exists no indication of the continuity of carbon clusters. The microstructure of the films consists of compacted amorphous silica with a broad distribution of bond angle along with separate clusters of sp^2 bonded carbon embedded within the matrix.

A schematic of the proposed microstructure of ion irradiated films is shown in Fig. 4.37. The structure of the films after ion irradiation at the highest fluence with 1 MeV Cu^+ ions (Fig. 4.37 (a))

consists of a compacted, tetrahedrally bonded, and carbon incorporated amorphous silica network with average bond angle of 130°. In addition, isolated clusters of highly defective graphitic carbon are also present as a secondary phase within the films. The interface of silica and carbon is composed of carbon-rich SiO_xC_y tetrahedra. The microstructure of the film irradiated with 4 MeV Cu^{2+} ions at the highest fluence is presented in Fig. 4.37 (b). The results indicate that the film is composed of a compact amorphous silica structure along with isolated carbon clusters. The average Si-O-Si bond angle of the silica phase was estimated to be 124°. The carbon clusters are sp^2 bonded carbon, arranged in a configuration other than graphitic six-fold rings, possibly five or seven member rings. The microstructure of the film irradiated with 9 MeV Cu^{3+} ions at the highest fluence is presented in Figure 4.37 (c). The structure is composed of amorphous silica and isolated carbon clusters. The amorphous silica structure is a combination of tetrahedrally and octahedrally bonded silica. The carbon structure after irradiation with 9 MeV Cu^{3+} ions is sp^2 bonded carbon, possibly arranged in five or seven rings. The concentration of carbon-rich SiO_xC_y tetrahedra in this film is also higher than other films.

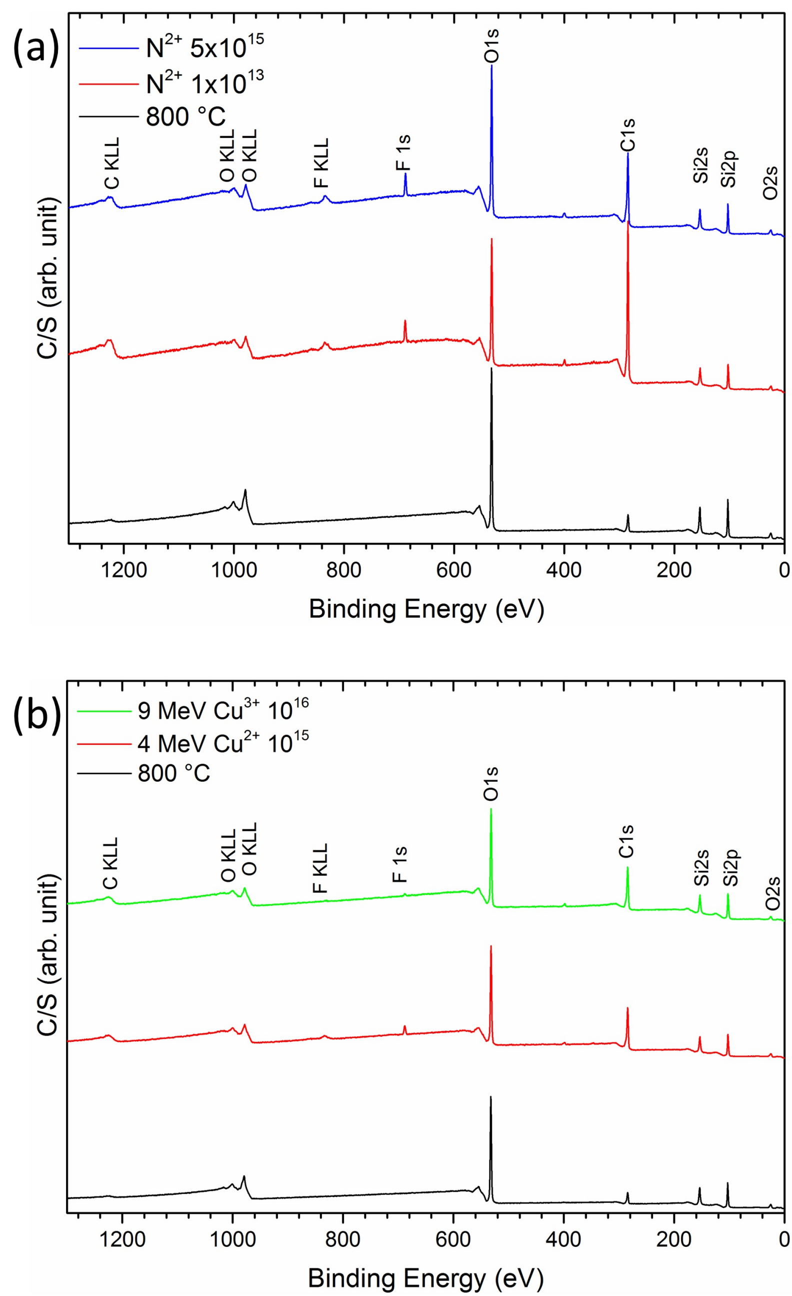

Figure 4.35: XPS spectra of the films ion irradiated with both light and heavy ions. The heat-treated film spectrum is also plotted for comparison.

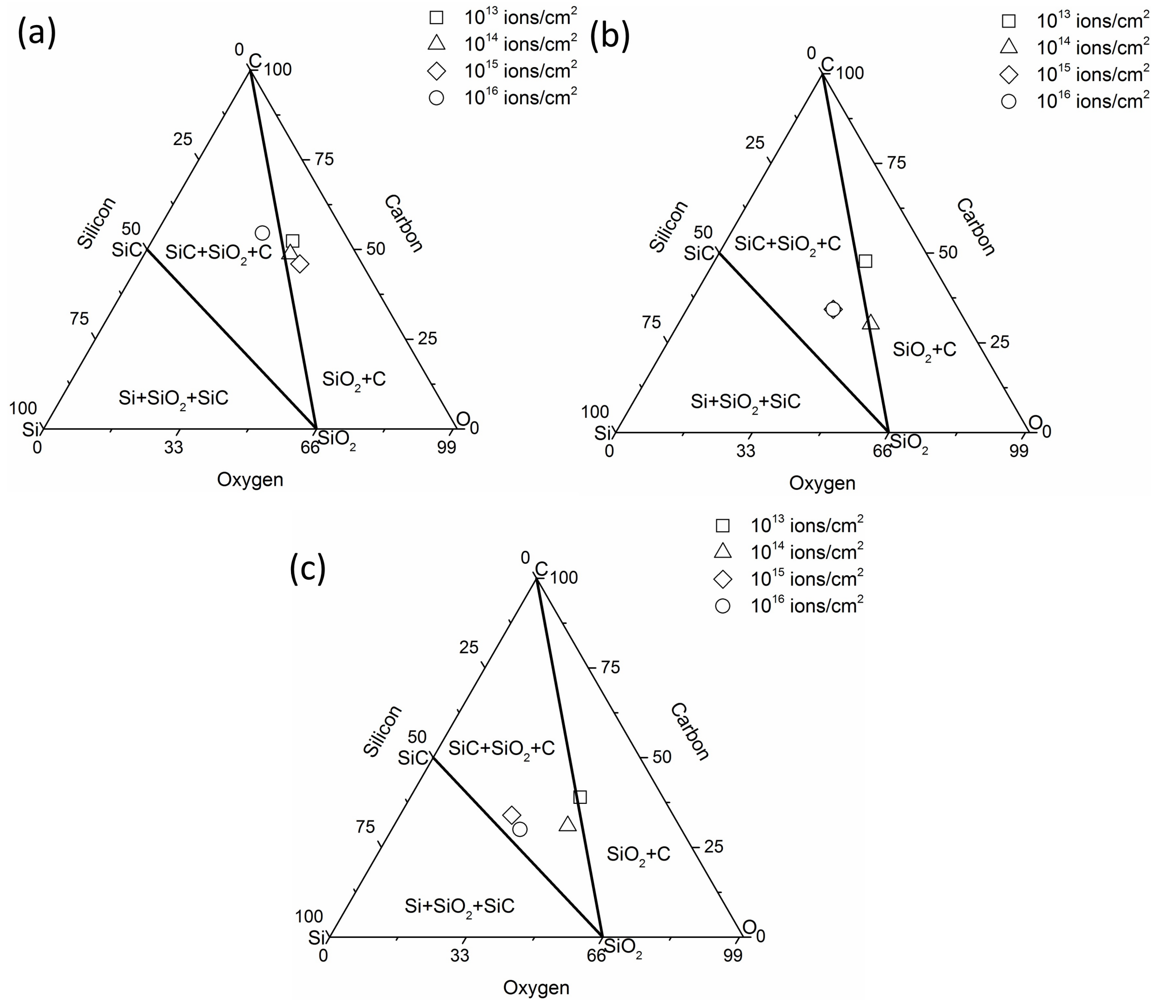

Figure 4.36: Chemical composition triangle of films irradiated with a) 1 MeV Cu^{+} b) 4 MeV Cu^{2+}, and c) 9 MeV Cu^{3+}, predicting the final phases present within the ion-irradiated films based on a model developed for heat-treated films.

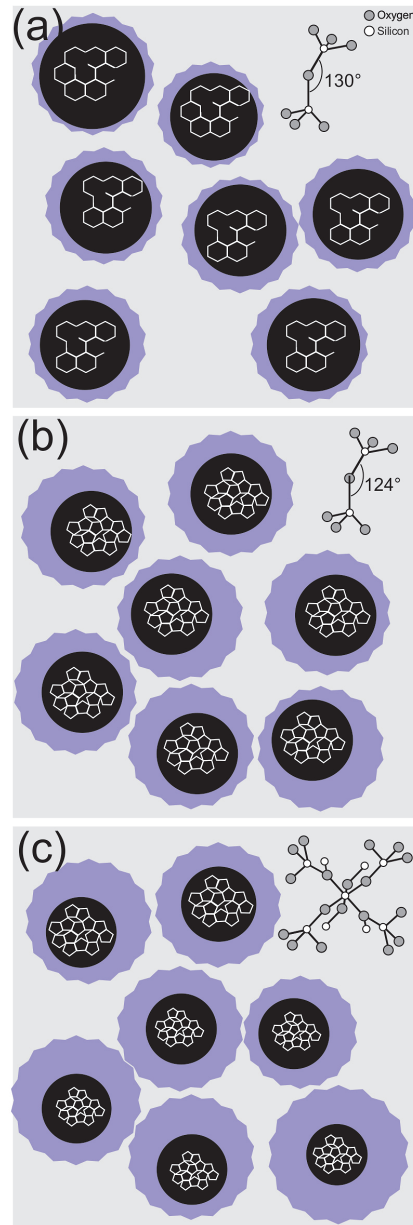

Figure 4.37: Microstructural configuration of films irradiated with different ion energies after irradiation with a fluence of 10^{16} ions/cm^2, a) 1 MeV Cu^{+}, b) 4 MeV Cu^{2+}, and c) 9 MeV Cu^{3+}.

4.3.6 Mechanical properties of the films after ion irradiation with heavy ions

Figure 4.38 shows the variations in the film thickness, reduced elastic modulus, and hardness of the ion irradiated films. There is an increase in both hardness and reduced elastic modulus, as well as a decrease in the films thickness with increasing fluence for all ion energies. Based on Equation 4.4 and assuming a Poisson's ratio of 0.25 for the films, the elastic modulus of the 1 MeV Cu^{+}, 4 MeV Cu^{2+}, and 9 MeV Cu^{3+} irradiated films with a fluence of 10^{16} ions/cm^2 is estimated to be 93 GPa, 118 GPa, and 147 GPa, respectively.

After irradiation with a fluence of 10^{16} ions/cm^2 with 1 MeV Cu^{+}, the elastic modulus and hardness of the film are higher than for fused silica (72.5 GPa and 7.6 for fused silica [150] versus 93 GPa and 8.3 GPa). The elastic modulus and hardness of the film irradiated with a fluence of 10^{16} ions/cm^2 with 4 MeV Cu^{2+} is also higher than for fused silica (118 GPa and 9.9 GPa). After ion irradiation with 9 MeV Cu^{3+}, the elastic modulus and hardness of the film irradiated with fluences of 10^{15} and 10^{16} ions/cm^2 are almost twice as that for fused silica (147 GPa and 11.6 GPa). The values are also well above the reported values for heat-treated SiOC (8 GPa for hardness and 50-113 GPa for elastic modulus [13, 27]).

Previous studies on the mechanical response of ion irradiated silicon oxycarbide thin films have shown similar behaviors. The increase in the mechanical properties of the ion irradiated films was related to the formation of either sp^3 bonded carbon or SiC [24, 25, 82]. Considering that the secondary phase within the films is sp^2 bonded carbon and no sign of SiC is observed in the XPS, FT-IR, and Raman spectra of the films, other structural changes which have occurred during ion irradiation should be considered as the source of increase in the elastic modulus of the films.

The decrease in the Si-O-Si bond angle of the silica during ion irradiation, in combination with the elastic deformation mechanism of amorphous silica, can explain the increase in the elastic modulus during ion irradiation. As discussed in Section 4.2.6, in addition to elastic deformation by changes in the bond length, the presence of free volume in the amorphous silica structure leads to an alternative elastic deformation mechanism. This alternative method can elastically deform the material at lower forces than pure bond length change. As bond angle decreases as a result of ion irradiation, a higher proportion of stress is applied for pure bond length change, which leads to a higher elastic modulus. The dependence of the elastic modulus of the films to the Si-O-Si bond angle has been shown both experimentally [146] and by molecular dynamics simulations [57]. The level of enhancement depends

on the Si-O-Si bond angle and the resulting compaction. Previous studies have predicted the elastic modulus and Si-O-Si bond angle of silica under different pressures [57]. Based on the Si-O-Si bond angle, the silica structure of ion irradiated films after irradiation with 1 MeV Cu^+ and 4 MeV Cu^{2+} at the highest fluence is similar to the structure of silica under applied pressures of 12.7 and 16.8 GPa, respectively. This in return indicates the elastic modulus of 94 GPa and 107 GPa for the silica phase in the films irradiated with 1 MeV Cu^+ and 4 MeV Cu^{2+} at the highest fluence. The measured values of elastic modulus of the films after irradiation with 1 MeV Cu^+ and 4 MeV Cu^{2+} ions at the highest fluence were 93 GPa and 118 GPa, respectively which are close to the estimated values for the elastic modulus of the silica phase. After ion irradiation with 9 MeV Cu^{3+}, the structure of silica has started to change its coordination number, which for pressured silica starts at 20-25 Ga [57,180]. This corresponds to elastic modulus of 129 GPa for the silica structure after irradiation with 9 MeV Cu^{3+}. The estimated elastic modulus of the silica phase is close to the measured elastic modulus of the films (147 GPa). The elastic modulus of the stishovite, the high pressure, octahedrally bonded phase of silica is reported to be 400 GPa [62]. The partial transformation of tetrahedrally bonded silica to octahedrally bonded silica may also increase the elastic modulus of the films irradiated with 9 MeV Cu^{3+} ions. The elastic modulus values of films after irradiation with 9 MeV Cu^{3+}, with 10^{15} and 10^{16} ions/cm^2 are similar which may be related to the negative effect of the decrease in the density of the film irradiated with 9 MeV Cu^{3+} with a fluence of 10^{16} ions/cm^2 (Fig. 4.22) which cancels out the positive effect of the decrease in Si-O-Si bond angle and the formation of octahedrally bonded silica.

In addition, the increase in the concentration of carbon-rich SiO_xC_y, as inferred from the XPS and FT-IR results, also increases the elastic modulus of the films. However, the effect is secondary to the modification of the silica structure, as the values for elastic modulus of the compacted silica phase and the films are similar.

Based on the above discussion, the higher elastic modulus of the 1 MeV Cu^+ irradiated films compared to fused silica is due to the combined effects of the reduction in Si-O-Si bond angle, as well as the formation of carbon rich SiO_xC_y tetrahedra. The higher elastic modulus of the films after ion irradiation with 4 MeV Cu^{2+} is related to even higher compaction in the silica structure due to an irradiation-induced decrease in bond angle, as well as larger concentrations of SiO_xC_y tetrahedra. In addition to these parameters, the increase in elastic modulus of the films irradiated with 9 MeV Cu^{3+} also originates from the formation of pockets of octahedrally bonded silica. The effect of the formation of SiO_xC_y tetrahedra is secondary to the changes in the structure of silica.

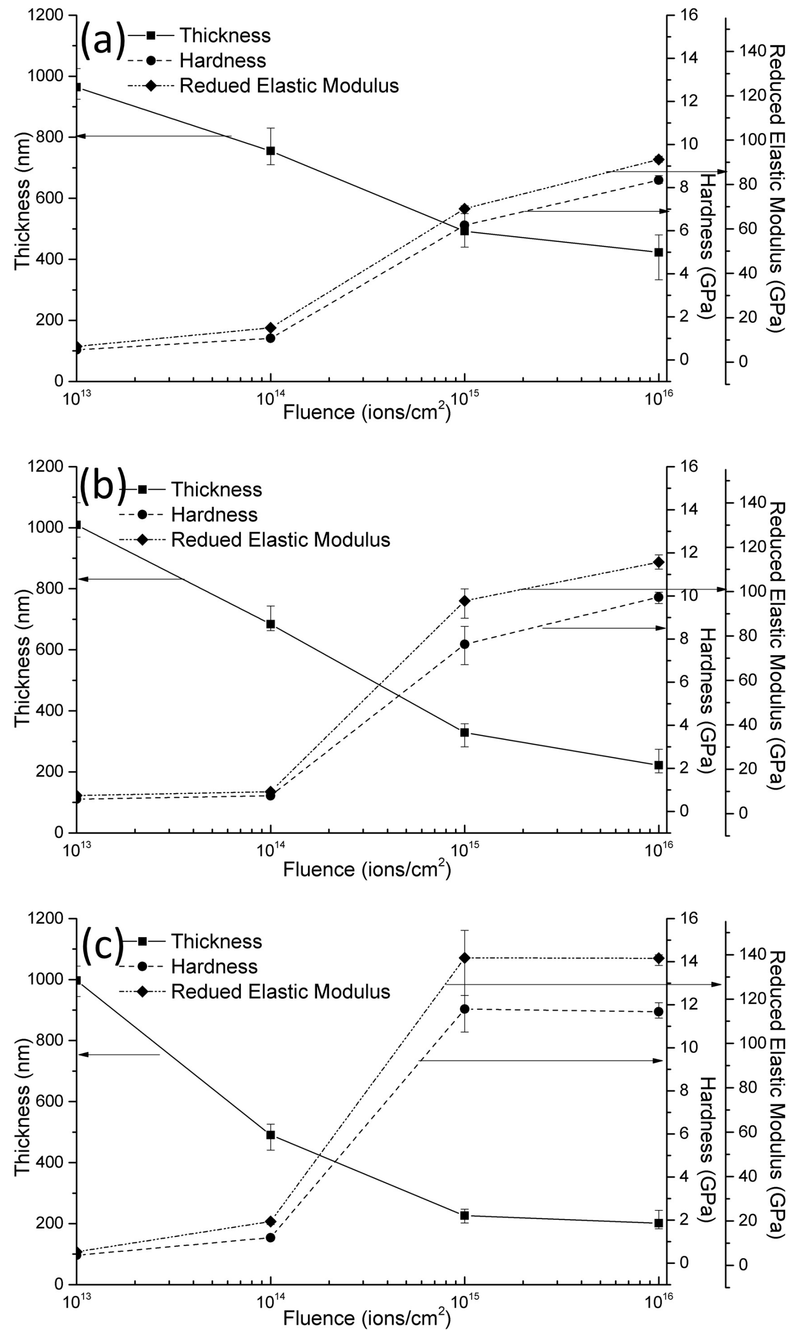

Figure 4.38: Film thickness, hardness, and reduced elastic modulus of the films after ion irradiation with a) 1 MeV Cu^{+} b) 4 MeV Cu^{2+} and c) 9 MeV Cu^{3+}. The data is adapted from [158].

4.4 Secondary heat-treatment of ion irradiated films

A secondary heat-treatment was performed on the ion irradiated films to observe any possible effect of the annealing process including structural release, recrystallization, and synthesis of silicon carbide nanoparticles. The simultaneous presence of amorphous silica and free carbon provides the possibility of synthesizing SiC through a secondary heat-treatment. The experiments were performed on base-catalyzed irradiated films. The ion irradiation and heat-treatment conditions of the base-catalyzed films are shown in Table 3.3.

Figure 4.39 shows SEM images of the N^{2+} irradiated base-catalyzed films with a fluence of 10^{16} ions/cm^2 before and after secondary heat-treatment at 1100 °C. Crack formation after secondary heat-treatment can be observed in SEM images. This is related to chemical reactions between the films and the silicon substrate [85]. The exact mechanism involves the reaction of silicon with amorphous silica at elevated temperatures to form gaseous SiO [206]:

$$SiO_{2(s)} + Si_{(s)} \rightarrow 2SiO_{gas} \tag{4.6}$$

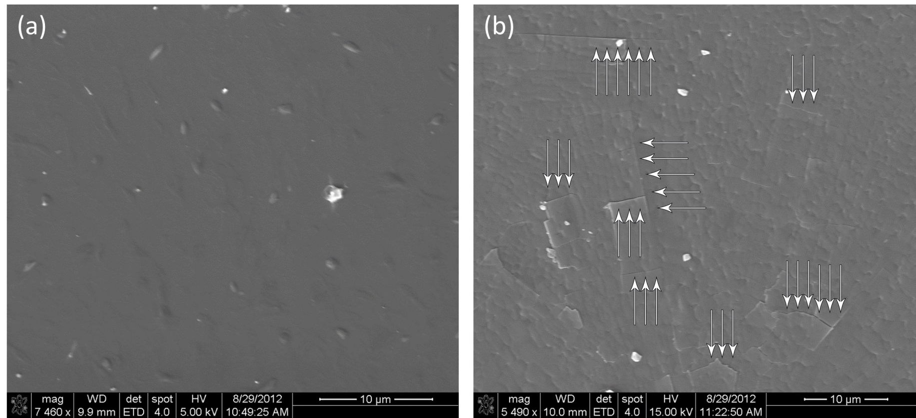

Figure 4.39: SEM images of base-catalyzed thin films a) ion irradiated with N^{2+} ions with a fluence of 10^{16} ions/cm^2 and b) the same film after heat-treatment at 1100 °C. The arrows indicate the formed cracks.

4.4.1 FT-IR spectroscopy characterization of ion irradiated base-catalyzed films after secondary heat-treatment

Reflection FT-IR spectra of the ion irradiated films after secondary heat-treatment at 1100 °C and 1350 °C are presented in Figs. 4.40 and 4.41, respectively and the results of curve fitting are presented in Table 4.7. The peak around 471 cm^{-1} is another Si-O-Si related peak [207]. The FT-IR peak at 800 cm^{-1} is also from Si-O-Si bending [208]. The small peak around 670 cm^{-1} is related to the silicon substrate [209].

The higher density of N^{2+} irradiated films after secondary heat-treatment compared to H^{+} irradiated films, as inferred from I(TO)/I(LO) values, is related to a higher level of bond disorder in the N^{2+} irradiated films and the subsequent higher driving force for structural modification during annealing.

Compared to previous films, the films after secondary heat-treatment have a higher TO peak spectral center. This is a result of structural release during secondary heat-treatment. The TO spectral center at roughly 1100 cm^{-1} corresponds to a bond angle of 149°, which is the bond angle of crystalline α-cristobalite [210]. XRD was also performed on one of the ion irradiated films after secondary heat-treatment and the XRD pattern in presented in Fig. 4.42. The results indicate the formation of crystalline α-cristobalite. The structural release and the increase in the bond angle of Si-O-Si as a result of annealing, may explain the previous diminishing of the mechanical properties of the ion irradiated films after a secondary heat-treatment, as observed in a previous study [21].

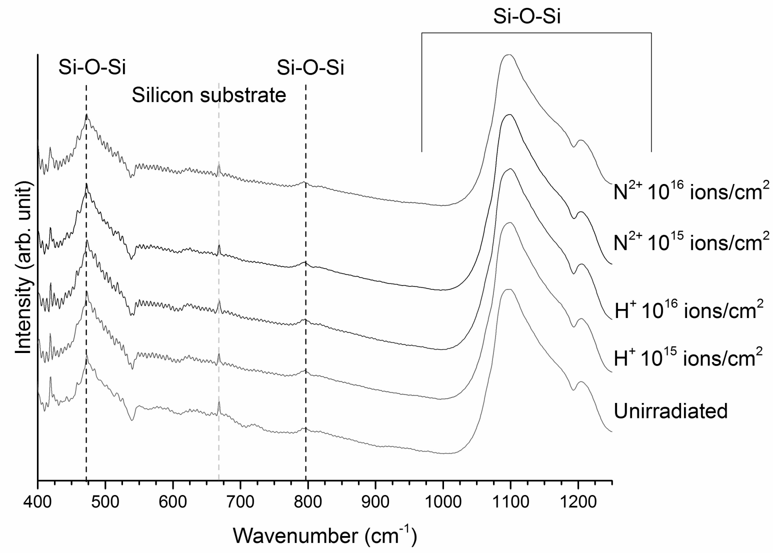

Figure 4.40: Reflection FT-IR spectra of the ion irradiated base-catalyzed films after a secondary heat-treatment at 1100 °C.

Table 4.7: Curve fitting results of FT-IR spectra of base-catalyzed films irradiated with H^+ and N^{2+} ions after secondary heat-treatment at 1100 °C and 1350 °C.

Film condition	TO peak spectral center	Si-O-Si bond angle(°)	I(LO)/I(TO)	I(O-Si-C)/I(TO)
Unirradiated- 1100 °C	1094	149	0.25	0.68
Unirradiated- 1350 °C	1100	152	0.24	0.52
H^+-10^{15} ions/cm^2 1100 °C	1094	149	0.25	0.69
H^+-10^{15} ions/cm^2 1350 °C	1107	154	0.185	0.23
H^+-10^{16} ions/cm^2 1100 °C	1094	149	0.25	0.72
H^+-10^{16} ions/cm^2 1350 °C	1104	153	0.18	0.3
N^{2+}-10^{15} ions/cm^2 1100 °C	1094	149	0.24	0.7
N^{2+}-10^{15} ions/cm^2 1350 °C	1109	155	0.17	0.14
N^{2+}-10^{16} ions/cm^2 1100 °C	1094	149	0.25	0.67
N^{2+}-10^{16} ions/cm^2 1350 °C	1109	155	0.17	0.14

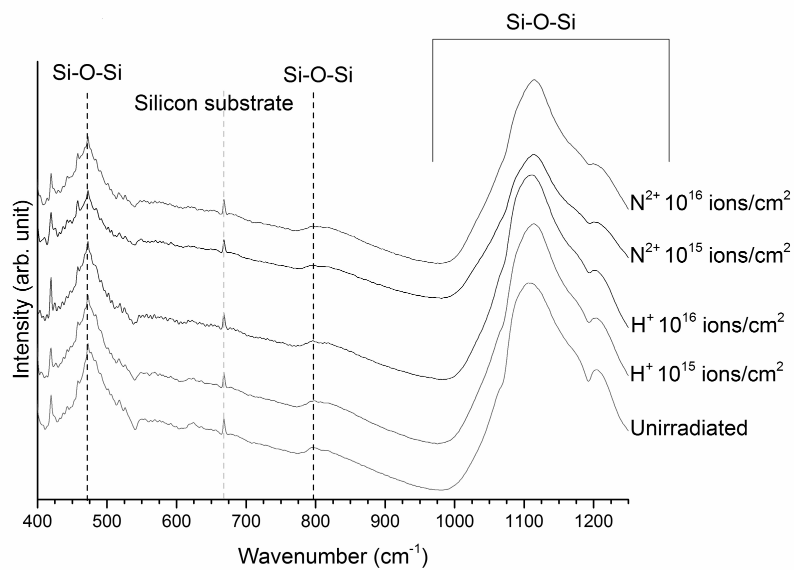

Figure 4.41: Reflection FT-IR spectra of the ion irradiated base-catalyzed films after a secondary heat-treatment at 1350 °C.

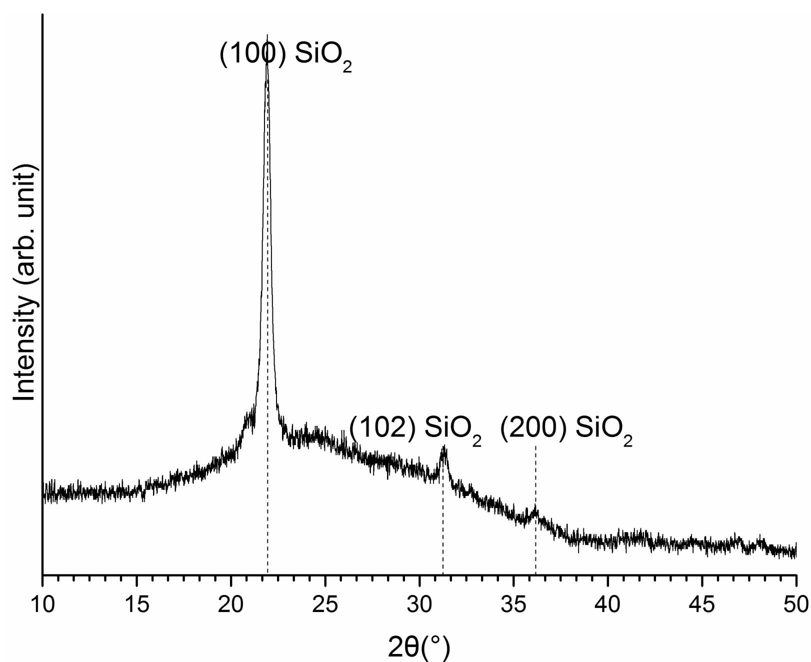

Figure 4.42: XRD pattern of a based-catalyzed ion irradiated film after ion irradiation with N^{2+} ions at 10^{16} ions/cm^2 and a secondary heat-treatment at 1350 °C. The observed XRD peaks correspond to the XRD pattern of α-cristobalite (JCPDS Number: 39-1425).

4.4.2 Raman spectroscopy characterization of ion irradiated base-catalyzed films after secondary heat-treatment

The Raman spectra of the ion irradiated base-catalyzed films after secondary heat-treatment at 1100 °C exhibit D and G Raman modes. No carbon related Raman modes are observed after secondary heat-treatment at 1350 °C. The carbon formed during ion irradiation of the base-catalyzed films is highly defective carbon [87], similar to that previously observed in Section 4.2.3. However after secondary heat-treatment at 1100 °C, the Raman spectra of the free carbon within the films is similar to nanocrystalline graphitic carbon formed by heat-treatment. The Raman spectra of the films after secondary heat-treatment at 1100 °C are presented in Fig. 4.43.

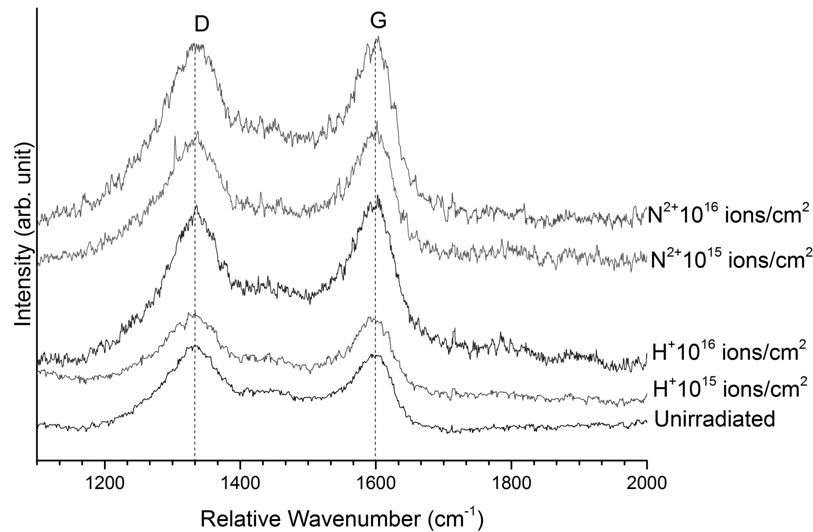

Figure 4.43: Raman spectroscopy results of base-catalyzed ion irradiated films after secondary heat-treatment at 1100 °C.

In order to study the nature of carbon within the films after secondary heat-treatment, curve fitting was performed on the Raman spectra. Unlike previous films, the Raman spectra of the ion irradiated films after secondary heat-treatment are better fitted with two BWF curves, as expected from the literature for nanocrystalline graphite [35]. A summary of the results are presented in Table 4.8.

Compared to as-irradiated films, the free carbon clusters of all the films annealed at 1100 °C exhibit a lower level of disorder. The size of the free carbon clusters for all of the films is estimated from Equation 4.2 to be between 4 to 5 nm.

In summary, the XRD, Raman, and FT-IR results of the ion irradiated films after a secondary heat-treatment indicates a release of induced structural damage and an ordering of the structure. In addition, there is no indication of the formation of secondary SiC clusters.

Table 4.8: Curve fitting results of the Raman spectra of base-catalyzed films after secondary heat-treatment.

Film condition	W(G) (cm^{-1})	FWHM(G) (cm^{-1})	I(D)/I(G)
Unirradiated	1600	51	1
H^+-10^{15} ions/cm^2 1100 °C	1590	60	1.3
H^+-10^{16} ions/cm^2 1100 °C	1595	65	1
N^{2+}-10^{15} ions/cm^2 1100 °C	1584	41	1.3
N^{2+}-10^{16} ions/cm^2 1100 °C	1586	74	1.3

In addition to the base-catalyzed films, a secondary heat-treatment was also performed on an unirradiated acid-catalyzed film at 1100 °C and 1350 °C. In the acid-catalyzed films, unlike the base-catalyzed films, most of the carbon is lost during thermal decomposition. And so, the final structure of the films after heat-treatment at 1100 and 1350 °C is just a silica network. Heat-treatment at 1350 °C leads to the formation of crystalline silica (α-cristobalite) as shown in Fig 4.44. All the visible peaks in the XRD pattern of the film correspond to crystalline α-cristobalite (JCPDS Number: 39-1425).

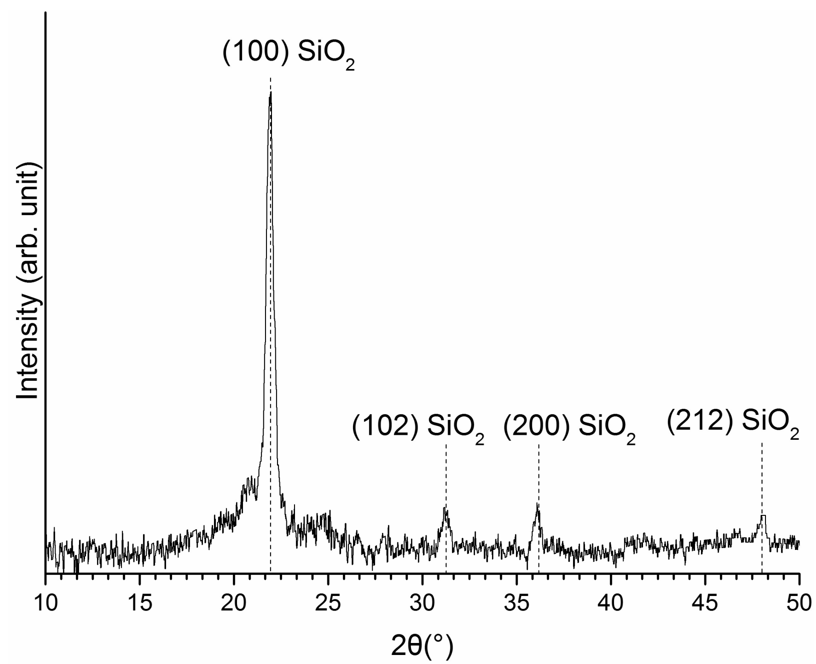

Figure 4.44: XRD Pattern of unirradiated acid-catalyzed films after heat-treatment at 1350 °C. The observed XRD peaks correspond to the XRD pattern of α-cristobalite (JCPDS Number: 39-1425).

Chapter 5

CONCLUSIONS AND POSSIBLE FUTURE WORK

5.1 Conclusions

1. Ion irradiation was performed using 200 keV H^+, 400 keV N^{2+}, 1 MeV Cu^+, 4 MeV Cu^{2+}, and 9 MeV Cu^{3+} ions at different fluences. Irradiation with all ion species successfully decomposes the starting organic materials and leads to the formation of an amorphous microstructure of silica and sp^2 bonded carbon. The decomposition is mostly achieved through hydrogen loss after irradiation with H^+ and N^{2+} ions. XRD experiments show that the films are amorphous after ion irradiation. An increase in the density of the films after ion irradiation is observed.

2. FT-IR spectroscopy investigation of H^+ and N^{2+} irradiated films indicates the incorporation of carbon within the silica network during ion irradiation. In addition, a decrease in porosity and bond angle of the Si-O-Si bonds is observed. The decrease in porosity and bond angle is larger in N^{2+} irradiated films compared to H^+ irradiated films. The results are consistent with previous studies on the effects of ion irradiation on the structure of amorphous silica.

3. Raman spectroscopy results indicate the formation of carbon clusters after ion irradiation at higher fluences with both H^+ and N^{2+} irradiation. The carbon clusters are found to be disordered sp^2 bonded carbon. A method is proposed to estimate the carbon cluster size of the ion irradiated films.

4. Unlike ion irradiated films, the microstructure of the films after heat-treatment consists only of amorphous silica. The formation of carbon clusters is only observed at intermediate heat-treatment

temperatures. The carbon clusters formed at intermediate temperatures consist of nanocrystalline graphite. The amorphous silica network in the heat-treated films is more porous than the H^+ and N^{2+} irradiated films.

5. Photoluminescence spectra of the films indicate that the free carbon clusters formed during ion irradiation are hydrogenated amorphous carbon. The hydrogen content of amorphous carbon decreases after ion irradiation with higher energies at higher fluences.

6. XPS results of the films confirm the results obtained by FT-IR spectroscopy. The XPS results confirm the incorporation of carbon within the silica network after ion irradiation. XPS derived chemical compositions are in agreement with ERD/RBS derived chemical compositions of the films. The trend in the changes of chemical composition is similar between the XPS and ERD/RBS results.

7. Based on Raman spectroscopy, FT-IR spectroscopy, ERD/RBS, and XRD results, the microstructure of the H^+ and N^{2+} irradiated films is an amorphous mixture of hydrogenated carbon clusters and silica. The suggested microstructural configuration of the H^+ and N^{2+} irradiated films is an amorphous silica matrix with isolated carbon clusters.

8. The results from Conclusions 2, 5, and 7 are utilized to explain an increase in elastic modulus of the H^+ and N^{2+} irradiated films. In addition to decomposition of the starting organic materials and a decrease in the porosity of the films as a result of ion irradiation, changes induced by ion irradiation in the structure of individual phases within the films are also found to enhance the elastic modulus of the films. The decrease in the bond angle of Si-O-Si leads to a change in the elastic deformation mechanism of amorphous silica. The incorporation of carbon within the silica structure and the formation of Si-C bonds may also enhance the mechanical properties of the films, but its effect is secondary to the changes in the bond angle of silica. In addition, the hydrogen loss after ion irradiation leads to the formation of carbon clusters that do not decrease the elastic modulus of the films. After irradiation with H^+, no enhancement due to a decrease in Si-O-Si bond angle is expected. However, the enhancement in the mechanical properties of the N^{2+} irradiated films is mostly related to a decrease in the Si-O-Si bond angle.

9. Conversion of the films was also performed using 1 MeV Cu^+, 4 MeV Cu^{2+}, and 9 MeV Cu^{3+} ions. While ion irradiation with H^+ and N^{2+} only leads to hydrogen loss, irradiation with 1 MeV Cu^+, 4 MeV Cu^{2+}, and 9 MeV Cu^{3+} also results in carbon and oxygen loss. The density of the films also increases with increasing ion energy and fluence.

10. Ion irradiation with heavy ions leads to modification of the amorphous silica structure. After ion irradiation with 1 MeV Cu^+ and 4 MeV Cu^{2+}, the Si-O-Si bond angle is measured to be 130° and 124°, respectively. In addition, ion irradiation with 9 MeV Cu^{3+} ions leads to the disappearance

of the FT-IR peaks related to silica, which is an indication of the onset of tetrahedral to octahedral transformation in silica. The results from XPS and Raman spectroscopy also confirm the observed changes in the structure of amorphous silica. A combination of irradiation induced thermal spikes and formation of vacancies and subsequent structural relaxation is found to be responsible for the changes in the structure of the silica phase.

11. Raman spectroscopy investigation of films irradiated with heavy ions reveals that the signature D and G Raman modes are not present in the Raman response of the films after irradiation with 4 MeV Cu^{2+} and 9 MeV Cu^{3+} at the highest fluences. Instead, a Raman mode is observed at 1430 cm^{-1} which is attributed to the presence of sp^2 bonded carbon within the films, but in a form other than six-fold graphitic rings. The results of Raman spectroscopy of carbon clusters are confirmed by XPS.

12. The microstructure of the films irradiated with heavy ions consists of individual sp^2 bonded carbon clusters within an amorphous silica network with either tetrahedrally or octahedrally bonded silica structure.

13. Elastic modulus and hardness of the films irradiated with heavy ions are higher than H^+ and N^{2+} irradiated films, fused silica, and heat-treated SiOC specimens. The smaller bond angle of amorphous silica, gradual transformation from tetrahedrally bonded to octahedrally bonded silica, and the formation of Si-C bonds are found to enhance the mechanical properties of the films. The changes in the structure of amorphous silica is found to be the dominant parameter dictating the mechanical properties.

14. Secondary heat-treatment of ion irradiated base-catalyzed films indicates a structural relaxation, as well as a chemical reaction between the films and the substrate after secondary heat-treatment. The Raman and FT-IR results indicate that the free carbon and silica phases within the structure are different from the as-irradiated films and are more similar to the structure of phases within a heat-treated SiOC film. The XRD pattern of the heat-treated films indicates the formation of crystalline α-cristobalite.

15. The results in the current study, specifically the dependence of elastic modulus on the Si-O-Si bond angle, can also explain the observed increase in the elastic modulus of ion irradiated films from a previous study [21].

16. Table 5.1 summarizes the proposed microstructure of different ion irradiated films.

Table 5.1: The proposed microstructure of ion irradiated films

Irradiation condition	Silica	Free carbon	Silicon carbide
200 keV H^{+}	tetrahedrally bonded silica with average Si-O-Si bond angle of 139°	Hydrogenated, amorphous sp^2 bonded carbon in graphitic configuration	Not observed
400 keV N^{2+}	tetrahedrally bonded silica with average Si-O-Si bond angle of 135°	Hydrogenated, amorphous sp^2 bonded carbon in graphitic configuration	Not observed
1 MeV Cu^{+}	tetrahedrally bonded silica with average Si-O-Si bond angle of 130°	Amorphous sp^2 bonded carbon in graphitic configuration	Not observed
4 MeV Cu^{2+}	tetrahedrally bonded silica with average Si-O-Si bond angle of 124°	Amorphous sp^2 bonded carbon in non-graphitic configuration	Not observed
9 MeV Cu^{3+}	A combination of tetrahedrally and octahedrally bonded silica	Amorphous sp^2 bonded carbon in non-graphitic configuration	Not observed

5.2 Possible Future Work

- The structure of silicon oxycarbide tetrahedra and octahedras can be better understood using additional characterization techniques. Specifically, NMR spectroscopy has a higher resolution than other competing techniques and can fully distinguish between the different silica tetrahedra and octahedras.

- Studying the effects of ion irradiation conditions on the deformation mechanism of the films can be achieved by studying the indentation impression on the surface which can provide additional insight into the mechanical deformation mechanism of the ion irradiated films.

- Repeating the ion irradiation experiments on fully converted SiOC films with varying levels of carbon and studying the effects of ion irradiation and carbon content can be useful in evaluating the enhancement in the mechanical properties of the films without the interference from the decomposition parameters.

- Measurement of other physical and chemical properties of the films (e.g., optical, electrical, and corrosion resistance) can help to open the door for new applications for ion irradiated thin films.

Bibliography

[1] E. Brinksmeier, O. Riemer, W. Preuß, F. Klocke, T. Pfeifer, M. Weck, W. Michaeli, P. Mayr, H.-R. Stock, A. Mehner, G. Goch, and D.A. Lucca. Process chains for the replication of complex optical elements. *Annals of the WGP*, pages 61–64, 2004.

[2] E. Brinksmeier, O. Riemer, and R.M. Gläbe. *Fabrication of Complex Optical Components: from Mold Design to Product*. Springer Science and Business Media, 2013.

[3] W. Datchary, A. Mehner, H.-W. Zoch, D.A. Lucca, M.J. Klopfstein, R. Ghisleni, D. Grimme, and E. Brinksmeier. High precision diamond machining of hybrid sol-gel coatings. *Journal of Sol-Gel Science and Technology*, 35:245–251, 2005.

[4] A. Mehner, W. Datchary, N. Bleil, H.-W. Zoch, M.J. Klopfstein, and D.A. Lucca. The influence of processing on crack formation, microstructure, density and hardness of sol-gel derived zirconia films. *Journal of Sol-Gel Science and Technology*, 36:25–32, 2005.

[5] A. Mehner, J. Dong, H.W. Zoch, E. Brinksmeier, D. Grimme, D.A. Lucca, R. Ghisleni, W. Michaeli, and F. Klaiber. Diamond machinable sol-gel SiO_xC_y coatings for high precision optical molds. *Proceedings of the 6th International Conference of Coatings in Manufacturing Engineering, Hannover, Germany*, pages 55–64, 2007.

[6] A. Mehner, J. Dong, T. Hoja, T. Prenzel, Y. Mutlugünes, E. Brinksmeier, D.A. Lucca, and F. Klaiber. Diamond machinable sol-gel silica based hybrid coatings for high precision optical molds. *Key Engineering Materials*, 438:65–72, 2010.

[7] R. Ghisleni an L. Shao, D.A. Lucca, V. Doan, M. Nastasi, J. Dong, and A. Mehner. Effects of heat treatment and ion irradiation on hybrid organic/inorganic sol-gel derived thin films. *Nuclear Instruments and Methods in Physics Research Section B*, 261:708–710, 2007.

[8] D.A. Lucca, M.J. Klopfstein, R. Ghisleni, A. Gude, A. Mehner, and W. Datchary. Investigation of sol-gel derived ZrO_2 thin films by nanoindentation. *CIRP Annals-Manufacturing Technology*, 53:475–478, 2004.

[9] J.E. ten Elshof, S.U. Khan, and O.F. Göbel. Micrometer and nanometer-scale parallel patterning of ceramic and organic-inorganic hybrid materials. *Journal of the European Ceramic Society*, 30:1555–1577, 2010.

[10] X. Zhang, M. Qian, X. Zeng, Z. Zhao, J. Lasante, and P. Plante. Design and fabrication of single mode rib waveguides using sol-gel derived organic-inorganic hybrid materials. *Journal of Sol-Gel Science and Technology*, 45:103–107, 2008.

[11] D. Balgude and A. Sabnis. Sol-gel derived hybrid coatings as an environment friendly surface treatment for corrosion protection of metals and their alloys. *Journal of Sol-Gel Science and Technology*, 64:124–134, 2012.

[12] P. Colombo, R. Riedel, G.D. Sorarú, and H.J. Kleebe, editors. *Polymer Derived Ceramics From Nanostructure to Applications*, chapter Historical Review of the Development of Polymer Derived Ceramics (PDCs). DEStech Publications Inc, 2010.

[13] P. Colombo, G. Mera, R. Riedel, and G.D. Sorarú. Polymer-derived ceramics: 40 years of research and innovation in advanced ceramics. *Journal of the American Ceramic Society*, 93:1805–1837, 2010.

[14] S. Zulfiqar, Z. Ahmad, M. Ishaq, S. Saeed, and M.I. Sarwar. Thermal and mechanical properties of SEBS-g-MA based inorganic composite materials. *Journal of Materials Science*, 42:93–100, 2007.

[15] L. Pavesi and R. Turan, editors. *Silicon Nanocrystals: Fundamentals, Synthesis and Applications*, chapter Si and SiC nanocrystals by pyrolysis of sol-gel derived precursors. Wiley-VCH, 2010.

[16] K. Izumi, H. Tanaka, Y. Uchida, N. Tohge, and T. Minami. Influence of firing conditions on adhesion of methyltrialkoxysilane-derived coatings on steel sheets. *Journal of Non-Crystalline Solids*, 147-148:483–487, 1992.

[17] S. Santucci, S. Di Nardo, L. Lozzi, M. Passacantando, and P. Picozzi. XPS analysis on SiO_2 sol-gel thin films. *Journal of Electron Spectroscopy and Related Phenomena*, 76:623–628, 1995.

[18] E. Ionescu, C. Balan, H.-J. Kleebe, M.M. Müller, O. Guillon, D. Schliephake, M. Heilmaier, and R. Riedel. High-temperature creep behavior of SiOC glass-ceramics: Influence of network carbon versus segregated carbon. *Journal of the American Ceramic Society*, 97:3935–3942, 2014.

[19] T. Venkatesan. High energy ion beam modification of polymer films. *Nuclear Instruments and Methods in Physics Research Section B*, 7-8:461–467, 1985.

[20] E.Z. Kuramev, A. Moewes, J.-C. Pivin, M. Bach, K. Endo, T. Ida, S. Shimada, M. Neumann, S.N. Shamin, D.L. Ederer, and M. Iwami. Polymer conversion into amorphous ceramics by ion irradiation. *Journal of Material Science*, 37:3789–3793, 2002.

[21] R. Ghisleni. *Effects of Ion Irradiation on the Surface Mechanical Behavior of Hybrid Sol-Gel Derived Silicate Thin Films*. Ph.D. Dissertation, Oklahoma State University, 2007.

[22] J.C. Pivin, P. Colombo, M. Sendova-Vassileva, J. Salomon, G. Sagon, and A. Quaranta. Ion-induced conversion of polysiloxanes and polycarbosilanes into ceramics: mechanisms and properties. *Nuclear Instruments and Methods in Physics Research Section B*, 141:652–662, 1998.

[23] A. Kumar, F. Singh, J.C. Pivin, and D.K. Avasthi. Photoluminescence studies of carbon clusters formed by irradiation of Si-based polymer. *Radiation Measurements*, 40:785–788, 2005.

[24] E.Z. Kurmaev, A. Moewes, M. Krietemeyer, K. Endo, T. Ida, S. Shimada, R.P. Winarski, M. Neumann, S.N. Shamin, and D.L. Ederer. X − ray fluorescence study of organic-inorganic polymer conversion into ceramics induced by ion irradiation. *Physical Review B*, 60:15100–15106, 1999.

[25] J.C. Pivin, P. Colombo, and G.D. Sorarú. Comparison of ion irradiation effects in silicon-based preceramic thin films. *Journal of the American Ceramic Society*, 83:713–720, 2000.

[26] H.J. Kleebe, H. Störmer, S. Trassl, and G. Ziegler. Thermal stability of SiCN ceramics studied by spectroscopy and electron microscopy. *Applied Organometallic Chemistry*, 15:858–866, 2001.

[27] S. Mártinez-Crespiera, E. Ionescu, H.J. Kleebe, and R. Riedel. Pressureless synthesis of fully dense and crack-free SiOC bulk ceramics via photo-crosslinking and pyrolysis of a polysiloxane. *Journal of the European Ceramic Society*, 31:913–919, 2011.

[28] G. Gregori, H.J. Kleebe, Y.D. Blum, and F. Babonneau. Evolution of C-rich SiOC ceramics part II. characterization by high lateral resolution techniques: electron energy-loss spectroscopy, high-resolution TEM and energy-filtered TEM. *International Journal of Materials Research*, 97:710–720, 2006.

[29] A. Saha, R. Raj, and D.L. Williamson. A model for the nanodomains in polymer-derived SiCO. *Journal of the American Ceramic Society*, 89:2188–2195, 2006.

[30] J. Dürr, S. Schempp, P. Lamparter, J. Bill, S. Steeb, and F. Aldinger. $X-$ray and neutron small angle scattering with $Si-C-N$ ceramics using isotopic substitution. *Solid State Ionics*, 101-103:1041–1047, 1997.

[31] A. Saha and R. Raj. Crystallization maps for SiCO amorphous ceramics. *Journal of the American Ceramic Society*, 90:578–583, 2007.

[32] G.D. Sorarú, G. D'Andrea, R. Campostrini, F. Babonneau, and G. Mariotto. Structural characterization and high-temperature behavior of silicon oxycarbide glasses prepared from sol-gel precursors containing $Si-H$ bonds. *Journal of the American Ceramic Society*, 78:379–387, 1995.

[33] G. Das, P. Bettotti, L. Ferraioli, R. Raj, G. Mariotto, L. Pavesi, and G.D. Sorarú. Vibrational study of the pyrolysis process of an hybrid $CH_3SiO_{1.5}$ gel into a SiCO glass. *Vibrational Spectroscopy*, 45:61–68, 2007.

[34] H.-J. Kleebe and Y.D. Blum. SiOC ceramic with high excess free carbon. *Journal of the European Ceramic Society*, 28:1037–1042, 2008.

[35] A.C. Ferrari and J. Robertson. Interpretation of Raman spectra of disordered and amorphous carbon. *Physical Review B*, 61:14095, 2000.

[36] T. Jiang, Y. Wang, Y. Wang, N. Orlovskaya, and L. An. Quantitative Raman analysis of free carbon in polymer-derived ceramics. *Journal of the American Ceramic Society*, 92:2455–2458, 2009.

[37] N.P. Bansa and A.R. Boccaccini. *Ceramics and Composites Processing Methods*. Wiley, 2012.

[38] A.C. Ferrari and J. Robertson. Resonant Raman spectroscopy of disordered, amorphous, and diamondlike carbon. *Physical Review B*, 64:075414, 2001.

[39] J. Robertson. Diamond-like amorphous carbon. *Materials Science and Engineering R*, 37:129–281, 2002.

[40] M.A. Tamor and W.C. Vassell. Raman "fingerprinting" of amorphous carbon films. *Journal of Applied Physics*, 76:3823–3830, 1994.

[41] P. Lespade, R. Al-Jaishi, and M.S. Dresselhaus. Model for Raman scattering from incompletely graphitized carbons. *Carbon*, 20:427–431, 1982.

[42] D. Beeman, J Silverman, R. Lynds, and M.R. Anderson. Modeling studies of amorphous carbon. *Physical Review B*, 30:870–875, 1984.

[43] E.L. Bouhris, editor. *Glass Mechanics and Technology*. John Wiley and Sons, 2008.

[44] H.S. Nalwa, editor. *Silicon-Based Material and Devices, Volume 1: Properties and Devices*, chapter Amorphous Silica. Academic Press, 2001.

[45] M.G. Tucker, D.A. Keen, M.T. Dove, and K. Tranchenko. Refinement of the $\mathrm{Si-O-Si}$ bond angle distribution in vitreous silica. *Journal of Physics: Condensed Matter*, 17:S67–S75, 2005.

[46] P.N. Sen and M.F. Thorpe. Phonons in AX_2 glasses: From molecular to band-like modes. *Physical Review B*, 15:4030–4038, 1977.

[47] A. Lehmann, L. Schumann, and K. Hübner. Optical phonons in amorphous silicon oxides. I. calculation of the density of states and interpretation of $\mathrm{LO-TO}$ splittings of amorphous SiO_2. *Physica Status Solidi (B)*, 117:689–698, 1983.

[48] F. Mauri, A. Pasquarello, B.G. Pfrommer, Y.-G. Yoon, and S.G. Louie. $\mathrm{Si-O-Si}$ bond-angle distribution in vitreous silica from first-principles ^{29}Si NMR analysis. *Physical Review B*, 62:R4786–R4789, 2000.

[49] X. Yuan and A.N. Cormack. $\mathrm{Si-O-Si}$ bond angle and torsion angle distribution in vitreous silica and sodium silicate glasses. *Journal of Non-Crystalline Solids*, 319:31–43, 2003.

[50] D. Uhlmann and N.J. Kreidl. *Elasticity and Strength in Glasses: Glass: Science and Technology*, volume 5. Academic Press, 1980.

[51] K. Awazu and H. Kawazoe. Strained Si-O-Si bonds in amorphous SiO_2 materials: A family member of active centers in radio, photo, and chemical responses. *Journal of applied physics*, 94:6243–6262, 2003.

[52] K. Awazu, S. Ishii, K. Shima, S. Roorda, and J. Brebner. Structure of latent tracks created by swift heavy-ion bombardment of amorphous SiO_2. *Physical Review B*, 62:3689–3698, 2000.

[53] B. Garrido, J. Samitier, S. Bota, J.A. Moreno, J. Montserrat, and J.R. Morante. Reconstruction of the SiO_2 structure damaged by low-energy Ar-implantedions. *Journal of Applied Physics*, 81:126–134, 1997.

[54] F.P. Mallinder and B.A. Proctor. Elastic constants of fused silica as a function of large tensile strains. *Physics and Chemistry of Glasses*, 5:91–103, 1964.

[55] H. Kobayashi. Anharmonicity and elastic hysteresis of fused SiO_2 fibers. *Journal of Applied Physics*, 49:4776–4778, 1978.

[56] V.N. Bognadov, I.M. Brovchenko, L.V. Maksimov, A.R. Silin, and O.V. Yanush. Spectroscopic, optical, and acoustic investigations of radiation modified silica glasses. *Physica Status Solidi (A)*, 119:621–629, 1990.

[57] N. Li, R. Sakidja, S. Aryal, and W.Y. Ching. Densification of a continuous random network model of amorphous SiO_2 glass. *Physical Chemisty Chemical Physics*, 16:1500–1514, 2014.

[58] H. Fan, C. Hartshorn, T. Buchheit, D. Tallant, R. Assink, R. Simpson, D.J. Kissel, D.J. Lacks, S. Torquato, and C.J. Brinker. Modulus-density scaling behaviour and framework architecture of nanoporous self-assembled silicas. *Nature materials*, 6, 2007.

[59] G.J. Curtis, J.M. Milne, and W.N. Reynolds. Non-Hookean behaviour of strong carbon fibres. *Nature*, 220:1024–1025, 1968.

[60] N.L. Ross, J. Shu, and R.M. Hazen. High-pressure crystal chemistry of stishovite. *American Mineralogist*, 75:739–747, 1990.

[61] A.F. Reid, A.D. Wadsley, and A.E. Ringwood. High pressure $NaAlGeO_4$, a calcium ferrite isotype and model structure of silicates at depth in the earth's mantle. *Acta Crystallographica*, 23:736–739, 1967.

[62] C. Meade, R. J Hemley, and H.K. Mao. High-Pressure X-Ray Diffraction of SiO_2 Glass. *Physical Review Letters*, 69:1387–1391, 1992.

[63] A. Karakuscu, R. Guider, L. Pavesi, and G.D. Sorarú. Synthesis and optical properties of SiC_{nc}/SiO_2 nanocomposite thin films. *Nanostructured Materials and Nanotechnology II: Ceramic Engineering and Science Proceedings*, 29:85–91, 2008.

[64] S. Jou, C.-T. Sun, and X. Chen. Silicon carbide films from polycarbosilane and their usage as buffer layers for diamond deposition. *Diamond and Related Materials*, 14:1688–1694, 2005.

[65] V. Raman, O.P. Bahl, and U. Dhawan. Synthesis of silicon carbide through the sol-gel process from different precursors. *Journal of Materials Science*, 30:2686–2693, 1995.

[66] A. Najafi, F. Golestani-Fard, H. R. Rezaie, and N. Ehsani. A study on sol-gel synthesis and characterization of SiC nano powder. *Journal of Sol-Gel Science and Technology*, 59:205–214, 2011.

[67] G.D. Sorarú, S. Modena, P. Bettotti, G. Das, G. Mariotto, and L. Pavesi. Si nanocrystals obtained through polymer pyrolysis. *Applied Physics Letters*, 83:749–751, 2003.

[68] S.J. Widgeon, S. Sen, G. Mera, E. Ionescu, R. Riedel, and A. Navrotsky. ^{29}Si and ^{13}C solid-state NMR spectroscopic study of nanometer-scale structure and mass fractal characteristics of amorphous polymer derived silicon oxycarbide ceramics. *Chemistry of Materials*, 22:6221–6228, 2010.

[69] G. Mera, A. Navrotsky, S. Sen, H.-J. Kleebe, and R. Riedel. Polymer-derived SiCN and SiOC ceramics structure and energetics at the nanoscale. *Journal of Materials Chemistry A*, 1:3826–3836, 2013.

[70] R. Riedel, G. Mera, R. Hauser, and A. Klonczynski. Silicon-based polymer-derived ceramics: synthesis properties and applications- a review. *Journal of the Ceramic Society of Japan*, 114:425–444, 2006.

[71] T. Varga, A. Navrotsky, J.L. Moats, R.M. Morcos, F. Poli, K. Müller, A. Saha, and R. Raj. Thermodynamically stable $Si_xO_yC_z$ polymer-like amorphous ceramics. *Journal of the American Ceramic Society*, 90:3213–3219, 2007.

[72] T. Yamaoka, K. Oyoshi, T. Tagami, Y. Arima, K. Yamashita, and S. Tanaka. crystallization of amorphous Si on a glass substrate through nucleation by Si^+ ion implantation. *Applied Physics Letters*, 71:1970–1972, 1990.

[73] V. Heera, R. Kögler, W. Skorupa, and J. Stoemenos. Complete recrystallization of amorphous silicon carbide layers by ion irradiation. *Applied Physics Letters*, 67:1999–2001, 1995.

[74] A. Benyagoub, A. Audren, L. Thomé, and F. Garrido. Athermal crystallization induced by electronic excitations in ion-irradiated silicon carbide. *Applied Physics Letters*, 89:241914, 2006.

[75] M. Nastasi, Q. Su, L. Price, J.A. Colón Santana, T. Chen, R. Balerio, and L. Shao. Superior radiation tolerant materials: amorphous silicon oxycarbide. *Journal of Nuclear Materials*, 461:200–205, 2015.

[76] J.A. Colón Santana, E.E. Mora, L. Price, R. Balerio, L. Shao, and M. Nastasi. Synthesis, thermal stability and the effects of ion irradiation in amorphous SiOC alloys. *Nuclear Instruments and Methods in Physics Research Section B*, 350:6–13, 2015.

[77] Q. Su, L. Price, J. Colon Santana, L. Shao, and M. Nastasi. Irradiation tolerance of amorphous SiOC crystalline Fe composite. *Material Letters*, 155:138–141, 2015.

[78] L.J. Mitchell, F. Naab, O.W. Holland, J.L. Duggan, and F.D. McDaniel. Ion beam synthesis of C-based optically-active nanoclusters in silica. *Journal of Non-Crystalline Solids*, 352:2562–2564, 2006.

[79] P.R. Poudel, B. Rout, D.R. Diercks, Y.M. Strzhemechny, and F.D. Mcdaniel. Fluence dependant formation of β-SiC by ion implantation and thermal annealing. *Applied Physics A*, 104:183–188, 2011.

[80] H. Weishart, V. Heera, F. Eichhorn, B. Pećz, A. Barna, and W. Skorupa. Ion beam synthesis of diamond-SiC heterostructures. *Diamond and Related Materials*, 12:1241–1245, 2003.

[81] V. Heera, F. Fontaine, W. Skorupa, B. Pećz, and Á. Barna. Ion-beam synthesis of epitaxial silicon carbide in nitrogen-implanted diamond. *Applied Physics Letters*, 77:226–228, 2000.

[82] J. C. Pivin and P. Colombo. Ceramic coatings by ion irradiation of polycarbosilanes and polysiloxanes. part I: Conversion mechanism. *Journal of Material Science*, 32:6163–6173, 1997.

[83] Z.G. Wang, Y.F. Jin, E.Q. Xie, Z.Y. Zhu, M.D. Hou, X.X. Chen, Y.M. Sun, and Q.X. Zhang. Swift heavy ion irradiation induced luminescence from C-doped SiO_2 film. *Nuclear Instruments and Methods in Physics Research B*, 193:685–689, 2002.

[84] C.-B. Liu and Z.-G. Wang. Raman scattering investigation of C-doped $a - SiO_2$ after high energy heavy ion irradiations. *Chinese Physics C*, 35:885–889, 2011.

[85] A. Karakucu. *Synthesis and characterization of luminescent nanostructured SiOC thin films*. Ph.D. Dissertation, University of Trento, 2010.

[86] A. Kumar, F. Singh, J.C. Pivin, and D.K. Avasthi. Fabrication of carbon naostructures (nanodots, nanowires) by energetic ion irradiation. , *Journal of Physics D: Applied Physics*, 40:2083–2088, 2007.

[87] T. Prenzel. *Characterization of Silica-Based Hybrid Sol-Gel Coatings after Heat Treatment and Ion Beam Irradiation*. Diploma thesis in Chemistry, University of Bremen, 2009.

[88] J. F. Ziegler. SRIM (Stopping and Range of Ions in Matter). http://www.srim.org.

[89] S. Prawer, K.W. Nugent, Y. Lifshitz, G.D. Lempert, E. Grossman, J. Kulik, I. Avigal, and R. Kalish. Systematic variation of the Raman spectra of DLC films as a function of $sp^2 : sp^3$ composition. *Diamond and Related Materials*, 5:433–438, 1996.

[90] D.G McCulloch, S. Prawer, and A. Hoffman. Structural investigation of xenon-ion-beam-irradiated glassy carbon. *Physical Review B*, 50:5095–5919, 1994.

[91] D.A. Shirley. High-resolution X-ray photoemission spectrum of the valence bands of gold. *Physical Review B*, 5:4709–4714, 1972.

[92] Y. Qi, T. Prenzel, T.A. Harriman, Y.Q. Wang, D.A. Lucca, D. Williams, M. Nastasi, J. Dong, and A. Mehner. Investigation of hydrogen concentration and hardness of ion irradiated organically modified silicate thin films. *Nuclear Instruments and Methods in Physics Research B*, 268:1997–2000, 2010.

[93] T. Venkatesan, T. Wolf, D. Allara, B.J. Wilkens, and G.N. Taylor. Synthesis of novel inorganic films by ion beam irradiation of polymer films. *Applied Physics Letters*, 43:934–936, 1983.

[94] R.V. Gelamo, M.A. Bica de Moraes, B.C. Trasferetti, and F.P. Rouxinol. Modification of plasma-polymerized organosiloxane films by irradiation with He^+, Ne^+, Ar^+, and Kr^+ ions. *Chemistry of Materials*, 17:5789–5797, 2005.

[95] N. Nocuń, E. Leja, J. Jedliński, and J. Najman. Structure and optical properties of hybrid glasses based on tetraethylorthosilicate-trimethoxyoctylsilane and tetraethylorthosilicate-tetraethylorthotitanate-trimethoxyoctylsilane systems. *Journal of Molecular Structure*, 744:597–602, 2005.

[96] T.E. Levine, P. Revesz, E.P. Gianelis, and J.W. Mayer. Ion-beam-induced densification of sol-gel ceramic thin films. *Journal of Vacuum Science and Technology B*, 12:986–990, 1994.

[97] B. Canut, V. Teodorescu, J.A. Roger, M.G. Blanchin, K. Daoudi, and C. Sandu. Radiation-induced densification of sol-gel $SnO_2 : Sb$ films. *Nuclear Instruments and Methods in Physics Research Section B*, 191:783–788, 2002.

[98] L. Abis, L. Armelao, D. Belli Dell'Amico, F. Calderazzo, F. Garbassi, A. Merigo, and E.A. Quadrelli. Gold molecular precursors and gold-silica interactions. *Journal of the Chemical Society-Dalton Transactions*, 18:2704–2709, 2001.

[99] X. Kang, S. Huang, P. Yang, P. Ma, D. Yang, and J. Lin. Preparation of luminescent and mesoporous Eu^{3+}/Tb^{3+} doped calcium silicate microspheres as drug carriers via a template route. *Journal of the Chemical Society-Dalton Transactions*, 40:1873–1879, 2011.

[100] G. Das, G. Mariotto, and A. Quaranta. Vibrational spectroscopy characterization of low-dielectric constant $SiOC : H$ films prepared by PECVD technique. *Materials Science in Semiconductor Processing*, 7:295–300, 2004.

[101] Y.W. Koh, K.P. Loh, L. Rong, A.T.S. Wee, L. Huang, and J. Sudijono. Low dielectric constant $a - SiOC : H$ films as copper diffusion barrier. *Journal of Applied Physics*, 93:1241–1245, 2003.

[102] M. Ibrahim, A. Nada, and D.E. Kamal. Density functional theory and $FT - IR$ spectroscopic study of carboxyl groups. *Indian Journal of pure and applied physics*, 43:911–917, 2005.

[103] V.-M. Graubner, R. Jordan, O. Nuyken, B. Schnyder, T. Lippert, R. Kötz, and A. Wokaun. Photochemical modification of cross-linked poly(dimethylsiloxane) by irradiation at 172 nm. *Macromolecules*, 37:5936–5943, 2004.

[104] A. Grill and D.A. Neumayer. Structure of low dielectric constant to extreme low dielectric constant SiCOH films: Fourier transform infrared spectroscopy characterization. *Journal of Applied Physics*, 94:6697–6707, 2003.

[105] P. Innocenzi. Infrared spectroscopy of sol-gel derived silica-based films: a spectra-microstructure overview. *Journal of Non-Crystalline Solids*, 316:309–319, 2003.

[106] R.M Almeida and C.G. Pantano. Structural investigation of silica gel films by infrared spectroscopy. *Journal of Applied Physics*, 68:4225–4232, 1990.

[107] W.M. Arnoldbik, N. Tomozeiu, E.D. van Hattum, R.W. Lof, A.M. Vredenberg, and F.H.P.M. Habraken. High-energy ion-beam-induced phase separation in SiO_x films. *Physical Review B*, 71:125329, 2005.

[108] H.J. Lee, K.S. Oh, and C.K. Choi. The mechanical properties of the SiOC(−H) composite thin films with a low dielectric constant. *Surface and Coating Technology*, 171:296–301, 2003.

[109] J. Kaspar, C. Terziglu, E. Ionescu, M. Graczyk-Zajac, S. Hapis, H.-J. Kleebe, and R. Riedel. Stable SiOC/Sn nanocomposite anodes for lithium-ion batteries with outstanding cycling stability. *Advanced Functional Materials*, 24:4097–4104, 2014.

[110] Y.-H. Kim, M.S. Hwang, H.J. Kim, J.Y. Kim, and Y. Lee. Infrared spectroscopy study of low-dielectric-constant fluorine-incorporated and carbon-incorporated silicon oxide films. *Journal of Applied Physics*, 90:3367–3370, 2001.

[111] R.L. Mozzi and B.E. Warren. The structure of vitreous silica. *Journal of Applied Crystallography*, 2:164–172, 1969.

[112] G. Lucovsky, J.T. Fitch, D.V. Tsu, and S.S. Kim. Atomic structure in SiO_2 thin films deposited by remote plasma-enhanced chemical vapor deposition. *Journal of Vacuum Science and Technology A*, 7:1136–1144, 1989.

[113] I.W. Boyd and J.I.B. Wilson. Structure of ultrathin silicon dioxide films. *Applied physics Letters*, 50:320–322, 1987.

[114] L. Zheng, Q. An, R. Fu, S. Ni, and S.-N. Luo. Densification of silica glass at ambient pressure. *The Journal of Chemical Physics*, 125:154511, 2006.

[115] Q. An, L. Zheng, and S.N. Luo. Vacancy-induced densification of silica glass. *Journal of Non-Crystalline Solids*, 352:3320–3325, 2006.

[116] L. Douillard and J.P. Duraud. Swift heavy ion amorphization of quartz a comparative study of the particle amorphization mechanism of quartz. *Nuclear Instruments and Methods in Physics Research Section B: Beam Interactions with Materials and Atoms*, 107:212–217, 1996.

[117] L. W. Hobbs and M. R. Pascucci. Radiolysis and defect structure in electron-irradiated α-quartz. *Le Journal de Physique Colloques*, 41:C6–237–C6–242, 1980.

[118] Y.-J. Lee. The second order Raman spectroscopy in carbon crystallinity. *Journal of Nuclear Materials*, 325:174–179, 2004.

[119] Y. liu, W. Ren, L. Zhang, and X. Yao. New method for making porous SiO_2 thin films. *Thin Solid Films*, 353:124–128, 1999.

[120] B. Marchon, J. Gui, K. Grannen, G.C. Rauch, J.W. Ager III, S.R.P. Silva, and J. Robertson. Photoluminescence and Raman spectroscopy in hydrogenated carbon films. *IEEE Transactions on Magnetics*, 33:3148–3150, 1997.

[121] M.J. Matthews, M.A. Pimenta, G. Dresselhaus, M.S. Dresselhaus, and M. Endo. Origin of dispersive effects of the Raman D band in carbon materials. *Physical Review B*, 59:R6585, 1999.

[122] J.D. Herdman, B.C. Connelly, M.D. Smooke, M.B. Long, and J.H. Miller. A comparison of Raman signatures and laser-induced incandescence with direct numerical simulation of soot growth in non-premixed ethylene/air flames. *Carbon*, 49:5298–5311, 2011.

[123] L.G. Cançado, A. Jorio, E.H. Martins Ferreira, F. Stavale, C.A. Achete, R.B. Capaz, M.V.O Moutinho, A. Lombardo, T.S. Kulmala, and A.C. Ferrari. Quantifying defects in graphene via Raman spectroscopy at different excitation energies. *Nano Letters*, 11:3190–3196, 2011.

[124] M.M. Lucchese, F. Stavale, E.H. Martins Ferreira, C. Vilani, M.V.O. Moutinho, R.B. Capaz, C.A. Achete, and A. Jorio. Quantifying ion-induced defects and Raman relaxation length in graphene. *Carbon*, 48:1592–1597, 2010.

[125] H. Baranska, A. Labudzinska, J. Terpinski, and J.R.E. Majer. *Laser Raman Spectrometry: Analytical applications*. Ellis Horwood, West Sussex, UK, 1987.

[126] J. Filik, P.W. May, S.R.J. Pearce, R.K. Wild, and K. R. Hallam. XPS and laser Raman analysis of hydrogenated amorphous carbon films. *Diamond and Related Materials*, 12:974–978, 2003.

[127] C. Casiraghi, A.C. Ferrari, and J. Robertson. Raman spectroscopy of hydrogenated amorphous carbons. *Physical Review B*, 72:085401, 2005.

[128] Y. Xu, D. Su, H. Feng, X. Yan, N. Liu, and Y. Sun. Continuous solgel derived SiOC/HfO_2 fibers with high strength. *RSC Advances*, 5:35026–35032, 2015.

[129] A. Karakuscu, R. Guider, L. Pavesi, and G.D. Sorarãu. White Luminescence from Sol Gel-Derived SiOC Thin Films. *Journal of the American Ceramic Society*, 92:2969–2974, 2009.

[130] G.D. Sorarù, G. D'Andrea, and A. Glisenti. XPS characterization of gel-derived silicon oxycarbide glasses. *Materials Letters*, 27:1–5, 1996.

[131] R.J.P. Corriu, D. Leclercq, P.H. Mutin, and A. Vioux. ^{29}Si NMR and XPS Investigation of the Structure of Silicon Oxycarbide Glasses Derived from Polysiloxane Precursors. *MRS Proceedings*, 346:351–356, 1994.

[132] R.J.P. Corriu, D. Leclercq, P.H. Mutin, and A. Vioux. Preparation and structure of silicon oxycarbide glasses derived from polysiloxane precursors. *Journal of Sol-Gel Science and Technology*, 8:327–330, 1997.

[133] L.-A. O'Hare, A. Hynes, and M.R. Alexander. A methodology for curve-fitting of the XPS Si 2p core level from thin siloxane coatings. *Surface and Interface Analysis*, 39:926–936, 2007.

[134] M. Ouyang, C. Yuan, R.J. Muisener, A. Boulares, and J.T. Koberstein. Conversion of some siloxane polymers to silicon oxide by UV/Ozone photochemical processes. *Chemistry of Materials*, 12:1591–1596, 2000.

[135] P. Mérel, M. Tabbal, M. Chaker, S. Moisa, and J. Margot. Direct evaluation of the sp^3 content in diamond-like-carbon films by XPS. *Applied Surface Science*, 136:105–110, 1998.

[136] Y. Taki and O. Takai. XPS structural characterization of hydrogenated amorphous carbon thin films prepared by shielded arc ion plating. *Thin Solid Films*, 316:45–50, 1998.

[137] F. Verpoort, P. Persoon, L. Fiermans, G. Dedoncker, and L. Verdonck. SiO_2/Si (100)model support with AES and XPS in combination with MLCFA. *Journal of the Chemical Society, Faraday Transactions*, 93:3555–3562, 1997.

[138] K.H. Heinig, T. Müller, B. Schmidt, M. Strobel, and W. Möller. Interfaces under ion irradiation: growth and taming of nanostructures. *Applied Physics A*, 77:17–25, 2003.

[139] R. Reiss and K.H. Heinig. Ostwald ripening during ion beam synthesis a computer simulation for inhomogeneous systems. *Nuclear Instruments and Methods in Physics Research Section B*, 84:229–233, 1994.

[140] T. Meguro, A. Hida, M. Suzuki, Y. Koguchi, H. Takai, Y. Yamamoto, K. Maeda, and Y. Aoyagi. Creation of nanodiamonds by single impacts of highly charged ions upon graphite. *Applied Physics Letters*, 79:3866–3868, 2001.

[141] T. Meguro, A. Hida, Y. Koguchi, S. Miyamoto, Y. Yamamoto, H. Takai, K. Meda, and A. Aoyagi. Nanoscale transformation of sp^2 to sp^3 of graphite by slow highly charged ion irradiation. *Nuclear Instruments and Methods in Physics Research Section B*, 209:170–174, 2003.

[142] Z. Ni, Q. Li, D. Zhu, and J. Gong. Fabrication of carbon nanowire networks by Si ion beam irradiation. *Applied Physics Letters*, 89:053107, 2006.

[143] I. Jenčič, M.W. Bench, I.M. Robertson, and M.A. Kirk. A comparison of the amorphization induced in $Al_xGa_{1-x}As$ and GaAs by heavy ion irradiation. *Journal of Applied Physics*, 69:1287–1293, 1991.

[144] A. Tripathi, A. Kumar, F. Singh, D. Kabiraj, D.K. Avasthi, and J.C. Pivin. Ion irradiation induced surface modification studies of polymers using SPM. *Nuclear Instruments and Methods in Physics Research Section B*, 236:186–194, 2005.

[145] A. Kumar, F. Singh, S.A. Khan, D.C. Agarwal, A. Tripathi, D.K. Avasthi, and J.C. Pivin. Precipitation of semiconducting carbon nanoparticles in ion irradiated gels. *Nuclear Instruments and Methods in Physics Research Section B*, 244:23–26, 2006.

[146] T. Deschamps, J. Margueritat, C. Martinet, A. Mermet, and B. Champagnon. Elastic moduli of permanently densified silica glasses. *Scientific Reports*, 4:7193, 2014.

[147] V.N. Bogdanov, I.M. Brovchenko, L.V. Maksimov, A.R. Silin, and O.V. Yanush. Spectroscopic, optical, and acoustic investigations of radiation modified silica glasses. *Physica Status Solidi A*, 119:621–629, 1990.

[148] S. Kucheyev, Y. Wang, A. Hamza, and M.A. Worsley. Light-ion-irradiation-induced thermal spikes in nanoporous silica. *Journal of Physics D: Applied Physics*, 44:085406, 2011.

[149] S.O. Kucheyev, A.V. Hamza, and M.A. Worsley. Ion-beam-induced stiffening of nanoporous silica. *Journal of Physics D: Applied Physics*, 42:182003, 2009.

[150] A.C. Fischer-Cripps. *Nanoindentation Testing*. Springer, 2011.

[151] N.P. Bansal and R.H. Doremus, editors. *Handbook of Glass Properties*. Academic Press, 1986.

[152] B. Beake and J. Smith. High-temperature nanoindentation testing of fused silica and other materials. *Philosophical Magazine A*, 82:2179–2186, 2002.

[153] D.A. Lucca, K. Herrmann, and M.J. Klopfstein. Nanoindentation: measuring methods and applications. *CIRP Annals - Manufacturing Technology*, 59:803–819, 2010.

[154] Instrumented indentation test for hardness and materials parameters – Part 1: Test method. ISO-14577-1:2002. Geneva, Switzerland ISO.

[155] M.A. El Khakani, M. Chaker, a. Jean, S. Boily, J.C. Kieffer, M.E. O'Hern, M.F. Ravet, and F. Rousseaux. Hardness and Young's modulus of amorphous a-SiC thin films determined by nanoindentation and bulge tests. *Journal of Materials Research*, 9:96–103, 1994.

[156] C. Lee, X. Wei, J.W. Kysar, and J. Hone. Measurement of the elastic properties and intrinsic strength of monolayer graphene. *Science*, 321:385–8, 2008.

[157] D.A. Lucca, R. Ghisleni, J.-K. Lee, Y.Q. Wang, M. Nastasi, J. Dong, and A. Mehner. Effects of ion irradiation on the structural transformation of sol-gel derived TEOS/MTES thin films. *Nuclear Instruments and Methods in Physics Research Section B: Beam Interactions with Materials and Atoms*, 266:2457–2460, 2008.

[158] Y. Qi. *Effects of Ion Irradiation on the Mechanical Properties and Structural Evolution of Sol-Gel Derived Hybrid Silicate Thin Films.* Ph.D. Dissertation, Oklahoma State University, 2015.

[159] C.E. Foerster, F.C Serbena, F.C., I.T.S. Garcia, C.M. Lepienski, L.S. Roman, J.R. Galvõ, and F.C. Zawislak. Mechanical properties of polyhedral oligomeric silsesquioxane (POSS) thin films submitted to Si irradiation. *Nuclear Instruments and Methods in Physics Research Section B: Beam Interactions with Materials and Atoms*, 218:375–380, 2004.

[160] L. Houssiau and N. N. Mine. Molecular depth profiling of polymers with very low energy reactive ions. *Surface and Interface Analysis*, 42:1402–1408, 2010.

[161] V. Zaporojtchenko, J. Zekonyte, and F. Faupel. Effects of ion beam treatment on atomic and macroscopic adhesion of copper to different polymer materials. *Nuclear Instruments and Methods in Physics Research Section B: Beam Interactions with Materials and Atoms*, 265:139–145, 2007.

[162] M. Abdesselam, D. Muller, M. Djebara, S. Ouichaoui, and A.C. Chami. Mev H^+ ion irradiation effect on the stoichiometry of polyethylene terephthalate films. *Nuclear Instruments and Methods in Physics Research Section B: Beam Interactions with Materials and Atoms*, 307:635–641, 2013.

[163] D. Fink, editor. *Fundamentals of Ion-Irradiated Polymers.* Springer, 2004.

[164] T.M. Besmann, editor. *Proceedings of the Thirteenth International Conference on Chemical Vapor Deposition*, chapter Kinetics and Theoretical study of thermal decomposition of tetraethoxysilane in the gas phase. The Electrochemical Society, 1996.

[165] S. Patai and Z. Rappoport, editors. *The Chemistry of Organic Silicon compounds part I*, chapter Thermochemistry. John Wiley and Sons, 1989.

[166] P. Ho and C.F. Melius. Thermochemical data for CVD modeling from Ab initio calculations. *MRS Proceedings*, 335:131–138, 1994.

[167] P. Ho and C.F. Melius. Theoretical Study of the Thermochemistry of Molecules in the Si-O-H-C System. *The Journal of Physical Chemistry*, 99:2166–2176, 1995.

[168] D.R. Lide, editor. *CRC Handbook of Chemistry and Physics, Internet Version.* CRC Presee, 2005.

[169] H. Huber, W. Assmann, S.A. Karamian, A. Mücklich, W. Prusseit, E. Gazis, R. Grötzschel, M. Kokkoris, E. Kossionidis, H.D. Mieskes, and R. Vlastou. Void formation in Ge induced by high energy heavy ion irradiation. *Nuclear Instruments and Methods in Physics Research Section B: Beam Interactions with Materials and Atoms*, 122:542–546, 1997.

[170] S.O. Kucheyev, J.S. Williams, C. Jagadish, J. Zou, V.S. J. Craig, and G. Li. Ion-beam-induced porosity of GaN. *Applied Physics Letters*, 77:1455, 2000.

[171] S.M. Kluth, J.D. Fitz Gerald, and M.C. Ridgway. Ion-irradiation-induced porosity in GaSb. *Applied Physics Letters*, 86:131920, 2005.

[172] T. Konevskikh, A. Ponossov, R. Blümel, R. Lukacs, and A. Kohler. Fringes in FTIR spectroscopy revisited: understanding and modelling fringes in infrared spectroscopy of thin films. *The Analyst*, 140:3969–3980, 2015.

[173] Q. Williams and R. Jeanloz. Spectroscopic evidence for pressure-induced coordination changes in silicate glasses and melts. *Science*, 239:902–905, 1988.

[174] Q. Williams, R.J. Hemley, M.B. Kruger, and R. Jeanloz. High-pressure infrared spectra of α-quartz, coesite, stishovite, and silica glass. *Journal of Geophysical Research*, 98:22157–22170, 1993.

[175] A.M. Hofmeister, J. Xu, and S. Akimoto. Infrared spectroscopy of synthetic and natural stishovite. *American Mineralogist*, 75:951–955, 1990.

[176] T. Sato and N. Funamori. Sixfold-coordinated amorphous polymorph of SiO_2 under high pressure. *Physical Review Letters*, 101:255502, 2008.

[177] R.J. Hemley, H.K. Mao, P.M. Bell, and B.O. Mysen. Raman Spectroscopy of SiO_2 Glass at High Pressure. *Physical Review Letters*, 57:747–750, 1986.

[178] C.J. Benmore, E. Soignard, S.A. Amin, M. Guthrie, S.D. Shastri, P.L. Lee, and J.L. Yarger. Structural and topological changes in silica glass at pressure. *Physical Review B*, 81:054105, 2010.

[179] N. Li, R. Sakidja, S. Aryal, and W.-Y. Ching. Densification of a continuous random network model of amorphous SiO_2 glass. *Physical Chemistry Chemical Physics*, 16:1500–14, 2014.

[180] T. Sato and N. Funamori. High-pressure structural transformation of SiO_2 glass up to 100 GPa. *Physical Review B*, 82:184102, 2010.

[181] G. Buscarino, S. Agnello, F. M. Gelardi, and R. Boscaino. Polyamorphic transformation induced by electron irradiation in a-SiO_2 glass. *Physical Review B*, 80:094202, 2009.

[182] M. Sitarz, C. Czosnek, P. Jele, M. Odziomek, Z. Olejniczak, M. Kozanecki, and J.F. Janik. SiOC glasses produced from silsesquioxanes by the aerosol-assisted vapor synthesis method. *Spectrochimica acta. Part A, Molecular and biomolecular spectroscopy*, 112:440–445, 2013.

[183] B. Champagnon, C. Martinet, M. Boudeulle, D. Vouagner, C. Coussa, T. Deschamps, and L. Grosvalet. High pressure elastic and plastic deformations of silica: In situ diamond anvil cell Raman experiments. *Journal of Non-Crystalline Solids*, 354:569–573, 2008.

[184] G. Compagnini and G. Foti. 1430 cm^{-1} Raman line in ion implanted carbon rich amorphous silicon carbide. *Nuclear Instruments and Methods in Physics Research Section B*, 127-128:639–642, 1997.

[185] C. Demaria, P. Benzi, A. Arrais, E. Bottizzo, P. Antoniotti, R. Rabezzana, and L. Operti. Growth and thermal annealing of amorphous germanium carbide obtained by X-ray chemical vapor deposition. *Journal of Materials Science*, 48:6357–6366, 2013.

[186] G. Compagnini, O. Puglisi, G.A. Baratta, and G. Strazzulla. Vibrational spectroscopy in ion-irradiated carbon-based thin films. *Topics in Applied Physics*, 100:505–520, 2006.

[187] B.-K. Yang, M. Krishnamurthy, and W.H. Weber. Incorporation and stability of carbon during low-temperature epitaxial growth of $Ge_{1-x}C_x (x < 0.1)$ alloys on Si (100): Microstructural and Raman studies. *Journal of Applied Physics*, 82:3287–3296, 1997.

[188] M. Gorman and S.A. Solin. Direct evidence for homonuclear bonds in amorphous SiC. *Solid State Communications*, 15:761–765, 1974.

[189] J.Q. Zhu, C.Z. Jiang, J.C. Han, H.L. Yu, J.Z. Wang, Z.C. Jia, and R.R. Chen. Optical and electrical properties of nonstoichiometric $a - Ge_{1-x}C_x$ films prepared by magnetron co-sputtering. *Applied Surface Science*, 258:3877–3881, 2012.

[190] P. Kazimierski, J. Tyczkowski, M. Kozanecki, Y. Hatanaka, and T. Aoki. Transition from amorphous semiconductor to amorphous insulator in hydrogenated carbon-germanium films investigated by Raman spectroscopy. *Chemistry of Materials*, 14:4694–4701, 2002.

[191] P. Musumeci, F. Roccaforte, and R. Reitano. Angular distortion of Si clusters in $a - SiC$. *Europhysics Letters*, 55:674–678, 2001.

[192] L. Calcagno, G. Compagnini, G. Foti, M.G. Grimaldi, and P. Musumeci. Carbon clustering in $Si_{1-x}C_x$ formed by ion implantation. *Nuclear Instruments and Methods in Physics Research Section B*, 120:121–124, 1996.

[193] C.Z. Wang and K.M. Ho. Structure, dynamics, and electronic properties of diamondlike amorphous carbon. *Physical Review Letters*, 71:1184–1187, 1993.

[194] T.E. Doyle and J.R. Dennison. Vibrational dynamics and structure of graphitic amorphous carbon modeled using an embedded-ring approach. *Physical Review B*, 51:196–200, 1995.

[195] R.N. Tarrant, O. Warschkow, and D.R. McKenzie. Raman spectra of partially oriented sp^2 carbon films: experimental and modelled. *Vibrational Spectroscopy*, 41:232–239, 2006.

[196] J. Finster. SiO_2 in 6:3 (stishovite) and 4:2 Co-ordination Characterization by core level spectroscopy (XPS/XAES). *Surface and Interface Analysis*, 12:309–314, 1988.

[197] D.A. Zatsepin, A.F. Zatsepin, D.W. Boukhvalov, E.Z. Kurmaev, N.V. Gavrilov, N.A. Skorikov, A. von Czarnowski, and H.-J. Fitting. Octahedral conversion of a SiO_2 host matrix by pulsed ion implantation. *Physica Status Solidi (B)*, 1-6, 2015.

[198] J.C. Lascovich, R. Giorgi, and S. Scaglione. Evaluation of the sp^2/sp^3 ratio in amorphous carbon structure by XPS and XAES. *Applied Surface Science*, 47:17–21, 1991.

[199] B. Hornetz, H.J. Michel, and J. Halbritter. ARXPS studies of SiO_2-SiC interfaces and oxidation of 6H SiC single crystal Si-(001) and C-(001) surfaces. *Journal of Materials Research*, 9:3088–3094, 1994.

[200] H.f. Li, S. Dimitrijev, D. Sweatman, H.B. Harrison, P. Tanner, and B. Feil. Investigation of nitric oxide and Ar annealed SiO_2/SiC interfaces by x-ray photoelectron spectroscopy. *Journal of Applied Physics*, 86:4316–4320, 1999.

[201] C. Onneby. Silicon oxycarbide formation on SiC surfaces and the SiC/SiO_2 interface. *Journal of Vacuum Science and Technology A: Vacuum, Surfaces, and Films*, 16:1597–1602, 1998.

[202] N. Stojilovic. Why Can't We See Hydrogen in X-ray Photoelectron Spectroscopy? *Journal of Chemical Education*, 89:1331–1332, 2012.

[203] D. Briggs and M.P. Seah. *Practical Surface Analysis. Volume 1. Auger and X-ray Photoelectron Spectroscopy*. John Wiley and Sons, 1990.

[204] J.C. Pivin and M. Sendova-Vassileva. Visible photoluminescence of ion irradiated polysiloxane films. *Solid State Communications*, 106:133–138, 1998.

[205] D. Chen, Z.M. Liao, L. Wang, H.Z. Wang, F Zhao, W.Y. Cheung, and S.P Wong. Photoluminescence from $\beta -$ sic nanocrystals embedded in SiO_2 films prepared by ion implantation. *Optical Materials*, 23:65–69, 2003.

[206] S. Walter, G.D. Soraru, H. Bréquel, and S. Enzo. Microstructural and mechanical characterization of sol gel-derived SiOC glasses. *Journal of the European Ceramic Society*, 22:2389–2400, 2002.

[207] G. Hasegawa, editor. *Studies on Porous Monolithic Materials Prepared via Sol-Gel Processes*, chapter Fabrication of Macroporous SiC and SiC/C Monoliths from Arylene-Bridged Polysilsesquioxanes via Carbothermal Reduction. Springer Japan, 2013.

[208] G. Das, G. Mariotto, and A. Quaranta. Microstructural evolution of thermally treated low-dielectric constant SiOC : H films prepared by PECVD. *Journal of the Electrochemical Society*, 153:F46–F51, 2006.

[209] P. Innocenzi, M.O. Abdirashid, and M. Guglielmi. Structure and properties of sol-gel coatings from methyltriethoxysilane and tetraethoxysilane. *Journal of Sol-Gel Science and Technology*, 3:47–55, 1994.

[210] R. Riedel and I.-W. Chen, editors. *Ceramics Science and Technology: Volume 1: Structures*, chapter Modelling Amorphous Ceramic Structures. Wiley-VCH, 2008.

[211] G.M. Bancroft, H.W. Nesbitt, R. Ho, D.M. Shaw, J.S. Tse, and M.C. Biesinger. Toward a comprehensive understanding of solid-state core-level XPS linewidths: Experimental and theoretical studies on the Si 2p and O 1s linewidths in silicates. *Physical Review B*, 80:075405, 2009.

[212] M.D. Ulrich, J.G. Hong, J.E. Rowe, G. Lucovsky, A.S.-Y. Chan, and T.E. Madey. Soft X-ray photoelectron spectroscopy of $(HfO_2)_x(SiO_2)_{1-x}$ high-k gate-dielectric structures. *Journal of Vacuum Science and Technology B: Microelectronics and Nanometer Structures*, 21:1777–1782, 2003.

[213] D.K. Sarkar, S. Bera, S. Dhara, K.G.M Nair, S.V. Narasimhan, and S. Chowdhury. XPS studies on silicide formation in ion beam irradiated Au/Si system. *Applied Surface Science*, 120:159–164, 1997.

[214] A.M. Ektessabi and S. Hakamata. XPS study of ion beam modified polyimide films. *Thin Solid Films*, 377-378:621–625, 2000.

[215] M. Antonello, G.W. Arnold, G. Battaglin, R. Bertoncello, E. Cattaruzza, P. Colombo, G. Mattei, P. Mazzoldi, and F. Trivillin. Fluence and current density dependence of silver nanocluster dimensions in ion-implanted fused silica. *Journal of Materials Chemistry*, 8:457–461, 1998.

[216] N. Suyal, D. Hoebbel, M. Mennig, and H. Schmidt. A solid state ^{29}Si and ^{13}C NMR study on the synthesis of thin silicon-oxycarbide glass sheets by a sol-gel route. *Journal of Materials Chemistry*, 9:3061–3067, 1999.

Appendix A

Curve fitting results of C 1s spectra of ion irradiated films

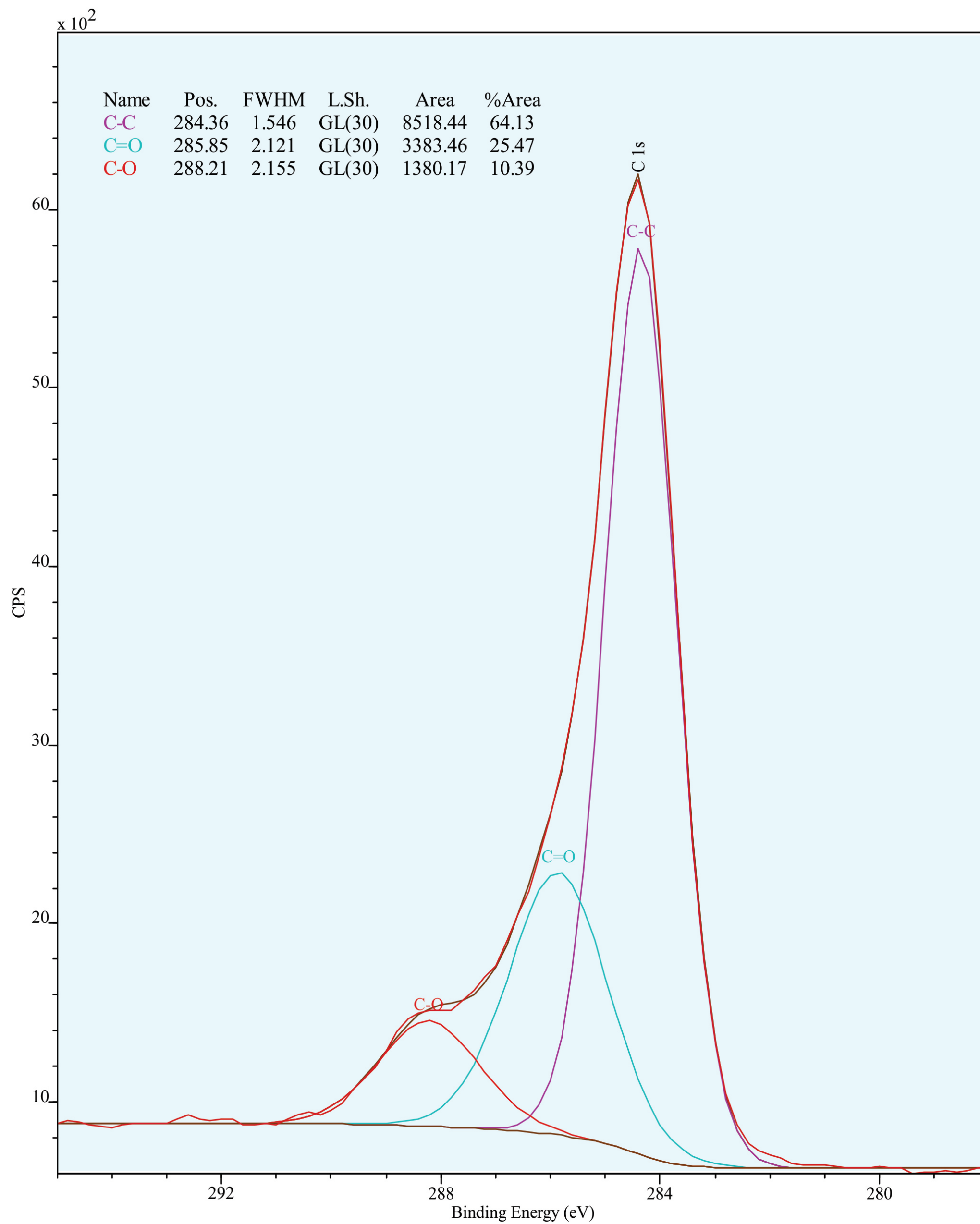

Figure A.1: Curve fitting results of C 1s spectra of N^{2+} irradiated film with a fluence of 5×10^{15} ions/cm^2. The C-C, C=O, and C-O peaks are indicated in the figure.

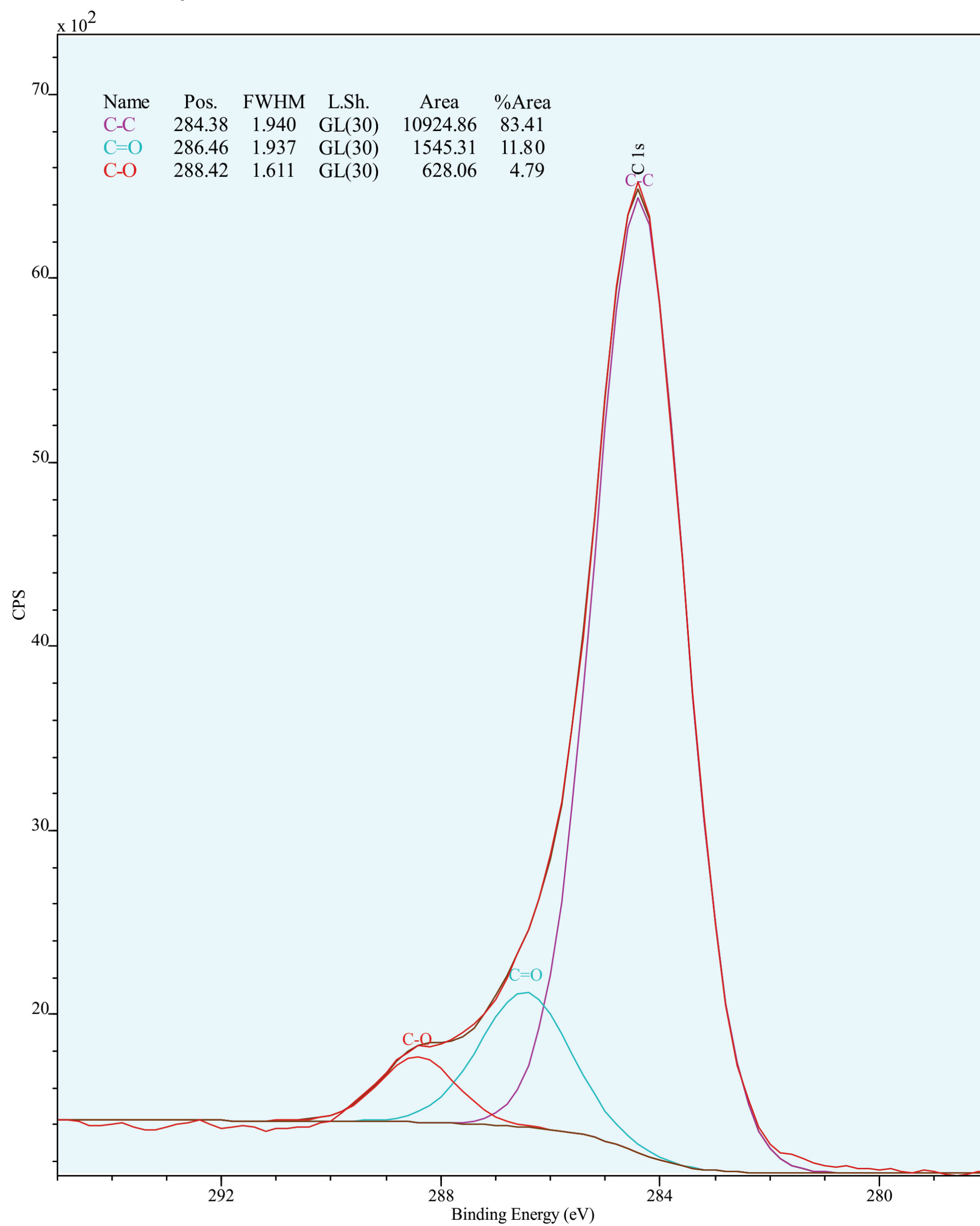

Figure A.2: Curve fitting results of C 1s spectra of Cu^{3+} irradiated film with a fluence of 10^{16} ions/cm^2. The C-C, C=O, and C-O peaks are indicated in the figure.

Appendix B

XPS O 1s spectra of ion irradiated and heat-treated films

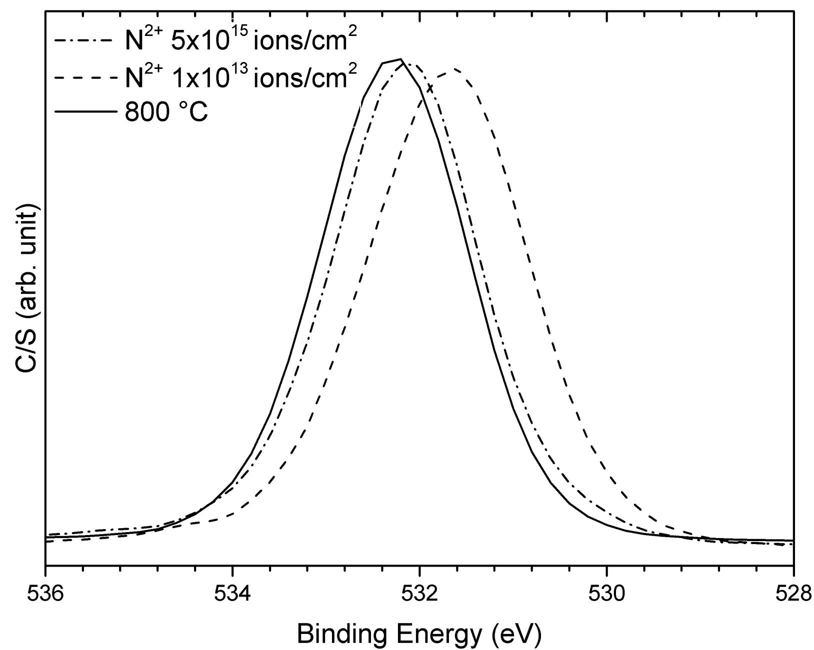

Figure B.1: XPS O 1s spectra of the films irradiated with light ions.

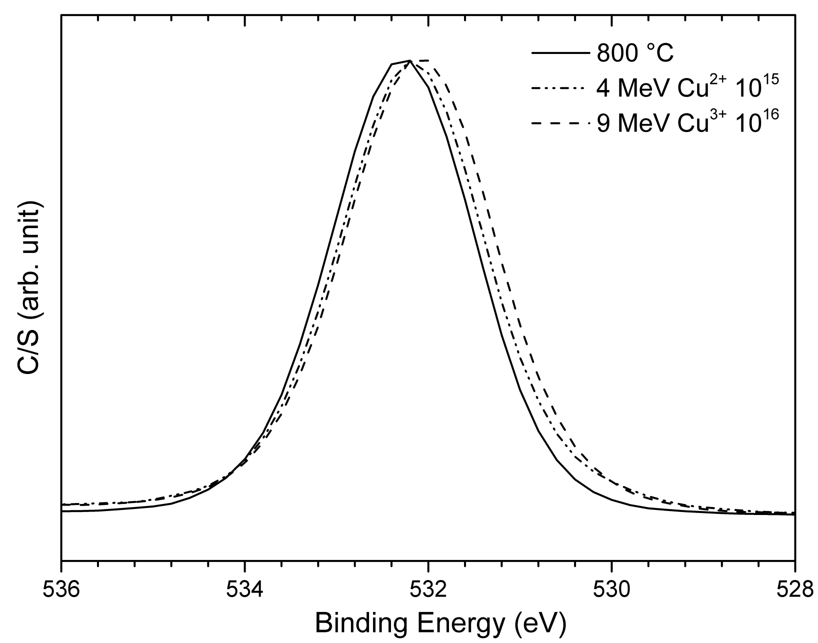

Figure B.2: XPS O 1s spectra of the films irradiated with heavy ions.

Appendix C

Silica Raman modes of fused silica and the film heat-treated at 800 °C

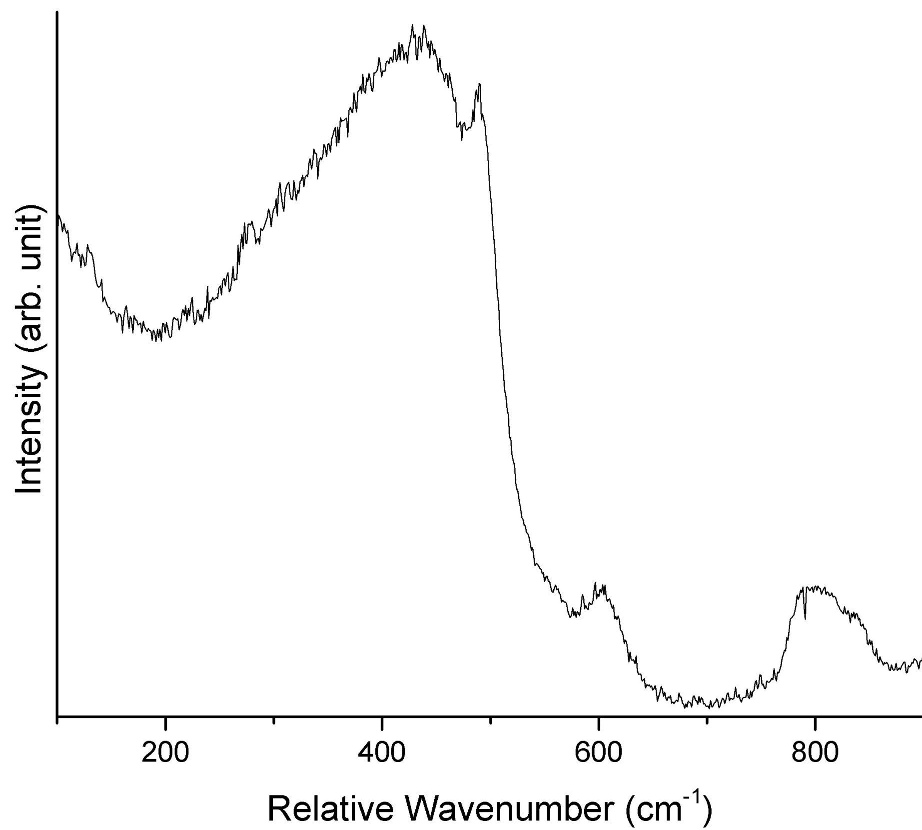

Figure C.1: Raman spectra of fused silica.

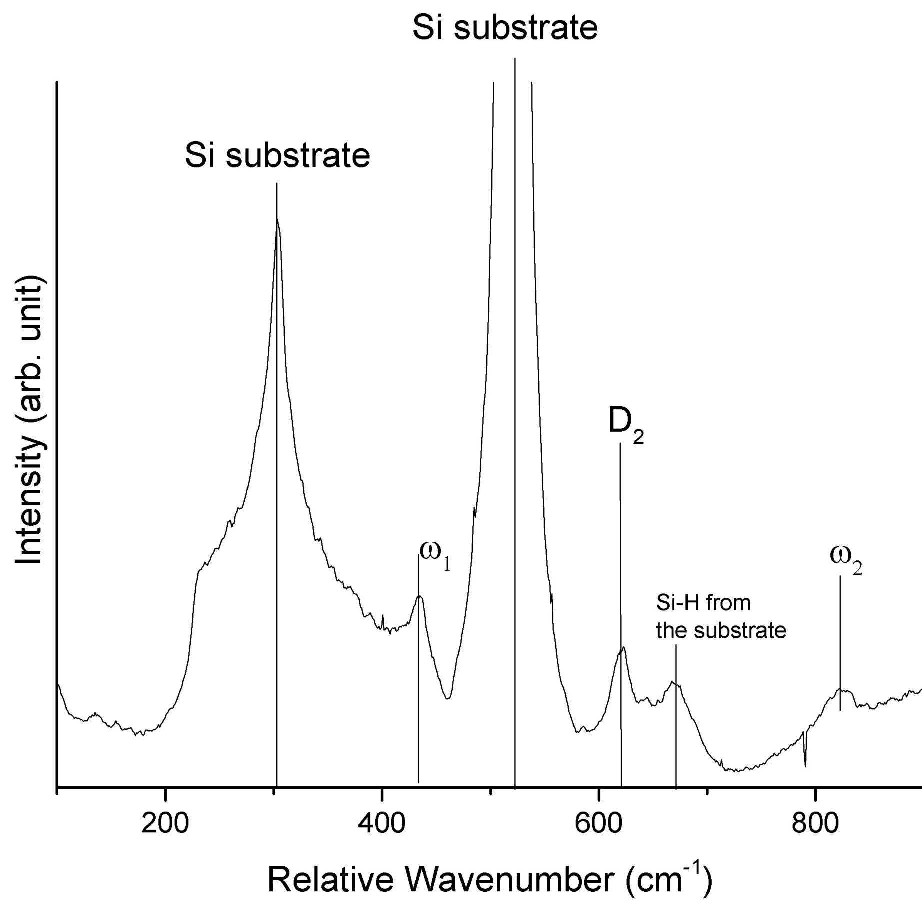

Figure C.2: Raman spectra of the heat-treated acid-catalyzed film after heat-treatment at 800 °C.

Appendix D

Estimation of free carbon content of ion irradiated and heat-treated films

In the following an attempt is made to quantitatively measure the concentration of different SiO_xC_y tetrahderas. As mentioned in Section 4.2.4, based on the energy difference between the XPS position of silica and silicon carbide, the binding energies of various SiO_xC_y tetrahedra (SiO_4, SiO_3C, SiO_2C_2, $SiOC_3$, as well as SiC) has been determined previously [129, 130, 132] as 103.5, 102.7, 101.9, 101.1 and 100.3 eV, respectively; and so, a quantitative evaluation of these tetrahedra can be achieved using XPS. The position of all lines were fixed in curve fitting. In addition, the FWHM of all lines were linked to be similar to each other. Initially the FWHM of 1.16 was chosen, based on the reported FWHM values in the literature for peak width of XPS Si 2p line of SiO_2 thin films [211,212]. However, it did not result in satisfactory fitting results. The FWHM of silica XPS line increases after ion irradiation [213–215], so the FWHM was chosen separately for each film using the two following constraints: 1) All lines should have similar FWHM and 2) The value of FWHM should be lower than 2 (the largest reported FWHM in the literature for line-width of ion irradiated Si 2p line). The results of curve fitting are presented in Table D.1.

In addition, the concentration of different tetrahedra can also be utilized to estimate the ratio of free carbon (i.e., carbon bonded to other carbon atoms) to bonded carbon (i.e., carbon bonded to silicon atoms). The method described in the coming paragraph, first suggested by Suyal et. al., [216], was utilized to estimate the concentration of free carbon within the films.

Suyal et. al., [216] utilized NMR spectroscopy to measure the concentration of different tetrahedra and then used the data to estimate the ratio of carbon bonded to silicon . They estimated the C/Si ratio using the following equation:

$$\begin{aligned} C/Si\,(at\%) = \;& (SiO_4\ area) \times 0 + (SiO_3C\ area) \times 0.25 + (SiO_2C_2\ area) \times 0.5 \\ & + (SiOC_3\ area) \times 0.75 + (SiC_4\ area) \times 1 \end{aligned} \tag{D.1}$$

where

$$(SiO_4\ area) + (SiO_3C\ area) + (SiO_2C_2\ area) + (SiOC_3\ area) + (SiC_4\ area) = 100 \tag{D.2}$$

This is based upon the fact that each carbon atom is bonded to four silicon atom and so each carbon in a tetrahedra is shared with four other silicon atoms. Suyal et. al., further extended their methodology to estimate the stoichiometric composition of the amorphous silica phases (i.e., the composition of silica phase without considering the free carbon phase). The authors assumed that no Si-Si or C-O bonds exist in the structure and so, the composition of glass can be stated as $SiC_{X/2}O_{2-X}$ and the O/Si ratio can be calculated from:

$$O/Si\,(at\%) = 2 - 2(C/Si\,(at\%)) \tag{D.3}$$

This analysis was performed on the NMR spectroscopy results of the SiOC films. However, the same logic can be extended to XPS spectroscopy, because the same tetrahedra are being studied when either XPS or NMR is used.

As indicated in Table D.1, there was an increase in carbon incorporation in the silica network after ion irradiation and carbon incorporation increased with increasing the ion energy.

Considering that the C/Si ratio for both the silica network and the overall film is known, an estimate of free carbon can be achieved using the following equation:

$$C_{free}(at\%) = \frac{C_{total} - C_{bonded}}{C_{total}} \times 100 \tag{D.4}$$

C_{total} can be estimated from ERD/RBS results (except for the heat-treated film, for which the total carbon was estimated from the XPS-derived chemical composition) and C_{bonded} can be estimated from the XPS Si 2p spectra, as described above. The free carbon estimates are presented in the table D.1. There was a an increase in the concentration of free carbon after ion irradiation and concentration of free carbon increased with increasing the ion energy. It should be noted that concentration of tetrahedra, stoichiometric composition and free carbon content results are only rough approximates, as the utilized methodology assumes that the concentration of broken bonds and vacancies are negligible. However, high concentration of broken bonds and vacancies after ion

irradiation is expected. The calculations were also not performed on the 9 MeV Cu^{3+} irradiated films, because a portion of the silica phase in these films are octahedrally bonded.

Table D.1: The concentration of different SiO_xC_y tetrahedra along with C/Si ratio and percentage of free carbon in each specimen.

Conversion condition	SiO_4 (%)	SiO_3C (%)	SiO_2C_2 (%)	$SiOC_3$ (%)	SiC_4 (%)	Stoichiometric composition	C_{free} (%)
800°C	43	56	0	1	0	$SiC_{0.15}O_{1.69}$	4
400 keV N^{2+} 5×10^{15} ions/cm^2	23	68	8	1	0	$SiC_{0.21}O_{1.58}$	92
4 MeV Cu^{2+} 10^{15} ions/cm^2	16	64	16	4	0	$SiC_{0.27}O_{1.46}$	77

Appendix E

Low Temperature Photoluminescence Spectra

The observed peaks are noises due to the long integration time.

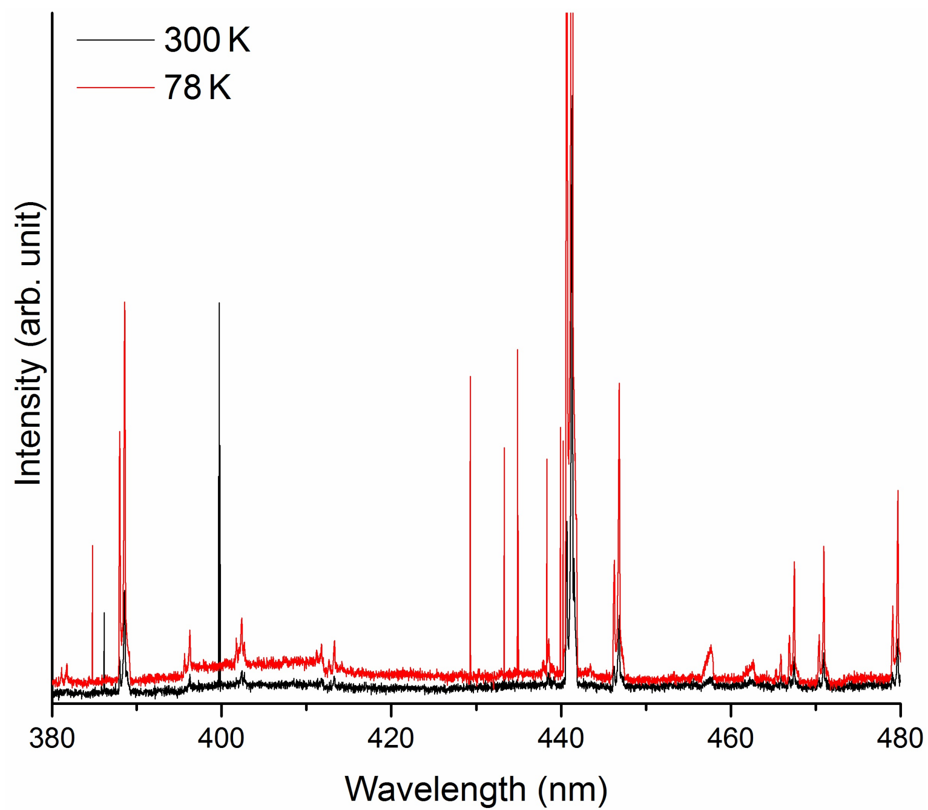

Figure E.1: Room temperature and low temperature photoluminescence spectra of the 1 MeV Cu^{+} irradiated film with a fluence of 10^{16} ions/cm^{2} in the 380-480 nm range.

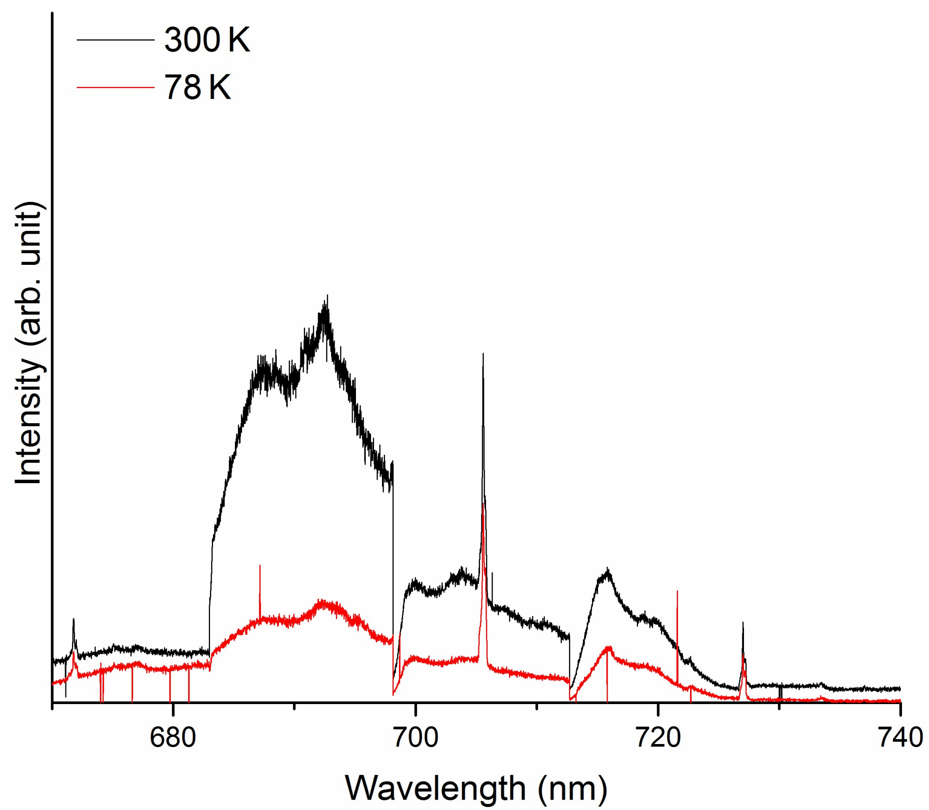

Figure E.2: Room temperature and low temperature photoluminescence spectra of the 1 MeV Cu^{+} irradiated film with a fluence of 10^{16} ions/cm^2 in the 660-740 nm range.

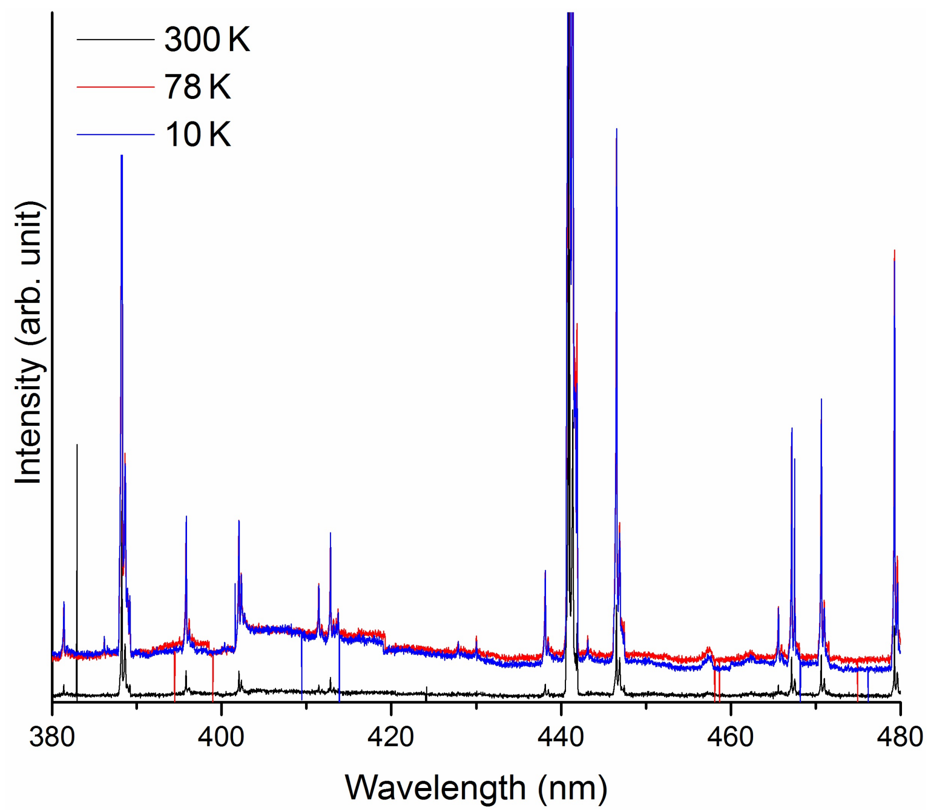

Figure E.3: Room temperature and low temperature photoluminescence spectra of the 9 MeV Cu^{3+} irradiated film with a fluence of 10^{16} ions/cm^2 in the 380-480 nm range.

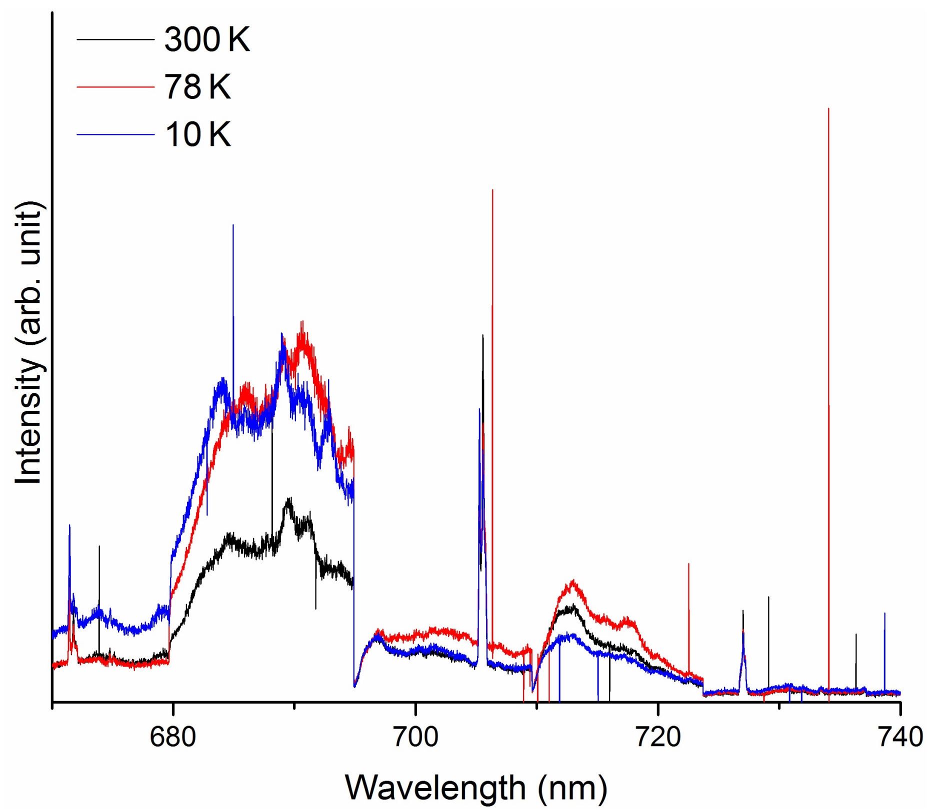

Figure E.4: Room temperature and low temperature photoluminescence spectra of the 9 MeV Cu^{3+} irradiated film with a fluence of 10^{16} ions/cm^2 in the 660-740 nm range.

VITA

Seyyed Ali Shojaee

Candidate for the Degree of

Doctor of Philosophy

Thesis: EFFECTS OF ION IRRADIATION ON THE CHEMICAL AND MICROSTRUCTURAL PROPERTIES OF SOL-GEL DERIVED THIN FILMS

Major Field: Mechanical and Aerospace Engineering

Biographical:

Personal Data: Born in Mashhad, Iran on Spetember 17, 1983 to Mahvash Shabazaz and Hossein Shojaee.

Education:
Graduated from Malek Ashtar High School, Mashhad, Iran in 2000. Received the Bachelor of Science degree in Materials Engineering from Ferdowsi University of Mashhad in 2006 and Master of Science in Materials Science and Engineering from Sharif University of Technology in 2008. Completed the requirements for the Doctor of Philosophy in Mechanical Engineering at Oklahoma State University, Stillwater, Oklahoma in August, 2016.

Experience:
Internship, Khorasan Razavi Regional Electric Company, 2004; Researcher, Kavosh Sanat Toos, 2004-2006; Research Assistant, Sharif University of Technology, 2008; Graduate Research/Teaching Assistant, Oklahoma State University, 2009-present.

Professional Memberships:
American Chemical Society